Toward nanoscale reactivity mapping under electro-catalytic reaction conditions

Plasmon-enhanced vibrational spectroscopy of the electrochemical gold oxidation and gold oxide reduction

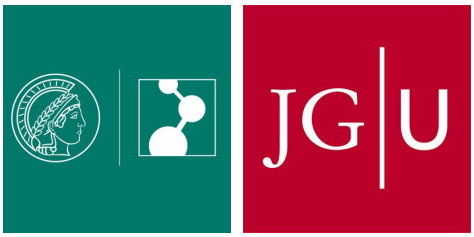

Jonas H. K. Pfisterer

Max Planck Institute for Polymer Research

Dissertation zur Erlangung des Grades eines
'Doctor rerum naturalium (Dr. rer. nat.)'
der Fachbereiche:
08 - Physik, Mathematik und Informatik
09 - Chemie, Pharmazie und Geowissenschaften
10 - Biologie
Universitätsmedizin
der Johannes Gutenberg-Universität

Max Planck Graduate Center

Mainz, August 2019

1. Gutachterin: [redacted]

2. Gutachter: [redacted]

3. Prüfungsvorsitz: [redacted]

4. Prüfungskomitee: [redacted]

5. Prüfungskomitee: [redacted]

Tag der mündlichen Prüfung: 15. Oktober 2019

Declaration

I hereby declare that I wrote the dissertation submitted without any unauthorized external assistance and used only sources acknowledged in the work. All textual passages which are appropriated verbatim or para-phrased from published and unpublished texts as well as all information obtained from oral sources are duly indicated and listed in accordance with bibliographical rules. In carrying out this research, I complied with the rules of standard scientific practice as formulated in the statutes of Johannes Gutenberg-University Mainz to insure standard scientific practice.

Jonas H. K. Pfisterer

Abstract

Detailed molecular understanding of surface chemistry under realistic non-equilibrium working conditions is pivotal for the rational design of efficient electrocatalytic energy conversion devices or effective measures against surface corrosion. Operando monitoring of reacting species with high surface-molecular sensitivity and chemical specificity under reaction conditions, ideally with nanometer spatial resolution, can provide the necessary molecular insights to understand the underlying surface electrochemistry. However, detection of reaction intermediates is challenging; in particular assessing simultaneously nano-structure surface topography and local chemical information on the nanoscale.

In this thesis, we investigate one of the most important model electrodes in fundamental electrochemistry: polycrystalline and single crystal Au surfaces in sulfuric acid electrolytes. We show how new molecular and unprecedented nanoscale insight into the electrochemical Au oxidation and Au oxide (AuOx) reduction can be obtained using electrochemical surface-enhanced Raman and infrared (EC-SERS/EC-SEIRAS) as well as tip-enhanced Raman spectroscopy (EC-TERS).

We use potential-jumps to the AuOx electro-reduction onset combined with EC-SERS to monitor the evolution of short-lived reaction intermediates. Our results confirm that Au-OH intermediates are formed also in acidic media and give spectral evidence of Au atoms in a 4-fold coordination with oxygen resembling the bulk Au_2O_3 coordination. The EC-SER spectra further attest the adsorption of (bi)sulfate ions during surface reduction. For sulfate adsorption on Au(111), we show how the potential-dependent vibrational Stark effect and coverage-dependent contributions to the observed EC-SEIRA signal can be disentangled. Using EC-SEIRAS potential-jump experiments combined with a model equation that can describe the potential-induced peak shift of the sulfate stretch vibrational mode, we quantify the coverage-dependent contribution to be 15.6 ± 1.2 cm$^{-1}/\theta_{SO}$ and the Stark effect to be 75.6 ± 2.7 cm^{-1}/V.

Importantly, we demonstrate how near-field optical nanoscopy, EC-TERS, offers a unique approach for corrosion and electrocatalysis to map nanoscale defect reactivity under electrocatalytic reaction conditions with a chemical spatial sensitivity of $\sim$10 nm. We find that the electro-oxidation reactivity of Au nanodefects is directly correlated to their surface topography and is limited to an oxide depth of $\sim$3 nm. The local Raman fingerprint indicates the presence of at least two spatially separated AuOx species, namely Au_2O_3 and Au_2O, on the nanodefects. Finally, we discuss the implications of all presented results for future EC-TERS studies to identify potential-dependent reaction pathways and their active sites at the sub-10 nm level, which will aid to push our understanding of defect reactivity to the molecular or atomistic level.

Zusammenfassung

Ein detailiertes molekulares Verständnis der Oberflächenchemie unter realistischen Operationsbedingungen ist ausschlaggebend für das rationale Design effizienter elektrokatalytischer Energiekonvertierungsgeräte oder effektiver Maßnahmen gegen Oberflächenkorrosion. Die Beobachtung reaktiver Spezies mit hoher oberflächen-molekularer Sensitivität und chemischer Spezifizität unter Reaktionsbedingungen, idealerweise mit räumlicher Auflösung im Nanometerbereich, kann die notwendigen molekularen Einblicke liefern, um die zugrundeliegende Oberflächenelektrochemie zu verstehen. Jedoch ist die Detektion von Reaktionszwischenprodukten herausfordernd, besonders das gleichzeitige Untersuchen der nanostrukturierten Oberflächentopographie und lokaler chemischer Informationen auf der Nanoskala.

In der vorliegenden Doktorarbeit wird eine der wichtigsten Modellelektroden im Bereich der grundlegenden Elektrochemie untersucht: poly- und einkristalline Goldoberflächen in Schwefelsäure. Es wird gezeigt, wie neue molekulare und nanoskalige Einblicke in die elektrochemische Goldoxidation und Goldoxidreduktion mittels elektrochemischer oberflächenverstärkter Raman- und Infrarot- (EC-SERS/EC-SEIRAS), als auch spitzenverstärkter Raman-Spektroskopie (EC-TERS) erhalten werden können.

Potentialsprünge zum Einsetzen der Goldoxidreduktion werden mit EC-SERS kombiniert, um die Entwicklung kurzlebiger Reaktionszwischenprodukte zu verfolgen. Die Ergebnisse bestätigen, dass Au-OH Zwischenprodukte auch in saurer Umgebung entstehen und geben spektrale Hinweise auf Au Atome in einer 4-fach Koordination mit Sauerstoff, welche der Au_2O_3 Bulk-Koordination ähnelt. Die EC-SER Spektren belegen die Adsorption von (Bi)Sulfationen während der Oberflächenreduktion. Für die Sulfatadsorption auf Au(111) wird aufgezeigt, wie der potentialabhängige Stark-Effekt und bedeckungsabhängige Beiträge des beobachteten EC-SEIRA Signals unterschieden werden können. Mittels EC-SEIRAS Potentialsprungexperimenten in Kombination mit einer Modellgleichung, welche die potential-induzierte Peakverschiebung der Sulfatstreckschwingung beschreibt, werden die bedeckungsabhängigen Beiträge auf 15.6 ± 1.2 cm$^{-1}/\theta_{SO}$ und der Stark-Effekt auf 75.6 ± 2.7 cm^{-1}/V quantifiziert.

Zudem wird aufgezeigt, wie optische Nahfeld-Nanoskopie, EC-TERS, einen einzigartigen Ansatz auf dem Gebiet der Korrosion und Elektrokatalyse bietet, um Defektreaktivität unter elektrokatalytischer Reaktionsbedingungen mit einer chemisch-räumlichen Sensitivität von ca. 10 nm aufzulösen. Die Elektrooxidationsreaktivität von Au Nanodefekten korreliert direkt mit ihrer Oberflächentopographie und ist begrenzt auf eine Oxiddicke von etwa 3 nm. Der lokale Raman-Fingerabdruck zeigt das Auftreten von mindestens zwei räumlich getrennten Oxidspezies auf den Nanodefekten an und zwar Au_2O_3 and Au_2O.

Abschließend werden die Implikationen der vorgestellten Ergebnisse für zukünftige EC-TERS Studien zur Identifikation potentialabhängiger Reaktionspfade und ihrer aktiven Zentren im sub-10 nm Bereich diskutiert, welche unser Verständnis reaktiver Defekte auf molekularer bzw. atomarer Ebene vorantreiben wird.

Contents

1 Introduction **1**

1.1 Identifying active sites and local defect chemistry . . . 3

1.1.1 Catalytic studies with TERS in air . . . 5

1.1.2 Moving into liquid . . . 6

1.1.3 Electrifying TERS in liquid . . . 7

1.2 Gold(oxide) - a model system . . . 9

1.3 Thesis outline . . . 10

2 Fundamentals and techniques **13**

2.1 Electrochemistry . . . 13

2.1.1 Electrochemical double layer . . . 14

2.1.2 Nernst equation (Thermodynamics) . . . 15

2.1.3 Butler-Volmer equation (Kinetics) . . . 16

2.1.4 Cyclic voltammetry . . . 18

2.2 Electrocatalysis . . . 21

2.3 Gold electro-oxidation and gold oxide reduction . . . 23

2.3.1 Gold - a noble metal . . . 23

2.3.2 Metal oxidation/reduction mechanisms . . . 25

2.4 Scanning tunneling microscopy . . . 28

2.4.1 Tunneling effect . . . 28

2.4.2 STM method . . . 29

2.4.3 Electrochemical STM . . . 31

2.5 Plasmon-enhanced vibrational spectroscopies . . . 32

2.5.1 Raman scattering . . . 34

2.5.2 Surface-enhanced Raman spectroscopy . . . 38

2.5.3 Tip-enhanced Raman spectroscopy . . . 41

2.5.4 Surface-enhanced IR absorption spectroscopy . . . 48

3 Monitoring the AuOx electro-reduction **53**
3.1 Introduction . . . 54
3.2 Materials and experimental details . . . 56
3.3 Experimental results . . . 57
3.4 EC-SERS potential-jump approach . . . 65
3.5 Identification of reaction intermediates . . . 67
3.5.1 Au-OH intermediates . . . 67
3.5.2 Gold oxide intermediates . . . 69
3.5.3 Role of (bi)sulfate anions . . . 71
3.6 Gold oxide electro-reduction mechanism . . . 72
3.7 Conclusions and Outlook . . . 73
3.8 Data processing and analysis . . . 75

4 Sulfate adsorption on Au(111) **77**
4.1 Stark effect or coverage dependence? . . . 78
4.2 Materials and experimental details . . . 79
4.3 Continuous scan experiments . . . 80
4.4 EC-SEIRAS potential-jump experiments . . . 83
4.5 Modeling of the ν_{SO} peak shift . . . 87
4.6 Conclusions and Outlook . . . 90
4.7 Data evaluation and error propagation . . . 91

5 Nanoscale EC-TERS mapping of defect reactivity **95**
5.1 Introduction . . . 96
5.2 Materials and experimental details . . . 98
5.3 EC-TERS detects reaction products . . . 98
5.4 Nanoscale mapping of Au defect oxidation . . . 102
5.5 Revealing defect chemistry on the 10 nm scale . . . 108
5.6 Conclusions and Outlook . . . 109
5.7 EC-TERS data analysis . . . 111

6 Conclusions and Outlook **117**
6.1 Conclusions . . . 117
6.2 A bright EC-TERS future for electrocatalysis . . . 118

Bibliography **123**

Acknowledgements **147**

Chapter 1

Introduction

The continuously growing world population and the rise of living-standards worldwide has been leading to a continuous increase in energy consumption, usage of fossil fuels, toxic chemicals and other resources over the past decades. The limited availability of the world's resources, further projected growth of energy demands, and environmental aspects, such as climate change, urge the global transition to a sustainable 'green' economy [Chu12]. Part of a solution concept, known as the 'hydrogen economy', is based on the idea of using carbon-free molecular hydrogen produced from renewable energy sources as energy carrier and was suggested by John Bockris and John Appleby in 1972 [Boc13]. Within this concept, intermittant renewable energies can be stored in the chemical bonds of molecular hydrogen (that is produced by water splitting, i.e. $2\ H_2O \rightarrow 2\ H_2 + O_2$) and later, at a desired point in time, be transformed back from chemical energy into electricity by fuel cell devices.

The field of electrochemistry plays a critical role for this electrochemical energy conversion scheme, as it is the electrochemical electrolyzers (the devices that transform electrical into chemical energy by water splitting) and fuel cell devices that form the centerpiece of this electrochemical energy conversion scheme. In both electrolyzer and fuel cell, electrocatalytic materials (electrocatalysts) speed up the electrochemical reaction by offering an alternative reaction pathway to thus decrease the reaction activation energy barrier and increase device efficiency. Current research seeks to develop electrocatalysts that are highly active but cheap, selective towards a desired reaction and at the same time stable for many hours of operation under the harsh environments of aqueous solutions or vapors [Deb12, You18]. The development of such energy materials is a challenging task [She17], because most often it is far from straightforward to experimentally identify which defect sites, such as nanoscale protrusions or step edges, are most active and which defects are

bound to degradation and corrosion phenomena.

The knowledge of site-specific reaction pathways and nanostructure-activity relations can be used to establish rational design principles to accordingly modify the electrode's nanoscale surface structure and/or material composition to enhance activity, selectivity and/or stability of the electrode toward a given electrochemical reaction [Mis16]. To elaborate such rational design principles for efficient energy conversion devices, novel electrochemical synthesis protocols or effective measures against material corrosion, elucidation of reaction mechanisms by operando monitoring and identification of surface reaction intermediates are required [Ban14, Mei18, Don19], ideally on the atomic level. However, detection and reliable identification of reaction intermediates with nanoscale spatial precision during electrochemical reactions are challenging: the inherently limited number of available surface sites [Van69] require high sensitivity to detect and characterize few reactive molecules at the catalyst surface. Low residence times of the reaction intermediates at the surface [Hou14, Ben16] warrant additional high surface-molecular sensitivity to allow sufficiently low acquisition times in the order of µs to s. Highly surface-molecular sensitive experimental tools are required that provide chemical specificity under realistic working conditions with nanoscale spatial chemical and topographic resolution.

Operando surface-enhanced Raman and infrared (IR) spectroscopy (EC-SERS/EC-SEIRAS) provide the surface molecular-sensitivity and chemical specificity under reaction conditions [Wu08, Sam05]. In particular, IR and Raman vibrational spectroscopies offer molecular chemical fingerprints sensitive to the nature and the chemical environment of the molecules under investigation. The high surface molecular sensitivity is achieved by metal surface nanostructures that amplify the IR and Raman signals. However, EC-SERS/SEIRAS provide an average response of the catalyst surface and molecular species in few nanometer proximity to the amplifying nanostructures present within the focus spot. Ideally, one could perform EC-SERS/SEIRAS measurements with nanometer spatial resolution at a single location. Electrochemical tip-enhanced Raman spectroscopy (EC-TERS) offers nanoscale chemical resolution of electrified solid-liquid interfaces by utilizing a single plasmonic hotspot that can be strategically moved across the sample surface to probe different surface locations. While the TERS technique under ambient conditions was introduced almost 20 years ago, the in-situ electrochemical TERS analog was only recently pioneered independently by the Ren [Zen15], Van Duyne [Kur15] and Domke groups [Mar17b]. These first works have demonstrated astonishing capabilities to address the molecular behavior of few molecules in situ. However, for the field of elec-

trocatalysis, corrosion or other solid-liquid interface-related disciplines, one key ability has yet to be demonstrated: the operando nanoscale chemical reactivity mapping and direct correlation between local chemistry and surface topography under electrochemical reaction conditions.

The overarching goal of this thesis is to answer the question how EC-TERS chemical imaging of the local defect chemistry and the identification of active nanoscale defects under reaction conditions is achievable. For this purpose, we map the electro-oxidation of nanoscale defects at Au(111) single crystal surfaces in contact with sulfuric acid and correlate surface topography and chemical reactivity. In the process, we further show how quasi-atomistic insight can be gained by complementary EC-SERS/EC-SEIRAS potential-jump experiments to identify (hydr)oxide intermediates or to study sulfate adsorption paving the way for the current but also future EC-TERS studies. In this way, electrochemical plasmon-enhanced vibrational spectroscopy will ultimately contribute to the necessary nanoscale mechanistic understanding to aid the rational design of highly efficient and stable electrocatalysts in the future.

The content of this thesis is partly adapted/reproduced from published [Pfi18, Pfi19c] or about to be published work [Pfi19a, Pfi19b]. This chapter is (partly) reproduced/adapted from 'Jonas H. K. Pfisterer and Katrin F. Domke, "Unfolding the versatile potential of EC-TERS for electrocatalysis", Current Opinion in Electrochemistry, 2018, 8, 96-102', published by Elsevier in 2018 [Pfi18].

1.1 Identifying active sites and local defect chemistry

Two of the key challenges in electrocatalysis as well as in corrosion science are (i) to determine the atomic composition of catalytically active surface sites that possess optimal adsorption properties and (ii) to identify molecular species and reaction pathways at specific surface sites as a function of applied (over)potential [O'M14, Bel03, Jar07]. The inhomogeneous reactivity distribution at catalytically active electrodes was already pointed out in 1925 by Hugh Stott Taylor [Tay25]. According to Taylor, it is not the complete catalyst surface that is catalytically active, but only specific surface sites. Ensemble studies indicate that these 'active sites' are often defects with adjusted coordination numbers, e.g. step edges or protrusions, that are responsible for most of the overall surface activity [Mis16]. For example, the oxygen reduction reaction (ORR) in alkaline media shows higher efficiency on the Au(100) single crystal surface than on Au(111) due to ad-

justed adsorption properties of the reaction intermediates [Her07]. In analogy, corrosion phenomena typically initiate at particular surface nanodefects and progress stepwise into the material [Luo18]. Step edge defects on Au(111) surfaces are, for example, electro-oxidized to gold oxide (AuOx) at about 10 to 20 mV lower overpotentials compared to the (111) terrace sites [Kol00, Zhu13]. These results indicate that, in general, different atomic arrangements favour different mechanistic pathways. To rationally engineer nanoparticles with specific atomic arrangements or defects enhancing surface reactivity and/or stability, detailed molecular understanding at the nanoscale or even atomic level is therefore required. The correlation between nanoscale surface atomic arrangements such as step edges or adatoms and reactivity or the site-specific reaction pathways, however, are still not fully understood – due to the lack of operando methodologies with chemical nanoscale resolving capabilities.

Model experiments under ultra high vacuum (UHV) conditions and computer simulations have remarkably contributed to our current understanding of the relation between defect reactivity and surface structure [Tho14]. However, atomistic insights from UHV studies or computer simulations are often difficult to translate to more complex reaction environments. Scanning electrochemical microscopy (SECM [Ben19]) has been used, for example, to study the electrochemical response of molybdenum disulfide nanosheet edges with <20 nm spatial resolution [Sun19] or to resolve the reactivity of single Au nanoparticles of 10 nm size [Sun14]. Electrochemical scanning tunneling microscopy (EC-STM) has recently been utilized to identify active surface sites by the comparison of local current fluctuations of the tunneling barrier above reactive and non-reactive nanoscale surface sites [Pfi17]. However, as for SECM, EC-STM in general lacks chemical specificity that would be required to obtain local chemical information about the reacting species.

The challenge of acquiring nanoscale chemical information of reacting molecules can be overcome by employing EC-TERS, as is demonstrated in this thesis. EC-TERS smartly comprises EC-scanning probe microscopy (EC-SPM) and label-free near-field Raman spectroscopy - introducing chemical specificity to EC-SPM setups. The SPM-tip is utilized as a nano-antenna that amplifies the otherwise weak Raman signals of few molecular adsorbates, where the Raman enhancement originates from surface plasmons that create a strong localized near-field at the SPM-tip apex providing intense TER scattering. The SPM-tip, or EC-TERS probe, can be strategically positioned on the electrode surface to locally investigate and compare the desired reaction/adsorption sites. The comprised SPM setup allows simultaneous imaging of the surface topography. TERS under UHV

conditions has demonstrated stunning chemical spatial resolution of down to the sub-nm level [Zha13a, Lee19]. Under ambient conditions, chemical spatial resolution of few nanometers has been achieved [Zho17, Su18]. Although EC-TERS has only recently been introduced to the electrochemists' tool box, the pioneering and very recent EC-TERS works hold great promise for future implementation of the EC-TERS approach in electrocatalytic research. In the following, we shortly review the current status of TERS in air to study catalytic reactions and the to date available liquid- and EC-TERS literature and their implications for electrocatalysis.

1.1.1 Catalytic studies with TERS in air

It has been repeatedly demonstrated that TERS in air offers direct experimental insight into nanoscale surface chemistry relevant for catalytic research questions, such as molecular orientation [Zha10, Toc16], chemical interactions [Dom09, Jia15] or charge-transfer properties [Liu11, Kra17], achieving even picosecond time resolution in specialized setups [Kli14]. The first TERS studies of a catalytic chemical conversion process, the dimerization reaction of 4-nitrothiophenol (NTP) to form dimercaptoazobenzene (DMAB), were published in 2012. Van Schrojenstein Lantman et al. followed the photo-catalyzed dimerization reaction with TERS under ambient conditions [van12]. Xu and co-workers quantified the chemical conversion as a function of laser intensity with UHV-TERS [Sun12, Zha13b]. Another remarkable study underlining the potential of TERS to monitor catalytic conversion was published by Chaunchaiyakul et al. who recently observed the formation of C≡C triple bonds due to dehydrogenation of (M)-2,13-bis(hydroxymethyl)(7)thiaheterohelicene on Au(111) [Cha17].

Making use of the nanoscale mapping ability of TERS, in 2015, Kumar et al. monitored the photocatalytic induced dimerization of p-mercaptoaniline (pMA) on Ag nanoparticles under ambient conditions and resolved the catalytically active nanoparticles with around 20 nm chemical spatial resolution [Kum15]. Correlated TERS maps and topography images revealed that the reaction occurred only on the Ag nanoparticles. Employing phenyl isocyanide as probe molecules, Zhong et al. investigated the site-specific catalytic properties of a bimetallic Pd-submonolayer on Au(111) model catalyst with a TERS resolution of 3 nm [Zho17]. The combined TERS and theory work allowed quantification of the molecule–surface site interaction energies at the Pd-Au step edge compared to the monometallic terrace sites due to the distinct electronic properties of the step edge. In a similar more recent work, the same group reported a chemical spatial resolution of even 2.5 nm [Su18].

While these examples highlight the molecular insights and chemical spatial resolution that is currently achievable with TERS in air measurements, TERS setup implementation in liquid electrolytes poses additional technical challenges to the TERS optics due to light aberrations at the air-glass-liquid interface [Gjo12].

1.1.2 Moving into liquid

Solid-liquid TERS was first demonstrated by Schmid et al. [Sch09]. Since then, only a handful of studies have been conducted in liquids without potential control [Nak13, Mar16, Tou16, Pie16, Mar17a, Kum18, Bha19b, Kum19, Bha19a]. The growing number of recent TERS studies have concentrated on bottom excitation-collection atomic force microscopy (AFM)-TERS, in which the transparent substrate is immersed to a small drop of liquid. For example, Kumar et al. imaged single-wall carbon nanotubes on a glass substrate under a drop of water and achieved a chemical spatial resolution of about 28 nm using Cr-Au-Ag tips [Kum18]. However, direct correlation between simultaneously recorded SPM and liquid-TERS maps was yet missing. In another study, Kumar et al. developed a new zirconia-protected TERS probe with increased lifetime, with which the authors studied the plasmon-assisted oxidation or dimerization reaction of p-aminothiophenol (pATP) on a Ag nano-structured substrate immersed in a water droplet [Kum19]. The heterogeneous Ag substrate revealed structure-dependent variations in reactivity revealing an average apparent size of the reaction hotspots of about 14 nm. This liquid-TERS study can be considered the extension of the earlier presented TERS work in air by Kumar et al. in 2015 [Kum15]. Similarly, Bhattarai and El-Khoury recently studied also a plasmon-assisted dimerization reaction of a self-assembled NTP monolayer on Au microplates on a glass support in the liquid phase [Bha19a]. The authors moved a Au-coated AFM-TERS-tip in water across the Au-glass boundary region composed as a ∼30 nm high Au edge and mapped the DMAB dimer product and the characteristic NTP resonance, respectively. The authors visualized the inhomogeneous distribution of reactant and product across the Au platelet edge region and attributed these inhomogeneities to steric or molecular crowding effects. Based on theory calculations and their recorded TER spectra, the authors further observed both cis- as well as trans-DMAB product molecules formed at the surface. In a prior study, the same group had shown that it is the edges of thiol-functionalized Au triangular platelets that reveal highest TERS intensities for the nitrile stretch at 2222 cm^{-1} and inferred enhanced local fields at the ∼40 nm high Au edges, obtaining a chemical spatial resolution of around 15 nm [Bha19b].

While these liquid-drop TERS approaches give valuable insight into solid-liquid interfaces, EC-TERS poses additional experimental challenges, such as potential control of the substrate, the necessity of well-engineered sample cells that accommodate bulk liquid electrolytes and high cleanliness of all electrochemical cell components. The advantage of a bulk electrolyte lies in the increased available space to accommodate counter and reference electrodes, the reduced risk of rapid solvent evaporation and possible concomitant pH changes. Moreover, the potential-control allows insertion of the electrolyte into the sample cell under well-defined conditions, if that is required, and can prevent detachment of molecules from the surface. Most importantly, triggering of electrochemical processes and the simultaneously obtainable current-potential response characterizing the macroscopic electrode state are promising assets.

1.1.3 Electrifying TERS in liquid

In 2015, Ren and co-workers studied 4-PBT ((4-(pyridin-4-yl)biphenyl-4-yl)methanethiol) on Au(111) with EC-TERS and observed molecule configurational changes as a function of applied potential due to protonation and deprotonation of the adsorbed molecules [Zen15]. By means of density functional theory (DFT) calculations and comparison of EC-SERS and EC-TERS spectra acquired in different pH electrolytes, the authors found the nitrogen end of the 4-PBT to be protonated at negative potentials or deprotonated at positive potentials. Interestingly, the cyclic voltammogram (CV) was almost featureless within the exploited potential limits as the 4-PBT monolayer passivated the Au(111), leaving only the EC-TERS signal for analysis of the local protonation/deprotonation. Very recently, the Ren group successfully implemented a water immersion objective to the EC-TERS setup that led to a remarkable 5-fold sensitivity increase and allowed the authors to study the electrochemical redox processes of anthraquinone molecules on Au(111) [Hua19].

In 2015, Van Duyne and co-workers investigated the redox reaction of Nile Blue (NB) dye molecules on polycrystalline indium tin oxide (ITO) [Kur15]. They correlated the EC-TER scattering intensity with the charges of the faradaic current in the simultaneously acquired CV. Surprisingly, a potential difference for the onset of NB oxidation/reduction to more negative potential values by >100 mV was observed for the nanoscale TERS response compared to the macroscale CV response. This difference between nano- and macro-scale observables was ascribed to the local disturbance of the electrochemical double layer by the TERS-tip in nanometer proximity to the electrode.

In a follow-up study, Van Duyne and co-workers extracted the apparent formal potential

($E_0^{'}$) from TERS-intensity vs. potential curves (TERS-CVs) for different surface coverages, giving evidence of single-molecule electrochemistry [Mat16]. The extracted $E_0^{'}$ varied as a function of electrode surface location and the occurrence of two-step TERS-CVs at low surface coverages supported a preferential adsorption at specific surface sites. The authors statistically analyzed the extracted cathodic and anodic $E_0^{'}$. Plotting the occurrence of specific $E_0^{'}$ values returned an ensemble TERS-CV comparable to a conventional CV. The authors found the anodic $E_0^{'}$ distribution to be narrower than the cathodic $E_0^{'}$, which indicates that reduced NB is less sensitive to the local electrochemical environment. Recently, the Van Duyne group studied the same NB redox system as well as cobalt phtalocyanine (CoPc) also on opaque Au(111) electrodes further correlating EC-TERS with macroscopic CV features and studying the potential-triggered order/disorder phase transition for the CoPc case [Che18b, Jia19]. For the CoPc/Au(111) system, the authors did not observe any EC-TERS features related to the ORR, for example the CoPc-O_2 complex.

The Domke group recorded the potential-dependent vibrational fingerprint of less than 100 small, non-resonant adenine molecules self-assembled on Au(111) [Mar17b]. Combining EC-TERS, CV and density functional theory (DFT) calculations, the authors proposed a potential-dependent reversible adsorption/reaction model for the adenine/Au(111) system: below 0.3 V vs. Ag/AgCl, adenine weakly physisorbs in a tilted geometry in its neutral state. When ramping to higher potentials, adenine adapts an upright adsorption geometry around the potential of zero charge. Above 0.6 V vs. Ag/AgCl, adenine is deprotonated and adsorbs flat at the Au(111) surface, interacting strongly via Au–N bonds. Such metal–$\mathcal{X}$ (with $\mathcal{X}$ typically N, O, S) vibrational modes at low wavenumbers <400 cm^{-1} can be easily observed with EC-TERS. They are of particular interest in electrochemical surface science as they give direct insight into adsorbate–electrode interactions, important for the chemical characterization of, for example, oxidized (electro)catalyst surfaces. Furthermore, site-specific understanding of molecular orientation is of pivotal importance as reactant geometry likely induces local changes in the electric double layer and determines macroscopic device performance [Kim00].

Yokota et al. suggested self-assembled monolayers (SAMs) of benzenethiol (PhS) on Au(111) as a standard sample for EC-TERS measurements in 0.1 M $HClO_4$ and studied the oxidative removel of the SAMs upon surface oxidation [Yok19]. Interestingly, according to presented EC-STM images before and after Au surface oxidation, protrusions that are formed during the PhS assembly on Au(111) disappear - in contrast to the typically observed surface-roughening after Au(111) oxidation [Sch97]. Further chemical

insight on the nanoscale is required to understand such corrosion prohibiting effects or surface restructuring and demands combined EC-STM and EC-TERS nanoscale mapping.

Very recently, the Van Duyne group achieved the in-situ mapping of spatially heterogeneous surface potential distribution on ITO grains with 40 nm resolution [Kan19]. Employing EC-AFM-TERS, the authors mapped the extracted $E_0^{'}$ from TERS-CVs of NB molecules adsorbed to electrodes composed of well-defined Au(111) nanoplates on polycrystalline ITO substrates. Correlating AFM-topography with $E_0^{'}$ maps across the boundary region of Au(111) and ITO visualized surface-location-dependent variations of the formal potential. While the $E_0^{'}$ distribution on Au(111) followed a single Gaussian distribution, on ITO, a bimodal Gaussian behavior was observed, attributed to the polycrystallinity of the ITO surface, revealing an overall $E_0^{'}$ difference of about 4 mV between Au and ITO. In addition, comparison between an AFM-friction image and the $E_0^{'}$ map revealed certain ITO grains with more negative $E_0^{'}$, which the authors proposed to be related to a more negative surface charge. One of the prime goals has thus been achieved - simultaneous EC-TERS and EC-STM imaging of molecules adsorbed on electrode surfaces under electrochemical conditions to directly correlate nanoscale electrochemical parameters, such as the apparent formal potential, and topography in situ.

For the application of EC-TERS in electrocatalysis, the crucial next step is to show that potential-dependent adsorption/desorption processes on pristine electrocatalyst surfaces without a pre-assembled monolayer can be followed under reaction conditions.

1.2 Gold(oxide) - a model system

Au was the first reported electrode material used for water splitting [Tro89]. As electrocatalytic material, Au has remained attractive to tune catalytic electrode properties [Rod14, Kod16] or as an important model system to study, for example, the reactivity of nanoparticles [Her07, Sun14]. In general, Au electrodes can be considered as one of the most important model electrodes in fundamental electrochemistry, for example to study ion adsorption [Ata98], metal island deposition [Fes18], electrocatalytic reactions [Rod14], biosensors [Bar13] or SAMs [Mar17b].

During the initial steps of anodic water splitting, pristine Au is transformed into AuOx (see Section 2.3 for reaction equation) that decisively changes the electrode's catalytic properties and provides a source of the element of oxygen for O_2 evolution [Con95]. For

example, based on online electrochemical mass spectrometry and oxygen isotope exchange experiments, Koper and co-workers showed that at low overpotentials the evolved molecular oxygen originates purely from the oxide surface, while at higher potentials, the evolved oxygen is a combination from the oxide lattice and oxygen atoms from the water [DM13]. The AuOx electro-reduction mimics the processes occuring during the oxygen evolution reaction (OER) at anodic potentials or during the oxidation of small organic molecules both in the absence of the actual oxidation reaction. The AuOx formed during Au surface electro-oxidation at anodic potentials still below the OER and the formation of a surface-limited oxide thin film are already the product of water splitting. From macroscopic cyclic voltammetry (CV) experiments on Au single crystal electrodes, Zhumaev et al. revealed that it is the surface defects that electro-oxidize first, i.e. at lower potentials, compared to well-defined atomically smooth terrace sites that oxidize only at higher potentials [Zhu13]. Such defect oxidation can be considered as a model corrosion phenomenon as well as the initial active sites for water splitting.

Despite the significance of Au(Ox) as a versatile model system for electrocatalysis and metal corrosion, the exact nature of the oxidized Au - the starting point for further water splitting or AuOx reduction - is not resolved. Weaver and co-workers hypothesized that a broad vibrational feature around 580 cm^{-1} originates from more than a single AuOx species [Des86] and various (hydr)oxide species, such as $Au(OH)_3$, hydrated or anhydrous Au_2O_3, OAuOH or Au_2O have been suggested in the literature [Peu84, Shi07]. Possibly, the chemical oxide composition of active nanodefect sites locally varies, making it challenging to disentangle from macroscopic ensemble measurements, and thus determines the local electro-oxidation reactivity. However, assessing the local oxide chemistry on the nanoscale level has to date not been possible. Moreover, it is typically assumed that Au-OH intermediates are formed as reaction intermediates during Au oxidation/AuOx reduction in acidic environment [AK86]. However, the spectroscopic detection and reliable identification of OH-intermediates during the AuOx reduction in acidic media has, to the best of our knowledge, not been confirmed experimentally.

1.3 Thesis outline

This thesis aims at providing the proof-of-principle that near-field optical nanoscopy, EC-TERS, offers a unique approach for corrosion and electrocatalysis research to study active (defect) site chemistry at the nanoscale under electrocatalytic reaction conditions. We pave the way for the present EC-TERS study by providing complementary EC-SERS and

EC-SEIRAS investigations elucidating the oxide reduction and sulfate adsorption at Au surfaces.

Chapter 2 introduces some of the important concepts in electrochemistry relevant for understanding CV, the basic idea of defects in electrocatalysis and the oxidation/reduction of Au(Ox). Further, the STM methodology is presented before explaining Raman scattering and the, for this study, crucial spectroscopic methods: EC-SERS, EC-TERS and EC-SEIRAS.

Chapter 3 further sets the scene for our nanoscale chemical imaging experiments by providing evidence that EC-SERS on simple electrochemically roughened polycrystalline Au surfaces offers sufficient SERS enhancement to detect various reaction products/intermediates under reaction conditions. We perform EC-SERS potential-jump experiments to monitor and identify short-lived reaction intermediates during the electro-reduction of AuOx in sulfuric acid. We jump to the AuOx reduction onset potential to monitor the dynamically evolving reaction intermediates as a function of time over several tens of seconds. We observe a peak splitting of the broad AuOx spectral feature around 594 cm^{-1} into two bands, which we identify as Au-OH and Au in a 4-fold coordination with oxygen resembling the bulk Au_2O_3 coordination. Further, the EC-SER spectra provide evidence for the adsorption of (bi)sulfate ions during the surface reduction process. The presented potential-jump experiments linked with advanced DFT simulations performed by our collaborator confirm the formation of Au-OH intermediates in acidic media during surface reduction.

Chapter 4 highlights the role of sulfate ions that can adsorb onto Au(111) electrodes and discusses how the potential-dependent vibrational Stark effect and coverage-dependent contributions to the observed EC-SEIRA signal can be disentangled. Using EC-SEIRAS potential-jump experiments combined with a simple linear model equation that can describe the potential-induced peak shift of the sulfate stretch vibrational mode, we quantify the coverage dependence contribution to be 15.6 ± 1.2 cm^{-1}/θ_{SO} and the Stark effect to amount to 75.6 ± 2.7 cm^{-1}/V. Potential-jump EC-SEIRAS experiments offer a new route to better understand and interpret adsorbate interactions at electrified solid-liquid interfaces.

In Chapter 5, we provide the proof-of-concept that EC-TERS is capable to assess topographic and chemical information simultaneously on the nanoscale level under electro-

chemical reaction conditions. We have mapped the electro-oxidation of nanoscale defects at Au(111) single crystal surfaces in aqueous sulfuric acid and correlate heterogeneous surface topography and electrochemical reactivity under reaction conditions with a chemical spatial sensitivity of about 10 nm. Correlation of the EC-TERS AuOx signal intensity and EC-STM height profiles allows us to estimate the local defect oxide layer thickness to be 3 nm. The observation of AuOx peak shifts as a function of EC-TERS probe position indicates the spatial distribution of at least two different AuOx species, namely Au_2O_3 and Au_2O, locally present on the defective nano-structures. Delivering such nano-chemistry and nano-defect reactivity information during surface oxidation demonstrates the unprecedented insights that are now within reach to identify potential-dependent reaction pathways and their active sites at the sub-10 nm level.

Chapter 6 concludes by summarizing the overall findings of this thesis, followed by a short description of current research efforts and pointing out possible future research directions.

Chapter 2

Fundamentals and techniques

Electrochemical plasmon-enhanced vibrational spectroscopies are interdisciplinary experimental methods by their very nature that require detailed understanding of electrochemistry, near-field optics, surface science and solid-state chemistry or physics. EC-TERS is the combination of three experimental techniques. SPM, electrochemistry and Raman spectroscopy are joint together to create a versatile and powerful experimental methodolgy, capable to address the local electrochemistry on the nanoscale. In this chapter, the basic theoretical concepts, necessary to familiarize the reader with the employed experimental techniques and their working principles are discussed. In addition, the experimental setups utilized within this thesis are specified. First, some of the basic considerations in the field of electrochemistry and the most standard electrochemical method, CV, are discussed to provide a broad basis to understand the origins of potential-dependent current flow through a sample electrode. Afterwards, some of the basic ideas of electrocatalysis, such as the Sabatier principle and the concept of active (defect) sites, are presented. Furthermore, the chemical and electrocatalytic properties of Au are discussed, together with the current understanding of the general Au oxidation/reduction mechanisms. Moreover, the technique of STM is discussed. IR and Raman spectroscopy, plasmonic field-enhancement and the enhanced vibrational spectroscopies, EC-SERS, EC-TERS and EC-SEIRAS, employed in this work are elaborated.

2.1 Electrochemistry

The field of electrochemistry is the branch of chemistry that deals with the relation between measurable electric currents, i.e. flowing electric charges, and chemical changes. An external voltage applied between two electron conducting electrodes connected through an ionic conductor (electrolyte) can induce chemical changes at the electrode, e.g. redox

reactions spatially separated at the two electrodes or molecular adsorption processes, and trigger charge transfer across the electrochemical inferface. Vice versa, externally driven chemical changes, e.g. by supplying an excess of chemical species to the electrodes, can result in measurable current flow. Precise control of the applied electrode potential (i.e. controlling the electrode's Fermi level) allows the fine tuning of the chemical processes occuring at the solid-liquid interface, for example, to trigger or stop a desired chemical reaction. The concomitant flowing electric charges can be measured and provide insight into the underlying electrochemical processes. Different electrochemical processes, such as ion adsorption or electrocatalytic reactivity, often depend on the surface nanostructure and the electrolyte environment and it can be challenging to ascribe the measured macroscopic electric currents unambiguously to specific electrochemical processes or molecular configurations. Plasmon-enhanced vibrational spectro-electrochemistry can provide the necessary molecular specificity complementing the electrochemistry approach. Electrochemical plasmon-enhanced vibrational spectroscopy presents a powerful experimental methodology to study surface electrocatalytic reactivity, as shown throughout this thesis (Chapter 3, 4, 5). In the following, some of the most important fundamental concepts of electrochemistry (based on Bard and Faulkner [Bar01]) are discussed that help to grasp the essence of electrochemical techniques, such as CV, the basic electrochemical characterization technique to study the electrode-electrolyte interface.

2.1.1 Electrochemical double layer

When an electrode, for example a piece of metal, is immersed into an electrolyte solution, an electrochemical double layer (EDL) is formed at the solid-liquid interface. The ions and solvent molecules of the electrolyte arrange close to the solid metal electrode to establish an electrostatic equilibrium between the charges in the electrode and the ions and polarized species in the electrolyte. Figure 2.1 shows schematically such an EDL structure with the specifically and non-specifically adsorbed as well as solvated ions. The double layer structure refers to the metal electrode (first layer, Figure 2.1 gray color) and the solution side (second layer, Figure 2.1 blue color). The electrolyte configuration is additionally structured in a compact layer close to the electrode-electrolyte interface (Figure 2.1 up to z_c) and a diffuse layer of solvated ions (Figure 2.1 from z_c). The EDL is of great importance, since adsorbed ions can have a profound influence on electrochemical processes at the solid-liquid interface [Col16]. For instance, chemisorbed solvent ions can block surface sites and hinder the adsorption of reactants or reaction intermediates [Che07]. In Chapter 3, we discuss how adsorbed (bi)sulfate ions play an important role during the reduction of AuOx. It is noteworthy that the schematic of Figure 2.1 illustrates

the ideal case of an atomically flat metal electrode. The presence of surface defects locally changes the distribution/configuration of the EDL as well as the local surface electric fields.

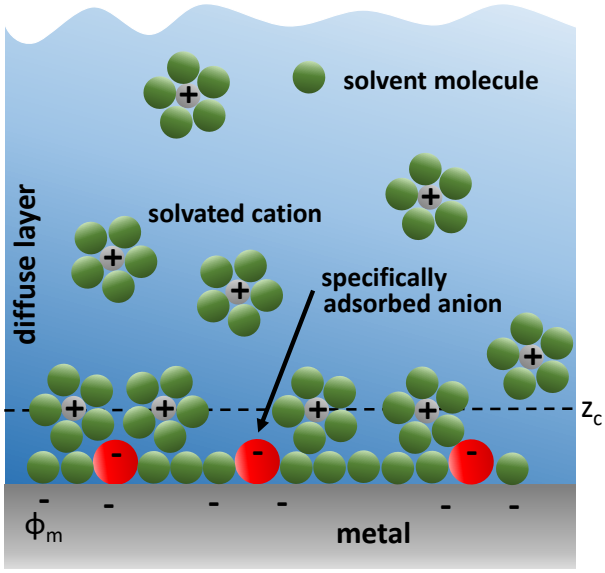

Figure 2.1. *Schematic of the EDL. ϕ_m is the surface electric field at the metal electrode surface that is directly related to the applied electrode potential. The distance from the electrode surface to z_c defines the compact layer. Image adapted from Ref. [Bar01].*

2.1.2 Nernst equation (Thermodynamics)

The electrochemical equilibrium that is established upon immersion of a metal electrode into an electrolyte and the thereby established open circuit potential (OCP) is quantitatively described by thermodynamics. The electrochemical potential, $\tilde{\mu}$, can be written as:

$$\tilde{\mu} = \mu_0 + RT \cdot \ln(a) + nF\varphi\,. \tag{2.1}$$

Here, μ_0 represents the standard chemical potential, R is the gas constant, T is the temperature, a is the activity, n specifies the number of moles and F and φ are the Faraday constant and the electrostatic potential, respectively. The electrochemical potential is composed of the chemical potential term, $\mu = \mu_0 + RT \cdot \ln(a)$, that originates from the chemical interactions between molecular species, and an electrostatic potential term, $nF\varphi$, which stems from the additional electrostatic interactions between the (charged) species. At electrochemical equilibrium, no electrochemical potential gradient is present

across the electrode-electrolyte interface and the electrochemical potentials at the solid, $\tilde{\mu}_{\text{int}}^{sol}$, and liquid, $\tilde{\mu}_{\text{int}}^{liq}$, interface are equal to one another, i.e. $\tilde{\mu}_{\text{int}}^{sol} = \tilde{\mu}_{\text{int}}^{liq}$. According to this electrochemical equilibrium condition, one can derive the famous Nernst equation that correlates the equilibrium electrode potential, E_{equ}, with the concentrations of the species present, and can be written in the general form as [Bar01]:

$$E_{equ} = E_0^{'} + \frac{RT}{nF} \cdot \ln\left(\prod (C_j)^{\upsilon_j}\right) . \tag{2.2}$$

Here, $E_0^{'}$ represents the formal potential that incorporates the activity coefficients, to address species concentrations, C_j, rather than activities that are often unknown. υ_j are the stoichiometric coefficients of the electrode reaction. According to the Nernst equation, a change in concentration of species at the electrode or variations in the system's temperature induce a potential change. Conversely, applying a different potential to the electrode shifts the equilibrium concentration of species at the interface and induces the flow of electrical charges until a new equilibrium is established. The theoretically available Gibbs-free energy of an electrochemical system, ΔG, is linked to the equilibrium potential as follows [Bar01]:

$$\Delta G = -nFE_{equ} . \tag{2.3}$$

In the following, we consider the non-equilibrium case when, for example, an electrocatalytic reaction occurs at the electrode surface.

2.1.3 Butler-Volmer equation (Kinetics)

Let us consider the case when the electrochemical system is at non-equilibrium and electrical charges flow due to, for example, an electrochemical reaction. Such an electrochemical reaction typically involves a number of steps, as schematically shown in Figure 2.2, for example, the mass transport to and from the electrode surface, the adsorption/desorption of chemical species and the actual charge transfer across the electrode-electrolyte interface that can involve a number of reaction intermediates and different reaction pathways. The slowest of these intermediate steps is called the rate-determining step and determines the overall turnover frequency (i.e. number of chemical transitions per time unit).

For a single step one-electron reaction of the form $X + e^- \leftrightarrows Y$, where X is being reduced and Y is being oxidized, the net rate, r, of an electrode reaction is given as $r = \frac{i}{nFA}$. Here, i is the current, n is the stoichiometric number[1], F is the Faraday constant and A

[1]Note that n can describe either the number of electrons passed per reactant molecule or the number of moles of electrons per mole of reactant [Bar01].

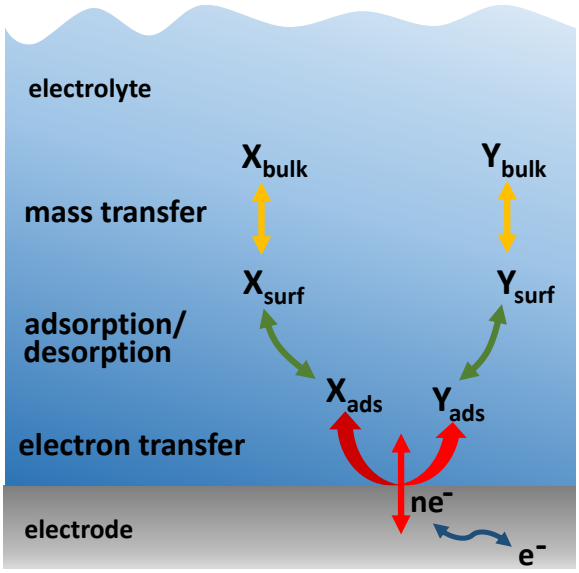

Figure 2.2. *Illustration of different steps affecting electrochemical reaction kinetics. Image adapted from Ref. [Bar01].*

is the electrode surface area [Bar01]. By measuring the current per unit area, one can determine the reaction rate that is potential-dependent. Considering the empirically found Arrhenius equation for the potential-dependent forward and backward rate constants, one can derive the famous Butler-Volmer equation as a function of applied overpotential[2], $\eta = E - E_{equ}$ [Bar01]:

$$i = i_0 \left[\frac{C_X(0,t)}{C_X^*} \exp \frac{-\alpha F \eta}{RT} - \frac{C_Y(0,t)}{C_Y^*} \exp \frac{(1-\alpha) F \eta}{RT} \right] , \tag{2.4}$$

where C_X^* and C_Y^* denote bulk concentrations. $C_X(0,t)$ and $C_Y(0,t)$ are the respective time-dependent surface concentrations. i_0 denotes the exchange current and α is the transfer coefficient that characterizes the symmetry of the energy barrier between reactant and product. Figure 2.3 illustrates the current trends as a function of overpotential according to the (Butler-Volmer) current-overpotential equation. While for small overpotentials an exponential increase in current is registered, for large overpotentials, the current saturates since mass transport plays the critical role as the rate-determining step. Considering no mass transport limitations, the influence of the pure rate constants can be extracted and visualized as in Figure 2.3B. Larger standard rate constants are ad-

[2]The overpotential, η, is the potential difference between the applied electrode potential, E, and the thermodynamic equilibrium potential, E_{equ}, required to drive an electrochemical reaction.

vantages, as they require lower overpotentials to reach equivalent current densities. For example, the ORR suffers from slow reaction kinetics revealed by low standard rate constants. Electrocatalytic research aims to understand how surface nanostructure/material composition and activity, i.e. increased rate constants, are related to rationally design improved electrocatalysts in the future.

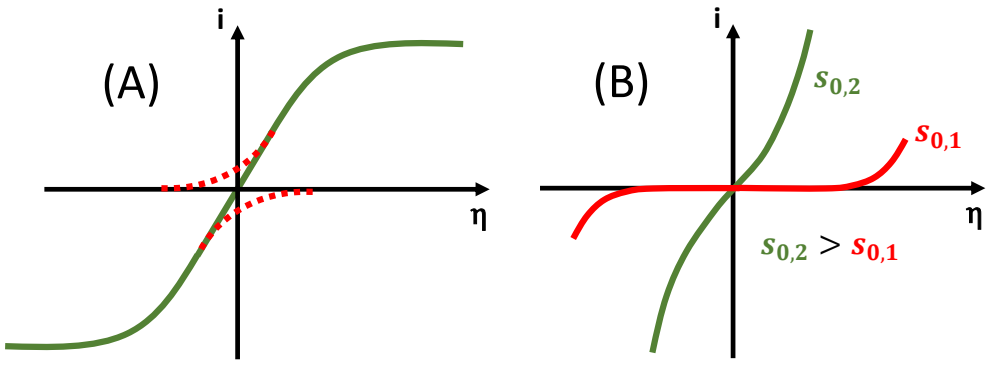

Figure 2.3. *(A) Current, i, plotted as a function of overpotential, η, according to the Butler-Volmer current-overpotential equation 2.4. (B) Excluding mass transportation as the limiting factor, the influence of different standard rate constants, s_0, on the $i(\eta)$ curve is visualized. Image adapted from Ref. [Bar01].*

2.1.4 Cyclic voltammetry

Cyclic voltammetry (CV) correlates flowing electric charges, i.e. number of electrons that pass through the electrode per unit time, as a function of applied potential. The measured current provides an 'averaged' response from the electrode surface. During CV measurements, the applied electrode potential is linearly ramped up and down as a function of time in a sawtooth pattern (Figure 2.4A) and the current is recorded as a function of the applied potential. In the case of a redox couple in solution, a typical CV shows oxidation and reduction peaks[3], as shown in Figure 2.4B. Scanning from E$_-$ toward more positive potentials, non-faradaic currents can be detected due to double layer charging, followed by an exponentially increasing (faradaic) anodic current due to the oxidation of redox species at the electrode surface and concomitant charge transfer across the interface. As the near-surface region is depleted of reactants, diffusion processes become the limiting factor for the oxidation of redox species and the current peak maximum is reached at

[3]Note that there are different current sign and CV plotting conventions for US and IUPAC [Elg18]. Here, we use the IUPAC convention, where oxidative currents are positive and the applied potential is plotted from negative to positive values (from left to right).

E_a. Further potential up-scan increases the depletion region at the surface slowing down mass transport further, which manifests itself in a decreasing current. After changing the sweep direction at E_+, the oxidized redox species at the electrode surface is reduced and a cathodic (reduction) peak is seen.

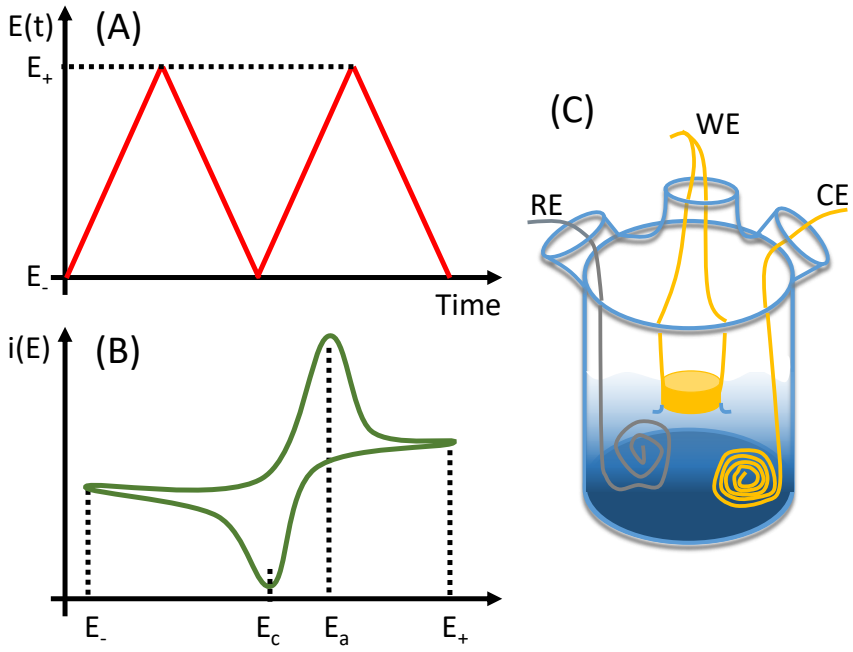

Figure 2.4. *(A) Applied linear potential sawtooth curves during up- and down-scans during CV. The slope defines the scan rate in mV/s. E_- and E_+ denote lower and upper potential boundaries, respectively. (B) CV of a redox couple in solution (for one up- and down-scan, i.e. single cycle). E_c and E_a are the cathodic and anodic peak positions, respectively. (C) Schematic of a three-electrode setup in a glass-cell configuration. WE, RE and CE account for the working, reference and counter electrode, respectively.*

The standard experimental setup to perform electrochemical measurements and record CVs is a three-electrode setup as schematically depicted in Figure 2.4C. The working electrode (WE) is the electrode interface under investigation. A second electrode, the reference electrode (RE), is required to set the applied potentials at the WE with respect to this stable RE interface. The RE should be stable, non-polarizable, have a constant reference potential and exhibit high impedance. The high impedance is required to minimize possible current flow across the RE (cf. Equation 2.4) in order to maintain a constant potential. Therefore, a third electrode is introduced as a current collector and is referred to as counter electrode (CE). At the CE, electrochemical reactions or processes occur, which is why the CE should be chemically stable and be positioned such as to minimize possible interference of the emerging reaction products (at the CE) with the WE. The RE

should be located close to the WE to minimize the potential iR drop between WE and RE. There are numerous different RE available and their usage depends on the particular electrochemical system under investigation. The standard hydrogen electrode (SHE) is defined as a Pt electrode in contact with an acidic solution, unity of hydrogen ion activity and hydrogen gas of 1 bar pressure bubbling around the Pt electrode [Bar01]. The absolute SHE potential at room temperature of 298.15 K amounts to -4.44 eV vs. vacuum level [Tra86]. In this work, the reversible hydrogen electrode (RHE) and the Pd-H electrode are used as REs. The potential conversion scale is illustrated in Figure 2.5. For the RHE, the proton concentration does not equal to 1 (as for SHE) and the RHE scale depends on the pH of the electrolyte according to RHE = SHE - 59 mV * pH. The Pd-H electrode consists of a Pd-wire that is filled with hydrogen. In an electrolyte of pH = 1, the Pd-H electrode approximately equals SHE. For example, 0.941 V vs. Pd-H corresponds to 1 V vs. RHE (Figure 2.5).

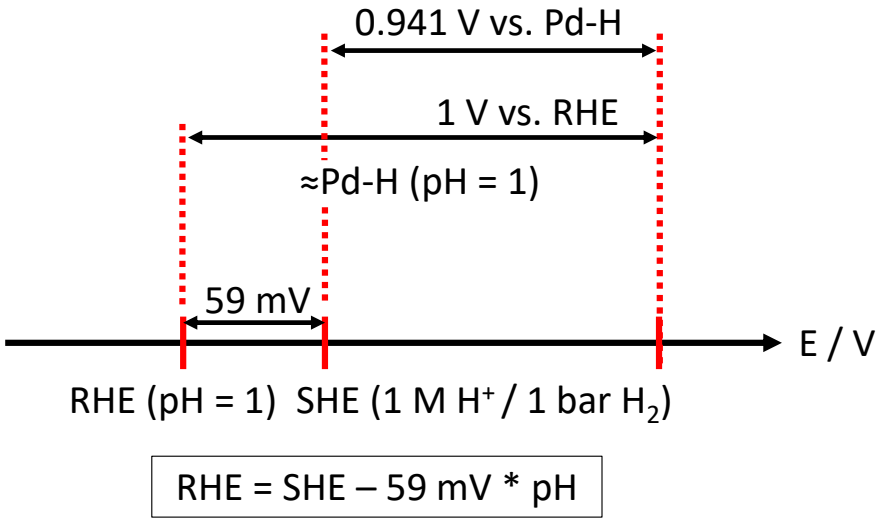

Figure 2.5. *Relation between the standard SHE reference electrode potential (equilibrium point of H_2/H^+) and the RHE and Pd-H reference electrodes employed in this work. A conversion example from RHE (pH = 1) to Pd-H (pH = 1) is given for 1 V vs. RHE.*

The applied potential of the WE is set with respect to the RE by a potentiostat [Hic42]. This device retains the designated WE potential relative to the RE by regulating the current flow between the WE and CE via an internal control loop that applies a bias voltage between WE and CE.

The CV methodology allows, in general - wherever charges can be counted, the detection and characterization of different electrochemical processes, such as surface oxidation/reduction (Chapter 3), molecular adsorption/desorption (Chapter 4), redox reactions of species in solution (Figure 2.5) or reorientation and reorganisation of adsorbed ions (Chapter 4). However, additional chemical specificity and/or nanoscale chemical understanding is often desired and, as we will see throughout this thesis, can be provided by advanced spectro-electrochemical approaches.

2.2 Electrocatalysis

In catalysis, chemical reactions are accelerated by catalytic materials that offer alternative reaction pathways with reduced activation energy barriers and that are not consumed during the reaction. Electrocatalysis deals with catalytic materials, i.e. electrocatalysts, that participate in and accelerate electrochemical reactions. Figure 2.6 illustrates such energy barriers for an (electro)chemical reaction via an intermediate reaction step. First, the reactant, A, has to overcome the first energy barrier to form the reaction intermediate, B, that subsequently has to pass the second energy barrier to transfer to the product state, C. Catalysts can lower either one or both energy barriers, possibly in an asym-

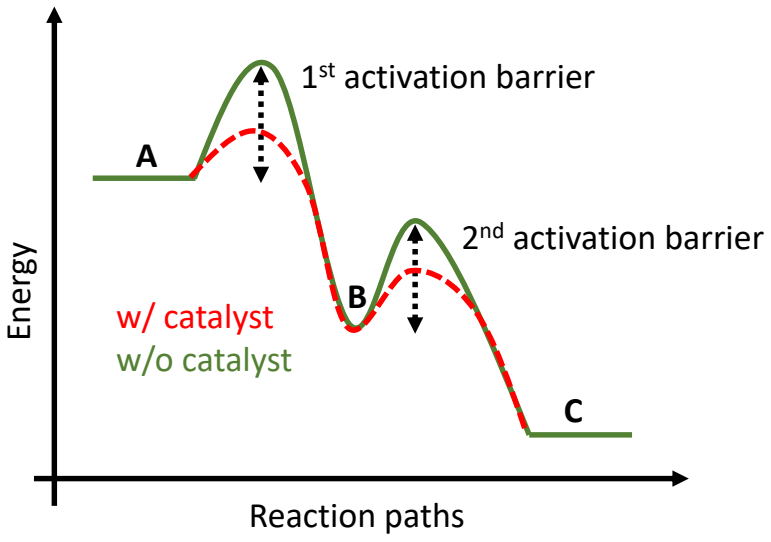

Figure 2.6. *Illustration of the chemical reaction pathways with (red) and without (electro)catalyst (green), where a reactant, A, is transformed to a reaction intermediate, B, before being transformed further to the final product, C. In this example, two activation energy barriers have to be overcome.*

metric way, for specific reaction pathways depending on the electronic properties of the catalyst [Tho14]. The electronic surface structure determines the adsorption/desorption properties for the reaction intermediates. The Sabatier principle, applied in the field of (electro)catalysis, states that the adsorption energies of the reaction intermediates should neither be too strong nor too weak. If too strong, the catalyst is poisoned by the adsorbate, as for example in the case of CO adsorption on Pt [Got98]. If too weak, the intermediate cannot efficiently attach to the catalytic surface. The Sabatier principle is often visualized in Volcano plots. In Figure 2.7, an example volcano plot for the hydrogen evolution reaction (HER) is shown, in which the exchange current density is plotted as a function of the hydrogen adsorption energy (as the descriptor) for different transition metals [Tym16]. While Pt, for example, binds the hydrogen atom slightly too strongly compared to the volcano maximum by around 0.1 eV, Au binds the hydrogen atom so weakly that the exchange current density is significantly lower compared to the theoretical determined volcano maximum.

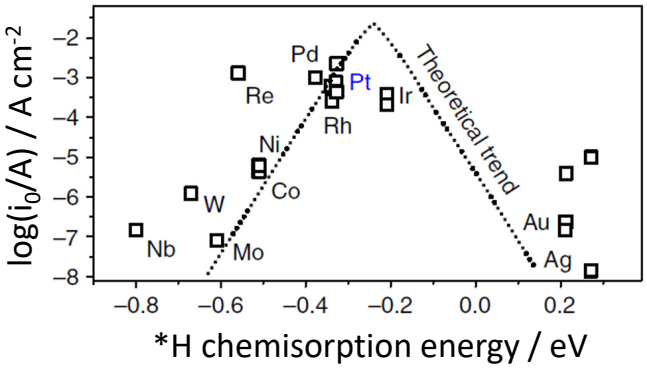

Figure 2.7. *Example of a volcano plot for the HER: Exchange current densities, i.e. exchange current, i_0, per area, A, for different transition metals plotted as a function of hydrogen, *H, chemisorption energies. Note the difference between area and ampere unit. Image adapted from Ref. [Tym16].*

It is not only the material that determines the catalytic activity of an electrode, but also its nanoscale surface structure. Already in 1925, Hugh Stott Taylor suggested that it is not the complete surface that is catalytically active [Tay25], but only certain spots on the surface, the active sites. Such active sites are often surface defects, as for example step edges or kink sites with specific coordination numbers, i.e. a specifc number of nearest neighbors [O'M14]. Electrocatalysts can have a complex nano- and/or atomic-structure that provides the optimal binding sites for the reactants and reaction intermediates. The local atomic surface composition and atomic arrangement defines the electronic structure

of the surface sites with optimal binding energies for the reaction intermediates (according to the Sabatier principle). One can differentiate, in addition to the surface geometry [CV15], between the ligand, ensemble and lattice strain effects. The ligand effect describes the effect of introducing (possibly different) atoms ('ligands') to the atomic active site or changing the number of nearest neighbors (and thus changing the number of 'ligands') [Bli07]. For example, Stephens et al. introduced a subsurface Cu submonolayer to Pt(111) tuning the OH binding energy for the ORR [Ste11]. The ensemble effect describes the grouping of surface (ad)atoms in ensembles and thus changing the number of neighboring atoms, which effects the electronic surface site configuration [Mar01]. For instance, Maroun et al. showed that Pd monomers on Au(111) are sufficient for CO oxidation, while Pd dimers are required for hydrogen adsorption [Mar01]. Lattice strain can also influence the electronic surface properties and thus the adsorption energies of reaction intermediates. For example, Escudero-Escribano et al. studied Pt-lanthanide electrodes, in which the contraction of lanthanide leads to strain in the Pt overlayer and thus to a change in ORR activity [EE16]. It is important to note that the different effects typically overlap and are not independent from each other. For example, in the case of CO adsorption on Pt overlayers on Ru, Schlapka et al. showed that the electronic influence of the substrate dominates for up to 3 layers, while strain effects influence CO adsorption energies even for thicker Pt overlayers [Sch03]. It is the electronic structure of the surface site that determines the active (defect) site adsorption properties and therefore the reactivity. To enhance material performance, maximizing the available number of active sites is often sought after [She17], for example, on electrocatalyst nanoparticles. The establishment of rational design principles for such active nanoparticles requires (i) identification of the most active surface structures and (ii) understanding of the local reaction mechanisms, i.e. of the nanoscale chemistry.

2.3 Gold electro-oxidation and gold oxide reduction

2.3.1 Gold - a noble metal

Gold (Au) is a transition metal located in the 11^{th} group of the periodic table, together with the other coinage metals silver (Ag) and copper (Cu). The orbital structure accounts to [Xe] $4f^{14}$ $5d^{10}$ $6s^{1}$. The melting point of Au lies at around 1337 K, the diameter of the Au atom is 2.884 Å and the lattice constant is 4.0786 Å [Kib03]. Au is a soft and shiny yellow metal. Its shininess is due to the good light reflectivity, as electrons in the Au can be approximated as a free electron gas that can follow easily the incoming visible light (electromagnetic waves). The yellow color originates from a relatively small bandgap

between the 6s- and 5d-orbitals that allow (complementary) blue light to be absorbed [Sch05].

Au crystallizes in a face-centered cubic (fcc) structure (Figure 2.8A). The low-index Au single crystal surfaces, Au(111), Au(100) and Au(110) reconstruct at room temperature [Bar90]. The single crystalline Au surfaces and their potential-dependent lifting of the reconstruction have been extensively studied, for example by Hamelin and Martins [Ham96a, Ham96b]. The atomic structure of the Au(111) single crystal surface, relevant to this work, is illustrated in Figure 2.8B. The Au(111) surface is prepared according to Clavilier and co-workers by flame-annealing under a stream of inert Ar gas [Cla79]. Figure 2.8C shows a glowing Au(111) single crystal during flame-annealing, as prepared in this work, placed on a glass ceramic plate and in a stream of Ar. Au in general is

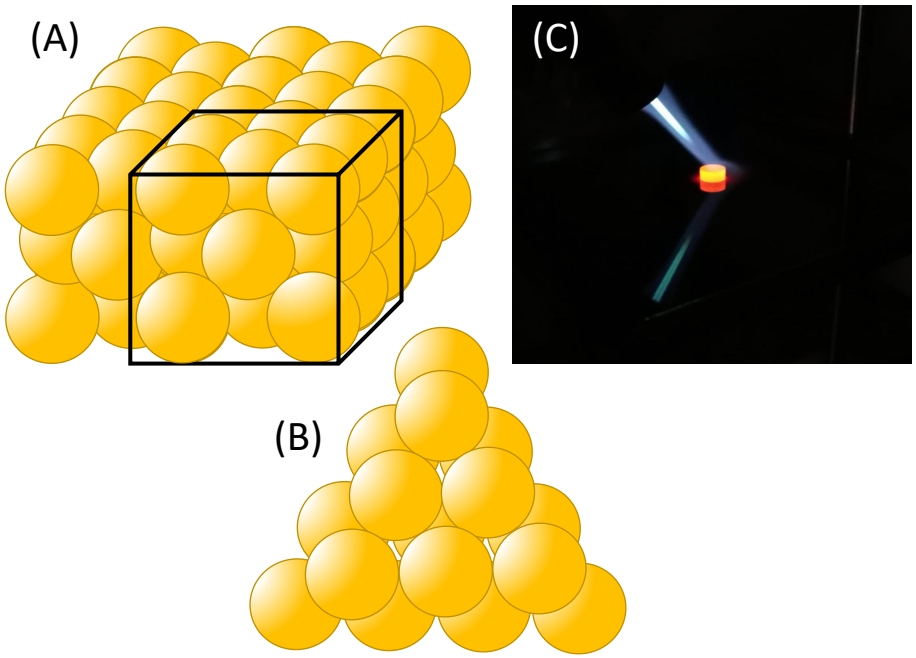

Figure 2.8. *(A) Face-centered cubic (fcc) single crystal structure. (B) Cutting the fcc single crystal along the plane defined by the (111) normal vector returns the Au(111) surface structure with threefold symmetry. (C) Photo taken during flame-annealing of a Au(111) single crystal in a butane flame in preparation for EC-TERS measurements.*

chemically inert, i.e. Au is resistant to most acids and does not corrode under ambient conditions at room temperature as Au is not oxidized by oxygen in the air (and therefore retains its shiny goldish color). However, at sufficient positive applied potentials, Au can be electrochemically oxidized by splitting water, as discussed in the following.

2.3.2 Metal oxidation/reduction mechanisms

The electro-oxidation mechanims of metals can in general be classified into five categories according to Conway [Con95]:

Metal dissolution and precipitation The metal is dissolved into the electrolyte and the metal cation is solvated by the solvent electrolyte. Metal dissolution is followed by the hydrolysis of the solvated metal cation and subsequent precipitation of the metal (hydr)oxide on the surface, forming a weakly adherent oxide or hydroxide film.

Nucleation and growth The oxide film is formed directly at the surface without prior dissolution of the metal as solvated cation. The oxide film grows after initial nucleation at energetically favored surface sites.

Sub-monolayer adsorption and place-exchange After initial formation of a (sub) monolayer of surface-adsorbed OH- or O-species, further growth involves the interchange between surface metal atoms and O/OH-species to form a full 2D oxide film. The electric field-dependent interchange between metal atoms and O/OH-species that exchange sites during surface oxidation and vice versa during electro-reduction is called place-exchange mechanism.

Mott-Cabrera mechanism Due to a high electric field across the insulating oxide film, further oxide growth can either occur by metal ion migration from the bulk metal to the electrolyte or by migration of O/OH-species from the electrolyte through the oxide film to the underlying metal. Accordingly, the oxide film grows in thickness either at the AuOx/electrolyte interface or at the bulk Au electrode/AuOx film interface.

Combination of mechanisms For Pt or Au, for example, place-exchange and Mott-Cabrera mechanisms are combined as discussed in the following.

Figure 2.9 shows the CV of a Au(111) bead single crystal in 0.1 M sulfuric acid (H_2SO_4). At low potentials around 0.4 to 1.0 V vs. RHE, sulfate anions are adsorbed at the Au surface [Shi94]. The sharp peaks at around 1.1 V vs. RHE correspond to the transition from a disordered sulfate adlayer to an ordered sulfate layer, likely incorporating also hydronium ions or water molecules at the (111) terraces [Mag92, Cue00]. At around 1.3 V vs. RHE, the Au oxidation commences, which can, in acidic media, be described with the following reaction equation:

$$x \cdot Au + y \cdot H_2O \leftrightarrows Au_xO_yH_z + (2y - z) \cdot H^+ + (2y - z) \cdot e^- \,, \tag{2.5}$$

where water is split to form a gold oxide (AuOx $\hat{=}$ $Au_xO_yH_z$) and protons are released into the electrolyte. The Au oxidation between 1.3 and 1.5 V vs. RHE corresponds to the oxidation of surface defects [Kol00, Zhu13], such as step edges, kinks or larger nanoscale defective structures. The peak at around 1.6 V vs. RHE is assigned to the oxidation of Au(111) terraces [Zhu13]. During the cathodic scan, the reverse AuOx electro-reduction starts at around 1.25 V vs. RHE and exhibits a single cathodic peak. The integrated charges for oxidation and reduction are approximately the same [Zhu13]. Slight discrepancies between oxidation and reduction charges in the order of 5 to 30 µC cm^{-2} presumably originate from the surface roughening resulting from the place-exchange between Au and O/OH-species (cf. Figure 2.13A,B) [Sch97] and concomitant Au dissolution [Che13].

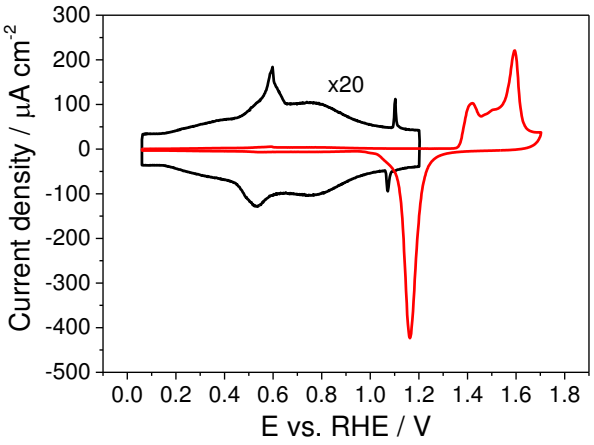

Figure 2.9. *CVs of a bead Au(111) single crystal electrode in 0.1 M H_2SO_4 (scan rate = 50 mV/s) to 1.2 (black) and to 1.7 V vs. RHE (red). The black CV is increased in y by a factor of 20.*

For Au surfaces in general, there are a number of potential-dependent steps with increasing positive applied potentials toward thick oxide film growth that have to be considered for the oxidation and reverse reduction processes [Con95]:

- Adsorption of water or other solvent molecules at the electrode surface that modify the electronic structure of the available surface sites for the following anion adsorption step.

- Adsorption of anions, e.g. (bi)sulfate ions, at the surface and formation of an ordered adlayer (in H_2SO_4 electrolyte) possibly including also H_2O or H_3O^+ molecules [Mag92, Cue00]. For the chemisorption of anions, charge-transfer between anion and metal surface occurs. The anion adsorption strength can delay the onset of

surface oxidation due to surface site blocking [Con95]. Sulfate ions adsorb strongest on Au(111), due to geometrical matching of the tetrahedral ions and the trigonal symmetry of the (111) surface plane [AK86, AK87].

- OH- or O-species are deposited at the metal surface forming a (sub)monolayer. Thereby, OH- and O-species compete with the previously adsorbed anions for available surface sites.

- A 2D oxide film is then formed by the place-exchange mechanism, where metal surface atoms and O/OH-species are interexchanged, i.e. Au atoms are pulled out of the surface while O/OH-species are incorporated into the first few layers. The place-exchange between Au atoms and O/OH-species is apparently energetically more favorable than maintaining a plain submonolayer of O/OH-adsorbates. During this surface rearrangement the remaining anions at the surface are desorbed.

- The 2D oxide growth then transitions into a 3D growth of thick oxide films according to the Mott-Cabrera mechanism, where the high electric field gradient (in the order of 10^8 to 10^9 V m^{-1} [TF05]) across the insulating oxide film enable ion migration across the growing oxide layer.

During bulk oxidation above ca. 1.95 V vs. RHE, the OER is initiated. Koper and coworkers found that the oxygen atoms from the surface oxide decisively contribute to the OER [DM13]: At low OER overpotentials, O_2 is formed from oxygen originating from the oxide structure, while at higher overpotentials, both oxygen from water and from the oxide structure compose the evolved O_2. The oxygen removal from the oxide surface can be considered as a surface reduction during water oxidation and concomitant evolution of molecular oxygen. As a consequence, the surface oxide reduction mechanism, the oxide composition and the nanoscale structure of the oxidized Au surface have direct implications on the OER reactivity. However, the exact nature of the oxide species present at oxidized Au surfaces is not clear [Peu84, Des86, Kon07] and both Au surface oxidation as well as AuOx reduction processes are not yet fully understood [Li15]. For example, in acidic solution the partial discharge of water is suggested to result in the formation of adsorbed $OH^{(1-\delta)}$ species, where δ is a partial charge, that are subsequently fully discharged accompanied by anion desorption and place-exchange between Au atoms and O/OH-species [Con95, Rod03b]. However, such adsorbed OH-species have to date not been observed in acidic media [Zhu13, Li15], suggesting different oxidation mechanisms as a function of pH. The scarce availability of operando spectroscopic evidence of reaction intermediates during Au electro-oxidation/reduction in acidic media as well as the complex interpretation of broad shape spectroscopic features have hindered a clear judgement

of the intermediates as well as products [Des86, Li15].

All in all, the oxidation of Au can be considered a complex process that depends on the crystallographic orientation [AK86, AK87], pH of the electrolyte [Con95], the type of adsorbing ions [Con95] and the applied potential-range [TF05]. Before passing on to the next section, it is noteworthy to emphasize that the Au oxidation and AuOx reduction and the interpretation thereof is further complicated by the dissolution of Au, as reported by the Mayrhofer group [Che13], which inevitably modifies the Au surface. In addition, the specific local surface geometry including nano-defect structures are expected to contribute to the complexity of the electrochemical oxidation/reduction process and the formation of certain AuOx species.

2.4 Scanning tunneling microscopy

Scanning probe microscopy (SPM) techniques utilize a physical probe that is scanned across the sample surface imaging its surface topography or topography-related properties, such as the local density of states (LDOS), on the nanometer or even atomic level [Voi15, Set17]. The fine tuning of surface location with (sub-)nanometer precision is made possible by piezoelectric actuators. The first SPM technique - the scanning tunneling microscope (STM) - was invented by Binning and Rohrer at IBM in 1982 [Bin82a, Bin82b] who were shortly afterwards awarded the Noble Prize [Bin87]. An STM uses an atomically sharp metallic tip that is approached in close vicinity in the order of 1 nm to a conductive (or semiconductive) surface until quantum mechanical electron tunneling across the vacuum (air) gap results in a measurable tunneling current. This tunneling current depends exponentially on the tip-sample distance and can be regulated by a feedback system, enabling the imaging of the LDOS of the surface probing indirectly the surface topography. The TERS technique, discussed in Section 2.5, uses STM as an essential part to position the TERS probe (STM probe) precisely at the desired surface location [Jia16]. In the following, we discuss STM as well as the underlying quantum mechanical effect of electron tunneling.

2.4.1 Tunneling effect

The tunneling effect is a quantum mechanical phenomenon that is the basis for STM. The tunneling effect states that particles such as electrons can pass through an energy barrier of a certain height even if the particle's energy is lower than this energy barrier. From a classical point of view, it is not possible to overcome the energy barrier, since the

particle's energy is not sufficient. But quantum mechanics predicts a finite probability to overcome the energy barrier according to an overlap of wave functions if the tip-sample distance is small enough (less than or equal to 1 nm).

A full conceptual description of the tunneling process was developed by Bardeen and later applied by Tersoff and Hamann to describe electrons tunneling between two solid metals [Bar61, Ter83]. Essentially, their conceptual formalism can be simplified to the following form of the tunneling current, i_t [Our13]:

$$i_t \approx \rho_{surface} \cdot \rho_{tip} \cdot \frac{E_{bias}}{d} \cdot \exp\left(-D \cdot \sqrt{\vartheta_{eff}} \cdot d\right) . \tag{2.6}$$

Here, $\rho_{surface}$ and ρ_{tip} describe the electronic densities of states for the sample surface and the STM tip, respectively. E_{bias} is the applied bias voltage between sample and tip. D is a constant, ϑ_{eff} is the effective energy barrier height (that is related to the work function of sample and tip) and d is the tip-sample distance. The tunneling current depends exponentially on the gap distance, d, which makes STM very sensitive in z-direction.

2.4.2 STM method

The STM technique is based on the tunneling effect [Sch98]. An atomically sharp metal tip is brought in close proximity to a conductive or semiconductive sample surface. Applying a bias voltage, E_{bias}, between sample and tip shifts the corresponding Fermi level in such a manner that electrons tunnel from the tip to the sample or vice versa (see Figure 2.10). The resulting tunneling current in the range of pA to nA is controlled by a feedback system. Figure 2.11 illustrates the STM electronic components important to understand the basic working principle of this feedback system. In the constant current mode, the feedback system adjusts the tip-sample distance (in z) with potential-controlled piezo-elements in such a way that the tunneling current is kept constant at the predefined current setpoint. Scanning across the sample surface (in x,y) that contains variations in the LDOS and recording the adjustments of the piezo-electric elements required to maintain a constant tunneling current results in an image of the LDOS [Voi15]. High voltage amplifiers apply the required voltages to the piezo-electric elements to move the tip in x, y and z. Besides the constant current mode, another often utilized STM operation mode is the constant height mode, where the tip-sample distance is locked and any further topography change results in changes of the tunneling current according to Equation 2.6 [Our13].

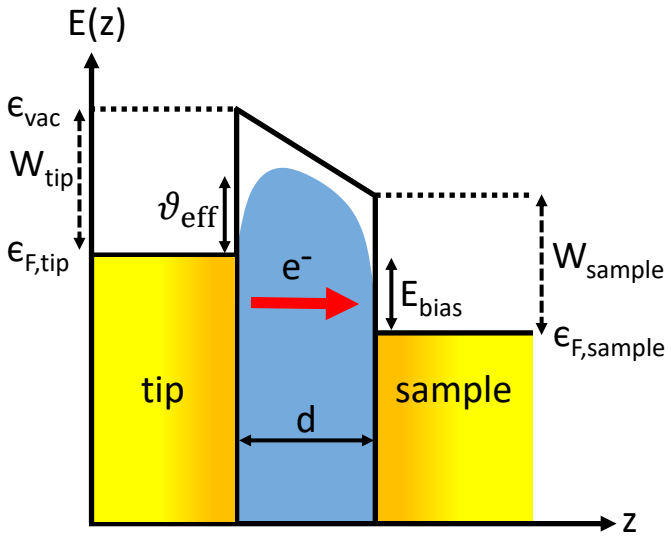

Figure 2.10. *Energy diagram of a tunneling junction composed of the STM-tip and the sample surface with a gap distance of d. W_{tip} and W_{sample} represent the corresponding work functions of tip and sample. The vacuum level is denoted as ϵ_{vac}. ϑ_{eff} is the effective energy barrier that depends on tip and sample material work functions as well as the medium in between. $\epsilon_{F,tip}$ and $\epsilon_{F,sample}$ are the Fermi levels of the tip and sample, respectively. Image adapted according to Ref. [Our13].*

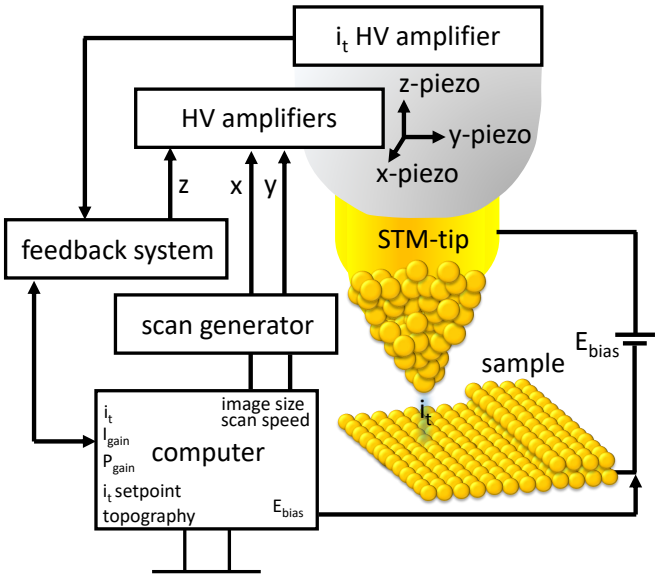

Figure 2.11. *Schematic of the STM feedback system of a tip scanner and the various high voltage (HV) amplifiers to position the piezo-electric elements and to read out the pA-nA tunneling currents with a current-voltage converter.*

Nanometer spatial resolution is routinely achieved in STM measurements and even atomic resolution is possible [Fes17]. The high vertical STM sensitivity in the order of Å stems

from the exponential current-distance dependency as seen in Equation 2.6. The experimental lateral spatial resolution depends on the tip-apex-dimensions, the precision of the piezo-elements and the STM-setup stability.

2.4.3 Electrochemical STM

STM conducted in an electrolyte under potential control is referred to as electrochemical scanning tunneling microscopy (EC-STM). EC-STM was introduced in 1986, demonstrating that atomic resolution can be achieved in aqueous electrolytes [Liu86, Son86]. EC-STM is the combination of an STM and a three-electrode electrochemical setup (Figure 2.12). A bipotentiostat regulates the applied potentials to the sample WE as well as to the STM-tip, which can be considered a second WE. The potentials are referenced versus a RE and a CE acts as current collector. Importantly, the STM-tip has to be electronically isolated from the electrolyte to reduce faradaic and non-faradaic[4] currents at the STM-tip that are typically much larger (µA to mA) than the tunneling current. Ideally, only the very end of the tip apex is left free from the coating material, limiting leakage currents to around 50 pA or less.

EC-STM setup

The EC-STM setup utilized in this work is an essential part of the EC-TERS setup. The EC-STM device is a Keysight Technologies GmbH STM 5420, former Agilent (STM-controller model N9610A) equipped with a bipotentiostat. The EC-STM is located on an x-,y-stage (for laser focusing, Steinmeyer Mechatronik GmbH, 3 nm step precision, max. range = 10 mm), which in turn is positioned on an optical air table (TMC Technical Manufactoring Corporation). The STM tip-scanner (model N9700C) has an extended nose to accommodate relatively long EC-STM tips of 1 to 1.5 cm length required to fit the stringent EC-TERS space constraints and to provide additional tip stability. The Au-tips are electrochemically etched (see Section 2.5 for further details) to form sharp and well-defined cone-shaped Au-tips that provide TERS enhancement. The Au-tips are electronically isolated utilizing transparent Zapon wax. Pt or Au wires are used as CEs and are freshly prepared by flame-annealing and rinsing with MilliQ water before usage. For acidic electrolytes, a hydrogen-loaded Pd wire (Pd-H) is employed as RE. The EC-STM is controlled by PicoView 1.14 software (Keysight Technologies GmbH).

[4]Faradaic currents are due to electrochemical reactions at the electrode. Non-faradaic currents refer to double layer charging and charge transfer associated with molecular reorientation or adsorption/desorption processes.

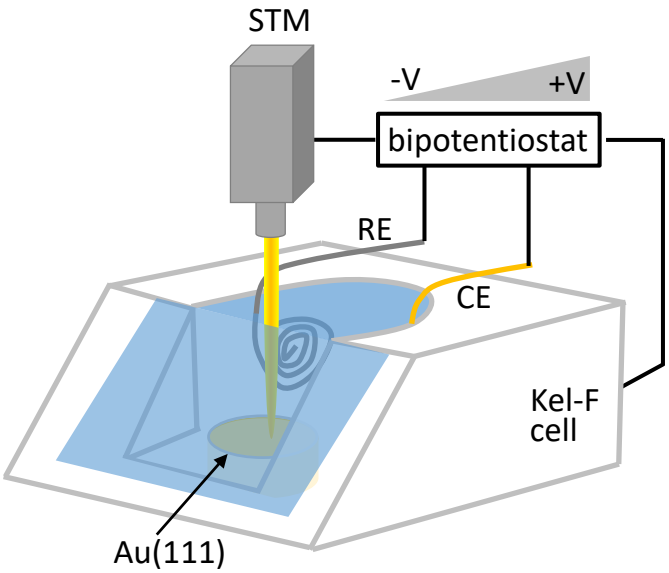

Figure 2.12. *Schematic of the EC-STM setup with the electrochemical Kel-F® cell using a bipotentiostat to apply the desired potentials with respect to the reference electrode (RE) to both sample Au(111) electrode and Au EC-STM-tip. CE denotes counter electrode.*

Figure 2.13 shows EC-STM images of a Au(111) single crystal in 0.1 M H_2SO_4 recorded in our (spectro-)electrochemical Kel-F® cell with an electrochemically etched Au-tip. In Figure 2.13A, the Au(111) substrate was imaged after sample mounting at a potential of 1 V vs. Pd-H before surface oxidation/reduction cycles, showing flat and well-ordered terraces with a step edge of monoatomic height of about 3 Å. Figure 2.13B highlights the Au(111) surface structure after complete surface oxidation/reduction, portraying preferentially formed monoatomically high valleys and few monoatomically high islands. Our EC-STM setup provides the means to study nanoscale features even with long Au-tips required to accommodate the TERS optics.

2.5 Plasmon-enhanced vibrational spectroscopies

The field of optical spectroscopy describes how electromagnetic radiation interacts with matter. Optical spectroscopy seeks to understand the interaction of light with materials by comparing the excitation light irradiated onto a sample of interest and the detected electromagnetic signals after light-matter interaction(s). Three important examples for optical interaction processes are light absorption, light emission and light scattering.

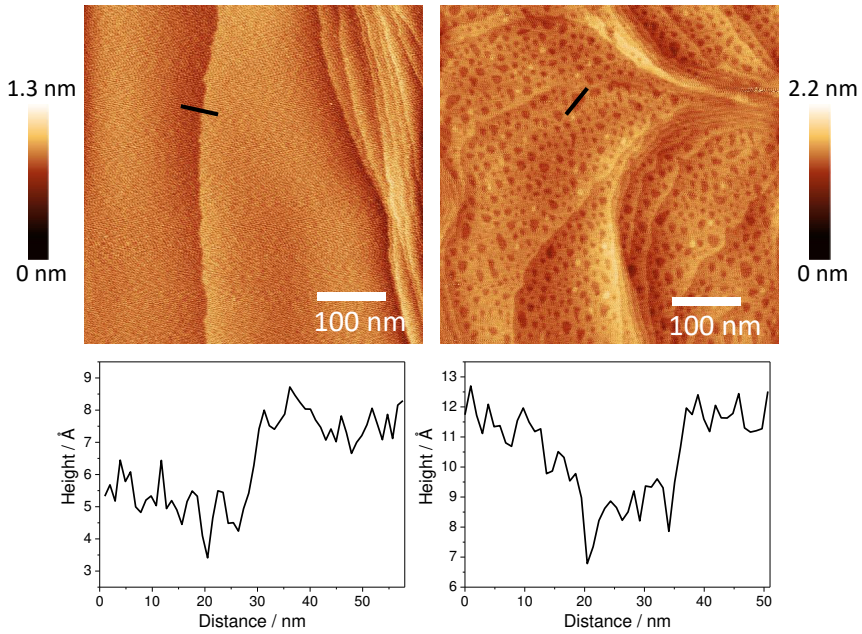

Figure 2.13. *EC-STM images of a Au(111) single crystal in 0.1 M H_2SO_4. (A) Recorded at a potential of 1.0 V vs. Pd-H before surface oxidation (Image size = 500 nm x 500 nm, 512 x 512 pixels, scan speed = 1 Hz, i_t = 1 nA, E_{tip} = 0.8 V vs. Pd-H). (B) EC-STM image recorded at a potential of 0.9 V vs. Pd-H after surface oxidation and subsequent reduction (Image size = 500 nm x 500 nm, 512 x 512 pixels, scan speed = 1.5 Hz, i_t = 1 nA, E_{bias} = 100 mV).*

During optical absorption, a photon of energy, $\hbar\omega$, excites a molecule from an energy level, S_0, to a higher energy level, S_1, if the transition is dipole-allowed, i.e. the photon can actually couple to the given transition [Le 09]. Electronic absorption, in which an electron is excited to a higher excited electronic state, is, for example, the basis of UV/Vis spectroscopy that probes the electronic states of molecules. In contrast, infrared absorption, in which a molecule is excited to a higher vibrational or rotational level within an electronic state, is the basis of IR spectroscopy probing the vibrational modes of molecules. The inverse process to optical absorption is stimulated light emission, where the incident photon interacts with the excited molecule to stimulate photon emission of the same frequency, polarization, direction and phase [Le 09]. In comparison, spontaneous light emission is an intrinsically probabilistic process that is due to vacuum fluctuations of the electromagnetic field that the excited state can couple to and spontaneously transit to a lower energy state by photon emission. Typical radiative lifetimes of some dye molecules are, for example, in the order of 1 to 100 ns [Le 09]. Most relevant for this work is the third main interaction type: light scattering, which is discussed in detail in the following paragraphs (based on Le Ru and Etchegoin [Le 09]). Thereafter, SERS, TERS

and SEIRAS are introduced as experimental approaches to provide signal enhancement necessary to study electrified solid-liquid interfaces.

2.5.1 Raman scattering

The Raman effect or Raman scattering is the basis for Raman spectroscopy, a certain type of a vibrational/rotational[5] label-free spectroscopic technique. The Raman effect was discovered by Chandrasekhara Venkata Raman in 1928, an Indian physicist who was shortly afterwards awarded the Noble Prize for his discovery [Ram28].

Light scattering is a simultaneously occuring instantaneous incident photon absorption and photon emission process. Therefore, compared to IR or fluorescence spectroscopy, no (individual) photon absorption is required [Le 09]. Figure 2.14 illustrates the energy diagrams for the three different types of scattering processes, in which the incoming photon transitions the molecule into a virtual state (i.e. no real molecular vibrational or electronic state) and concomitantly emits a photon. Rayleigh scattering describes the elastic scattering where incident and scattered photons have the same frequency (energy), but different direction and/or polarization. Raman scattering describes the inelastic scattering where the frequencies (energies) of the incident and scattered photons are different from each other. Depending on whether the scattered photon frequency is lower or higher than that of the incident photon, the inelastic scattering is referred to as Stokes or anti-Stokes Raman scattering, respectively. From a classical point of view, the instantaneous scattering process can be considered as the emission (scattered radiation) from an oscillating dipole that is induced by the incident electromagnetic field. The scattering process can, in principle, be fully deduced from quantum mechanics. In the following, however, we stick to the classical picture and the interested reader is referred to specialized literature for an in-depth quantum mechanical derivation [Le 09].

An oscillating dipole can be considered as two charges with opposite sign, $\pm q$, that oscillate with a small amplitude, $x(t) = x_0 \cdot cos(\omega \cdot t)$ along, for example, $\vec{e_x}$ [Le 09]. ω denotes the angular frequency. The oscillating dipole is then $\vec{p}(t) = q \cdot x(t) \cdot \vec{e_x} = q \cdot x_0 \cdot cos(\omega \cdot t) \cdot \vec{e_x}$. The amplitude, $q \cdot x_0$ in units of [Cm], is called dipole moment. As moving charges create electromagnetic fields, such oscillating dipoles radiate photons at an energy $\hbar\omega$.

We can describe the induced dipole moment, $\vec{u}$, due to the presence of an external electric

[5]Rotational bands are typically found below 150 cm^{-1}. We refer only to vibrational spectroscopy from here onward, but note that, in general, molecular rotations can also contribute to Raman scattering.

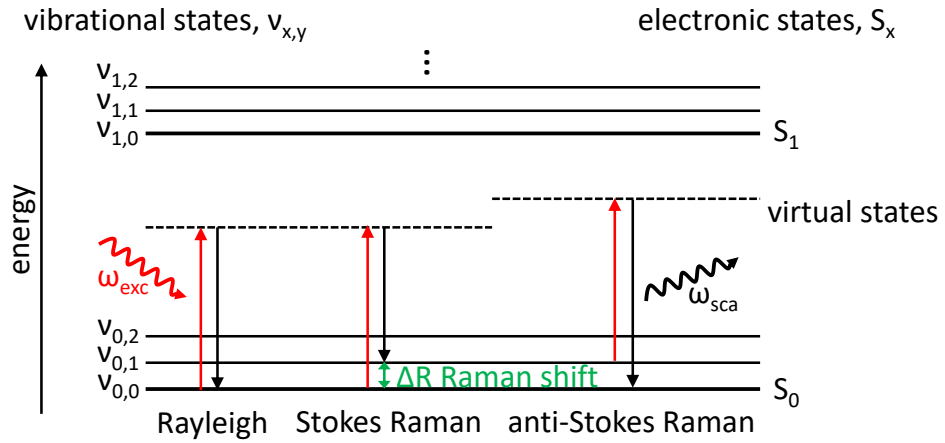

Figure 2.14. *Energy diagram visualizing the difference between Rayleigh, Stokes and anti-Stokes Raman scattering of molecules. ω_{exc} and ω_{sca} denote the excitation and scattered photon frequency, respectively. ΔR is the energy difference that characterizes the Raman shift.*

field, $\vec{\epsilon}$, as follows:

$$\vec{u} = \beta \cdot \vec{\epsilon}. \tag{2.7}$$

Here, β, the proportionality factor, is the polarizability tensor with the general rank of two. Polarizability describes the extent of which electrons in a molecule respond to the presence of an external electric field. In general, molecules with a larger number of 'free' electrons are typically more easily polarizable. Upon molecular vibration, subtle perturbations of the molecular structure are induced and result in small changes in polarizability. The polarizability tensor, β, can be expressed according to the Taylor expansion in the normal mode coordinates $(g_v, g_w, ...)$, which are associated to the corresponding molecular vibrational frequencies $(\omega_v, \omega_w, ...)$, as [Le 09]:

$$\beta = \beta_0 + \sum_v \left(\frac{\partial \beta}{\partial g_v}\right)_0 \cdot g_v + \frac{1}{2} \cdot \sum_{v,w} \left(\frac{\partial^2 \beta}{\partial g_v \cdot \partial g_w}\right)_0 \cdot g_v \cdot g_w + \dots, \tag{2.8}$$

where β_0 is the polarizability at equilibrium. Under the assumption of only small polarizability perturbations, we can neglect quadratic and higher-order terms of Equation 2.8 and write for a specific normal mode, l:

$$\beta_l = \beta_0 + \left(\frac{\partial \beta}{\partial g_l}\right)_0 \cdot g_l = \beta_0 + \beta_l' \cdot g_l\,, \tag{2.9}$$

where β_l' is defined as the Raman tensor of the l-normal mode. Let us consider an harmonic oscillation of the normal mode coordinate, g_l, around the equilibrium position in the form

of $g_l = g_l^0 \cdot cos(\omega_l \cdot t)$ and an external electric field, $\vec{\epsilon} = \vec{\epsilon_0} \cdot cos(\omega_{exc} \cdot t)$ with an excitation frequency of ω_{exc}. Plugging the expression for g_l into Equation 2.9 and further combining the resulting term together with the electric field, $\vec{\epsilon}$, in Equation 2.7 returns the following equation:

$$\vec{u} = \left[\beta_0 + \beta_l' \cdot g_l^0 \cdot cos(\omega_l \cdot t)\right] \cdot \vec{\epsilon_0} \cdot cos(\omega_{exc} \cdot t)\,. \tag{2.10}$$

Equation 2.10 can be rewritten using trigonometric identities to the following form consisting of the sum of three individual terms [Van13]:

$$\vec{u} = \beta_0 \cdot \vec{\epsilon_0} \cdot cos(\omega_{exc} \cdot t) + \frac{1}{2} \cdot \beta_l' \cdot g_l^0 \cdot \vec{\epsilon_0} \cdot cos\left[(\omega_{exc} - \omega_l) \cdot t\right] + \frac{1}{2} \cdot \beta_l' \cdot g_l^0 \cdot \vec{\epsilon_0} \cdot cos\left[(\omega_{exc} + \omega_l) \cdot t\right]\,. \tag{2.11}$$

Equation 2.11 describes the molecular dipole moment that is induced due to the perturbations of an external electric field. The first term describes the elastic Rayleigh scattering at the same frequency as the monochromatic laser excitation, ω_{exc}. The second term is the (inelastic) Raman Stokes scattering at a frequency, ω_{Stokes}, smaller than the incoming laser excitation, i.e. $\omega_{Stokes} = (\omega_{exc} - \omega_l) < \omega_{exc}$. The second term is the (inelastic) Raman anti-Stokes scattering at a frequency, $\omega_{anti-Stokes}$, larger than the incoming laser excitation, i.e. $\omega_{anti-Stokes} = (\omega_{exc} + \omega_l) > \omega_{exc}$. If the Raman tensor, β_l', turns out to be zero, both Stokes and anti-Stokes scattering terms vanish and the vibrational mode is Raman inactive. In other words, a change in polarizability, i.e. $\beta_l' \neq 0$, is necessary for a Raman mode to be active. It is important to note that this classical description does not include all relevant aspects that are comprised in a full quantum mechanical treatment. For instance, in the case of $g_l^0 = 0$, no Raman scattering would be expected within the presented derivation, however, quantum mechanics introduces a zero-point energy and oscillations even in the vibrational ground state. Nevertheless, the classical description illustrates the essence of the scattering process and for further insights, the interested reader is referred to specialized literature [Le 09, Sie08].

Raman spectroscopy is element specific and provides a chemical fingerprint of the probed molecules, as the difference in energy between the incoming and scattered photons (see Figure 2.14), ΔR, is characteristic for a vibrational level of a molecule [Van13]. In this regard, also changes in the chemical environment of the molecule or its orientation can affect the chemical signature. As the molecule experiences a change in binding configuration with neighboring molecules, the electron density within the molecule is altered, which affects the bond strength, and, as a consequence, the associated Raman band shifts. Raman spectra are typically presented as the intensity of the inelastically scattered light as a function of the Raman shift, $\Delta\tilde{\nu}$, in wavenumbers (cm^{-1}). The Raman shift, $\Delta\tilde{\nu}$, is

defined from the energy difference, ΔR, as [Van13]:

$$\Delta\tilde{\nu} = \left(\frac{1}{\lambda_{exc}} - \frac{1}{\lambda_{sca}}\right), \tag{2.12}$$

where λ_{exc} is the wavelength of the incoming photon and λ_{sca} is the wavelength of the scattered photon. A peak in a Raman spectrum relates to a specific molecular vibration, and its peak position is specific to the molecule's chemical environment. In order to understand trends in Raman spectra, the analogy to a simple harmonic oscillator can be very useful. Let us consider a mass, m, that is connected via a spring with spring constant, κ, to e.g. the rigid room ceiling that can be considered as the infinite mass counterpart. This mass experiences a force, $m \cdot \frac{d^2x}{dt^2} = -\kappa x$. This differential equation can be solved by a sine function of the form $Z \cdot sin(\omega \cdot t + \xi)$, where Z is the amplitude and ξ is a phase factor, which results in the following term for the angular frequency, ω [Van13]:

$$\omega = \sqrt{\frac{\kappa}{m}}. \tag{2.13}$$

Accordingly, for higher masses, the Raman peaks are expected toward lower wavenumbers. For stronger bonds such as double or triple bonds, i.e. higher κ, the Raman peaks are expected at higher wavenumbers. The full width at half maximum (FWHM) of a peak can, for example, additionally be a measure for the degree of crystallinity, i.e. narrow peaks referring to more crystalline substances [Van13]. In general, Raman scattering cross-sections[6] are very low in the order of 10^{-29} to 10^{-32} cm^2 [Le 09, Pet05], which is several orders of magnitude lower compared to fluorescence (10^{-16} cm^2) [Osa01]. If during the scattering process the virtual state coincides with an electronic state, the Raman cross-section can be significantly higher. This specific case is referred to as resonance Raman scattering. However, in general, the drawback of Raman spectroscopy is the low Raman scattering cross-section that requires large amounts of analyte molecules for examination. The low Raman scattering cross-section represents a major challenge for the detection of molecules adsorbed onto surfaces with a limited number of adsorption sites. However, surface- and tip-enhanced Raman spectroscopy can eligantly circumvent this challenge by enhancing the otherwise weak Raman signals by localized surface plasmon interactions at metal surfaces, as explained in the following sections.

[6]The total Raman scattering cross-section, σ, is defined as the scattered intensity integrated over all scattering angles and polarization directions per incoming intensity of the incident light: $\sigma = \frac{I_{sca}^{int}}{I_{inc}}$ [Osa01].

2.5.2 Surface-enhanced Raman spectroscopy

In 1974, Fleischmann et al. discovered that, despite the inherently low Raman cross-section, pyridine molecules adsorbed onto rough Ag electrodes could, surprisingly, give sufficient Raman signal intensity to be detected [Fle74]. Later, Jeanmaire and Van Duyne confirmed that the enhanced Raman sensitivity does not originate from the increased number of surface-bound species due to the increase in surface area, but that the roughened surface geometry plays the pivotal role [Jea77]. At roughened nanostructured coinage metal (such as Cu, Ag, Au) surfaces, localized surface plasmons can strongly amplify the incident electromagnetic fields in close proximity to the metal surface and thus enhance the otherwise weak Raman signals of few molecules adsorbed to the metal surface. This enhancement in Raman sensitivity due to localized surface plasmons, as discussed in the following, is the basis for SERS. SERS is a powerful surface-sensitive label-free spectroscopic technique, which lies at the cross-roads of several disciplines, such as nanotechnology, surface chemistry, optics and plasmonics [Sch14].

A plasmon is a quasi-particle that describes the quantized collective electron oscillations of the free electron gas within a metal (that can be considered a 'plasma') [Sar10]. A surface plasmon is a certain type of longitudinal plasmon that is confined to the interface between two materials with dielectric functions of opposite sign [Le 09], for example a metal and a dielectric such as glass. The excitation of surface plasmons requires both energy and momentum conservation. However, the dispersion curves for the incident electromagnetic wave in free space ($\varepsilon = 1$) and the surface plasmon of atomically smooth surfaces do not intersect, as shown in Figure 2.15, and the necessary matching of momentum cannot be achieved for single crystal surfaces. For rough surfaces, however, at some designated spots, the surface corrugation can broaden the available momentum space and the incident light can couple to the 'localized' surface plasmons fullfilling momentum (and energy) conservation. These designated surface sites with specific surface geometry are called 'hotspots' and can also be viewed as nano-antennas enhancing the otherwise weak Raman signal. Within the laser focus spot of ca. 1 µm^2, only very few 'hotspots' are responsible for the Raman enhancement [Sha98, Fan08]. Around the 'hotspot', the created near-field is localized in lateral spatial dimensions of only a few nanometers and decays exponentially in vertical direction [Can11]. SERS is therefore a surface-sensitive technique.

Raman enhancement factors can be in the order of 10^7 to 10^{10} [Le 07] depending on the particular system under investigation and even single molecule detection has been demonstrated [Kne97]. Great efforts have been undertaken to determine the surface nanostruc-

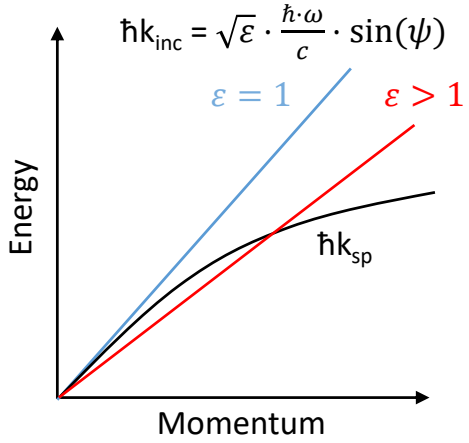

Figure 2.15. *Dispersion curve of a surface plasmon, $\hbar k_{sp}$ (black), and an electromagnetic wave traveling in different dielectric media (blue, red). $\hbar k_{inc}$ is the wave vector component parallel to the interface. ψ and ε denote the incident angle and the dielectric constant, respectively. The case for $\varepsilon > 1$ (red) is discussed in Subsection 2.5.4. Image adapted from Ref. [Dom06].*

tures that show optimal Raman enhancement as well as signal stability [Ban08]. This task is delicate, as the plasmon resonance frequency depends on the size and shape of the nanostructure, on the utilized material and on the dielectric function of the surrounding medium. For a single molecule, the electromagnetic field enhancement, G, in SERS can be considered as a two-step process [Kne06, Din16]. In the first step, the local electromagnetic field, $\vec{\epsilon}_{loc}$, is enhanced at the incident frequency, ω_{inc}, as the far-field is transferred to the near-field by the hotspot according to $G_{inc}(\omega_{inc}) = \frac{|\vec{\epsilon}_{loc}(\omega_{inc})|^2}{|\epsilon_{inc}|^2}$. In the second step, the local electromagnetic field, $\vec{\epsilon}_{loc}$, is enhanced at the Raman scattered frequency, ω_{sca}, again due to the coupling between the electromagnetic field and the localized surface plasmon resonance according to $G_{sca}(\omega_{sca}) = \frac{|\vec{\epsilon}_{loc}(\omega_{sca})|^2}{|\epsilon_{inc}|^2}$, and the near-field is transferred to the far-field. In a first approximation, $G_{inc}(\omega_{inc})$ roughly equals $G_{sca}(\omega_{sca})$, which leads to the following approximation:

$$G = G_{inc}(\omega_{inc}) \cdot G_{sca}(\omega_{sca}) \approx \frac{|\vec{\epsilon}_{loc}|^4}{|\epsilon_{inc}|^4} \,. \tag{2.14}$$

Accordingly, the electromagnetic enhancement, G, depends on the electric field to the power of four. In addition, the overall SERS enhancement is influenced by chemical enhancement effects that originate from intermediate charge-transfer states [Ott92, Van13]. For the purpose of this study, we stick to the simplified picture of electromagnetic enhancement by nano-antennas.

One nanostructure that provides particularly strong enhancement are two nanoparticles separated by a distance of a few nanometers that create a strongly enhanced electric field at the junction between them [Din16]. However, even rough Au surfaces can provide sufficient enhancement to detect few adsorbed molecules and provide valuable insight into the chemistry at polycrystalline surfaces (see Figure 2.16).

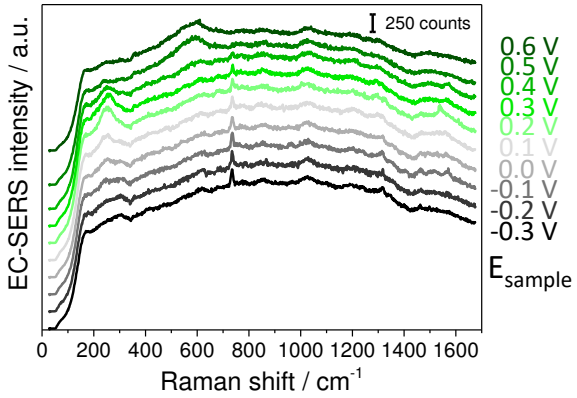

Figure 2.16. *SER spectra of a self-assembled monolayer of adenine on a rough polycrystalline Au substrate in 0.01 M H_2SO_4 under potential control (vs. Pt pseudo-RE). Pt wires were used for CE and RE, respectively. Each spectrum is an average of 6 to 8 individual spectra with an acquisition time of 5 s (laser power = ca. 1 mW determined in air). The abbreviation 'a.u.' denotes arbitrary units.*

Electrochemical SERS

SERS investigations are not limited to in air or under vacuum studies, but can be performed in aqueous electrolytes under potential control, referred to as EC-SERS. In fact, the early pioneering works of SERS were conducted under electrochemical conditions [Fle74, Jea77]. The SERS-active surface is the working electrode of a three-electrode setup as described earlier in Subsection 2.1.4. Figure 2.16 shows example EC-SER spectra of a SAM of adenine molecules adsorbed to an electrochemically roughened Au electrode portraying potential-dependent EC-SERS signatures of adenine [Dom07, Iba15, Wen16, Mar17b]. At 0.5 to 0.6 V vs. Pt, the Au surface is oxidized and the adenine molecules are irreversibly detached from the surface. EC-SERS provides the means to study electrochemical processes at the electrified solid-liquid interface, such as molecular reorientation [Yao08], molecular adsorption [Leu87] or electrocatalytic reactions [Wu08, Wil19], as a function of applied potential and/or electrolyte composition. Despite the irrevocable strengths of (EC-)SERS, one major disadvantage of (EC-)SERS is its limitation to rough polycrystalline surfaces of coinage metals. This challenge can be overcome, for example, by electrochemical shell-isolated nanoparticle-enhanced Raman spectroscopy (EC-

SHINERS), for which Au nanoparticles are fully coated by a 2 to 5 nm thin Si layer and then dispersed on single crystal surfaces or other surfaces of interest [Li10]. It has been shown that the electrochemical response of such SHIN-covered ('smart dust') single crystal surfaces remains uneffected, i.e. the original surface properties are maintained, while the SHIN-particles provide effective Raman enhancement to detect adsorbates or even reaction intermediates during electrochemical reactions [Don19]. EC-SHINERS, as a specific EC-SERS methodology, is undeniably an extremely powerful technique to gain mechanistic insight into reaction mechanisms on well-defined surfaces. However, as highlighted earlier in the introduction, nanometer, if not atomic, chemical-spatial resolution is needed to directly study the behavior of single defect/active sites. After shortly specifying the EC-SERS setup utilized in this work, we introduce an experimental technique - EC-TERS - that allows both the investigation of single crystal surfaces (in principle not restricted to coinage metal surfaces) as well as the necessary chemical-spatial resolution in the nanometer regime.

EC-SERS setup

The EC-SERS setup is a home-built one that uses a long working-distance Olympus 50x objective (NA = 0.5, working distance = 10.6 mm), a red HeNe laser (632.8 nm, linearly polarized, max. output power = 35 mW) and a Horiba iHR 550 spectrograph with a nitrogen-cooled CCD detector (Symphony II, Horiba). The spectrograph and CCD detector are controlled via LabSpec 5 software. The home-built Teflon cell is positioned in a backscattering configuration on an x-,y-stage and the objective can be moved in z-direction, allowing fine-tuning of the laser focus. An additional CMOS camera (Mikrotron, MC 1362) temporarily coupled into the beam path with a beam splitter aids proper laser focusing onto the Au surface. Around 20 mW of laser power is typically measured in air at the laser focus as maximum available power. In the liquid cell, the power in the laser focus is estimated to be around 5 to 7 mW. Intensity losses are due to optical aberrations at the glass window (1-2 mm thickness). The home-built Teflon cell accommodates the WE, which can be approached ca. 1 mm to the glass window, and a Au (0.5 mm diameter, Alfa Aesar, Premion, 99.9985% metals basis) and hydrogen-loaded Pd wire (0.5 mm diameter, MaTecK, 99.95% metals basis) as CE and RE, respectively. CorrWare software controls the Schlumberger potentiostat (SI 1286 Electrochemical Interface).

2.5.3 Tip-enhanced Raman spectroscopy

In 1985, just around the time when scanning tunneling and atomic force microscopies were invented [Bin82b, Bin82a, Bin86], John Wessel envisioned an apparatus that would

allow optical microscopy well-below the Abbe-diffraction limit and the detection of single molecules [Wes85]. He suggested to scan a Ag particle with nanometer size as optical probe across a surface while focusing a laser beam onto the nanoparticle. The excitation of surface plasmons would strongly amplify the spatially confined electromagnetic field in the proximity of the Ag particle and thus enhance the Raman signal of the molecules within the probe-sample gap. The spectroscopic Raman fingerprints of the adsorbate molecules' vibrational states would reveal chemical structure and bonds rendering a spatial resolution down to the nanometer regime. The scanning of the optical probe would be accomplished by piezoelectric elements in a similar fashion as the newly developed SPMs. He further envisioned the great importance of overcoming the technical challenges including precise control of the probe-sample distance and the necessity of producing well-defined metal tips with an exact shape for promoting strongest near-field enhancement, as well as the complex experimental implementation.

15 years later, his vision was turned into reality and TERS was born [Ino99, Stö00, And00, Hay00, Pet00]. The setups essentially follow Wessel's approach to combine SPM with Raman spectroscopy. The basic working principle is illustrated in Figure 2.17. The SPM-tip, which is either metallic or metal-coated, acts as an antenna to locally enhance the electromagnetic near-field by excited localized surface plasmons (see previous SERS section 2.5.2 for details on plasmons). The tip can be viewed as a single hotspot, in analogy to SERS [Din16], that is scanned across a surface. TERS allows to investigate rough as well as smooth surfaces from metals to semiconductors to isolators [Sch13]. Therefore, TERS overcomes the dependency of SERS on nanostructured coinage metal surface hotspots, renders high surface sensitivity and achieves meV spectral and nm spatial resolution so that topographic and chemical information on the nanoscale can be simultaneously extracted. TERS, as a specific type of plasmon-enhanced Raman spectroscopy, is thus a versatile experimental technique that is widely applicable in physical chemistry, biology, materials and surface science [Dom10, Sha15, Kur16]. Figure 2.17B shows example TER spectra of a SAM of thiophenol on Au(111) recorded under ambient conditions, for the tip-approached (near-field) and tip-retracted (far-field) case. Only when the tip is approached to the sample surface, the thiophenol chemical fingerprint that can be assigned to different vibrational modes of thiophenol is observed [Mar16, Mar17a].

Vertical and lateral resolution

Experimentally, it was found that the tip-sample distance can have a profound influence on the TERS signal intensity. Specifically, a reduction in the tip-sample distance results

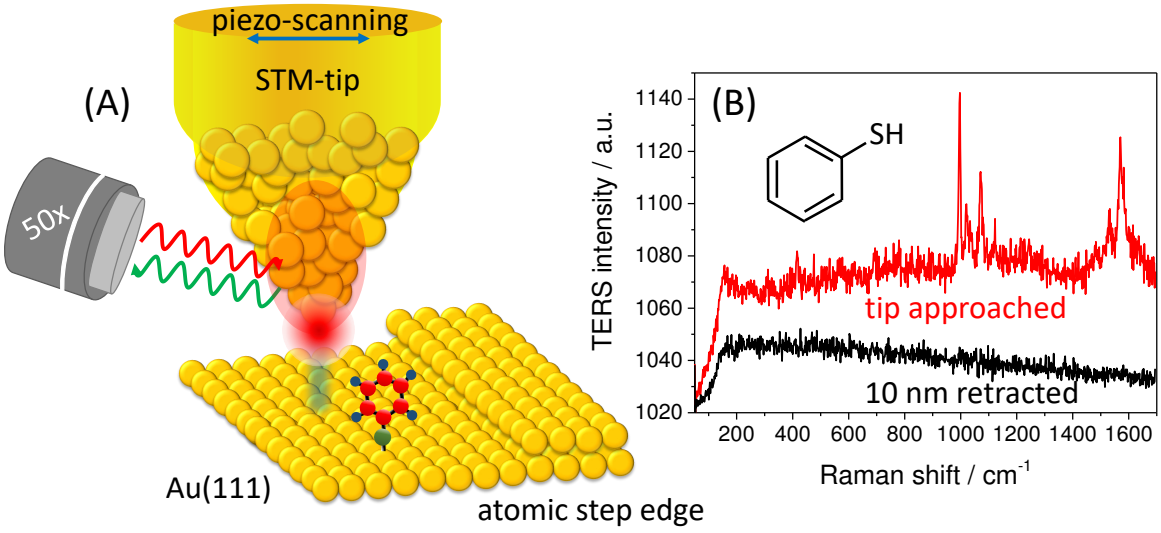

Figure 2.17. *(A) Illustration of tip-enhanced Raman spectroscopy (TERS). A laser is focused onto an SPM tip that acts as a local nano-antenna amplifying the otherwise weak Raman signals from molecules located in close proximity to the SPM-tip. The SPM allows acquisition of surface topography images that can be combined with simultaneously acquired chemical Raman maps. (B) Example TER spectra of a SAM of thiophenol attached to Au(111) recorded in air. When the STM-tip is approached in tunneling conditions to the surface (<1 nm), TER spectra are obtained (red curve). When the STM-tip is retracted 10 nm away from the surface, only the far-field background signal is observed (black curve). Inset: Thiophenol molecular structure.*

in an increase in TERS enhancement [Pet05, Pet07, Can09, Mar17a]. Under inert Ar atmosphere, the tip-sample distance effect on the signal intensity appears to be more pronounced than in water experiments [Mar17a]. In general, the height/z-resolution of TERS depends on the vertical ('z-axis' or surface normal of the planar sample surface) extension of the near-field that was found to be inversely proportional to the 10^{th} power of the tip-sample distance for 2D surfaces [Pet05]. In short, this reciprocal power of ten originates from the near-field distance dependence of an oscillating dipole, $(\varsigma_{tip} + d)^{-3}$ [Ker82], which together with the 4^{th} power law of Equation 2.14 and the integration over the probed 2D surface area results in the power of ten [Pet05, Dom06]. ς_{tip} is the radius of the tip apex and d is the tip-sample distance.

The lateral resolution in the field of optical microscopy is the distance between two objects that still allows the optical imaging and distinction of both individual objects. The lateral resolution of typical optical microscopes is limited by the Abbe diffraction limit that defines the maximum lateral optical resolution accessible by far-field optics and amounts to roughly $\sim \frac{\lambda}{2}$ [Sta12]. For visible light, $\frac{\lambda}{2}$ is in the range of ~190-370 nm. Near-field Raman

spectroscopy, i.e. TERS, allows to overcome the diffraction limit by field confinement at the nano-antenna STM tip apex. The near-field spatial confinement is responsible for the extremely high spatial resolution of a few nanometers or better [RL17].

A Heaviside (step) function would suggest that the lateral spatial resolution of TERS should coincide with the dimension of the tip radius, ς_{tip} [Pet05]. A more realistic estimation was derived by Pettinger et al. approximating the lateral resolution to be $\frac{\varsigma_{tip}}{2}$ [Pet05], which was often utilized as a conservative estimate of the achievable lateral TERS resolution in the past. Accordingly, a standard TERS-tip radius of 20 nm (see Figure 2.19) would result in a spatial resolution of 10 nm. In fact, to date such lateral resolution has been achieved in numerous studies under ambient conditions [Ste08]. However, even the few nanometer regime of <5 nm has been demonstrated [Che14a, Zho17] with a spatial resolution independent of the coarse tip dimensions. Even more impressively, even sub-nanometer spatial resolution has been shown for specific cases under UHV conditions [Zha13a, Lee19], allowing to visualize the distribution of specific vibrational modes or orbitals within a single molecule [Lee19]. While a theoretical concept to describe such impressive results is still under development [Men15, Che19], the prospects of sub-nm chemical spatial resolution are tremendous for all interface-related disciplines. In general, highest TERS enhancement and lateral spatial resolution can be achieved in the gap-mode [Hay01]. An image dipole is created in the metal surface of the substrate from the laser excitation-induced dipole at the tip apex. These two localized surface plasmons are interdependent and form the gap-mode, which leads to additional enhancement and field confinement proportional to $\sqrt{\varsigma_{tip} \cdot d}$ [Shi17]. This is the reason why many (EC-)TERS studies are performed on metal substrates, often of the same material type as the tip.

Electrochemical TERS

The TERS technique can be conducted in air or under inert gas atmosphere as well as in liquids under potential control, i.e. under electrochemical conditions. Figure 2.18 illustrates the EC-TERS setup that requires a bipotentiostat to control the potentials of both the sample surface and the STM-tip. The first AFM-based TERS measurement in liquid environment without potential control was achieved by the Zenobi group in 2009 [Sch09], followed by Nataka et al. who studied time-dependent liquid TERS of lipid bilayers in water [Nak13]. In 2015, the Ren and Van Duyne groups independently published the first results on STM- and AFM-based EC-TERS that were shortly afterwards followed by the Domke group [Zen15, Kur15, Mar17b]. These first pioneering works have demonstrated the huge potential of EC-TERS for electrochemical surface science, observing potential-

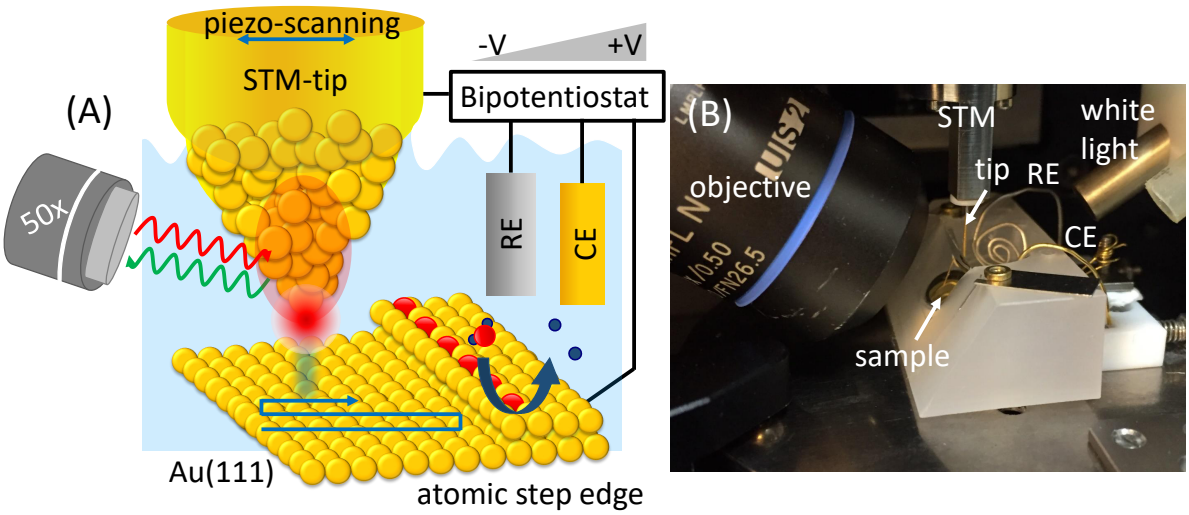

Figure 2.18. *(A) For EC-TERS, the measurements are conducted in aqueous electrolytes and both sample electrode and SPM-tip are potential-controlled by a bipotentiostat. EC-TERS is thus the combination of SPM, near-field Raman spectroscopy and electrochemistry. CE and RE denote counter and reference electrode, respectively. (B) Image of the EC-TERS sample cell utilized within this work showing the objective, STM-tip, sample in home-built Kel-F® cell with electrolyte and CE and RE.*

dependent redox reactions, protonation/deprotonation and reorientation of SAMs (see Chapter 1 for detailed review). In this thesis, we show that EC-TERS can be utilized to perform operando EC-TERS mapping while AuOx surface species are formed operando, providing unprecedented nanochemical insight into surface reactivity under reaction conditions.

EC-TERS setup

The utilized EC-TERS setup is an STM-based home-built device and has been described in full detail previously [Mar16, Mar18, Dri18]. Here, the most important setup features, technical details and procedures are shortly summarized, while further technical design considerations can be found in the literature and are not readdressed here. The EC-TERS setup incorporates an EC-STM from Keysight Technologies GmbH (STM 5420, former Agilent), which is equipped with a bipotentiostat and a tip-scanner with an elongated tip-holder (see Section 2.4 for further EC-STM specifications). The red HeNe laser (632.8 nm, linearly p-polarized, max. output power = 35 mW, Research Electro Optics Inc., model 32413) is focused on the EC-STM Au-tip in a side-illumination configuration at a 55° angle with respect to the surface normal. The red laser light is first passed through a

clean-up filter (Semrock MAXLINE LL-632.8-25.0M) and, if required, through two additional gray filters to reduce the laser intensity. The 50x long working-distance objective has a working distance of 10.6 mm (Olympus, NA = 0.5). The liquid nitrogen-cooled CCD detector (Symphony II, Horiba) and the Horiba iHR 550 spectrograph are controlled by LabSpec 5 software. The spectrograph provides three different gratings of 600, 1200 and 1800 lines/mm. A dichroic laser beam splitter (Semrock RazorEdge Dichroic LPD02-633RU-25) separates the excitation and detection pathways, providing for the latter a frequency cut-off value of 156 cm^{-1}. The detection path is further equipped with a Rayleigh-filter (Semrock RazorEdge ultrasteep long-pass edge filter LP02- 633RE-25) with a cut-off at 79 cm^{-1}. Raman spectra from 156 to 4000 cm^{-1} can be obtained in a multi-window collection mode. The home-built Kel-F® cell provides a laser entrance through a glass window (high precision cover glass, cut from 24 mm x 50 mm glass slides, thickness 170 ± 5 µm) that is pasted with UV glue (Loctite 3321) on the Kel-F® cell (see Figure 2.18B) at a 55° angle with respect to the sample surface normal to match the angle of the 50x objective. An O-ring (Kalrez, FFKM 75, DTH-Dichtungstechnik GmbH, outer diameter 8 mm x 0.7 mm) seals the Au(111) single crystal to the Kel-F® cell compartment. The Kel-F® cell accommodates the aqueous electrolyte, WE, CE and RE.

Au-tips are electrochemically etched in 1:1 solution of HCl (37% fuming, Merck, Emsure) and Ethanol (Merck, Emsure) at 2.4 V with a circular-shaped Au CE (1.0 mm diameter, Mateck, 99.995%) made of Au wire (0.25 mm diameter, Alfa Aesar, Premion, 99.9985%) following the procedure by Ren et al. [Ren04]. During the electrochemical etching procedure, Au oxides are formed that are subsequently dissolved by the Cl^- anions in solution forming $AuCl_4^-$ [Pod79]. Figure 2.19 shows a scanning electron microscope (SEM) image of typical TERS Au-tips prepared by electrochemical etching. The Au-tips are electronically isolated by Zapon wax (CLOU ZAPONLACK Schutzlackierung) coating. The coating procedure consists of about six successive rounds of pulling the etched-Au-tip through a thin layer of Zapon wax and subsequent drying (ca. 10 min per Au-tip) [Mar18]. For the EC-TERS experiments, the EC-TERS tip is positioned at a distance of 1 to 2 mm to the upper edge of the pasted glass window. The EC-STM is located on an x-,y-stage that allows positioning of the TERS-tip with respect to the incoming laser beam. The Olympus 50x objective is mounted on a piezo stage (Steinmeyer Mechatronik GmbH, 3 nm step precision) to focus in z-direction. A CMOS camera (Mikrotron, MC 1362) can be temporarily coupled into the laser beam path by means of a beam splitter to create a white light (white light source: SCHOTT KL 1600) image that aids precise

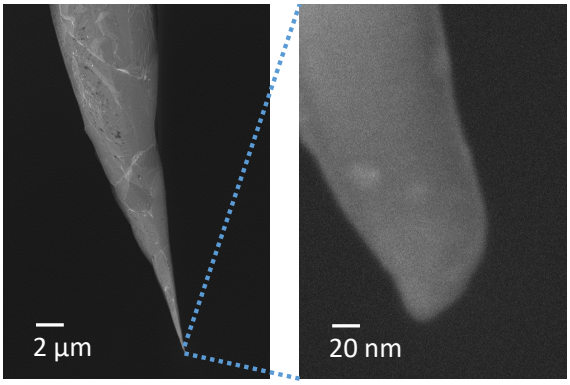

Figure 2.19. *Scanning electron microscope (SEM) image of typical TERS Au-tip prepared by electrochemical etching.*

laser focusing (Figure 2.20). A laser power of about 20 mW is usually measured in air

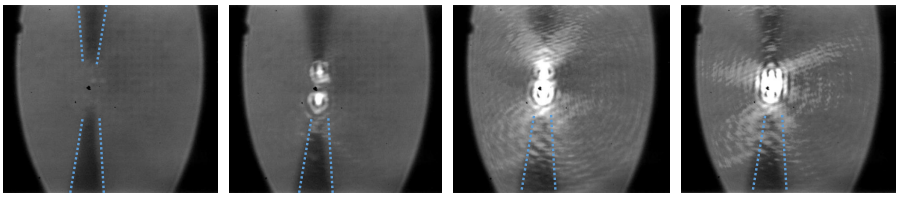

Figure 2.20. *White light images recorded during EC-TERS tip approaching to the Au(111) sample surface in 0.1 M aqueous sulfuric acid electrolyte.*

at the laser focus as maximum available power. Due to optical aberrations at the glass window, the actual power is estimated to be lowered by a factor of 3 to 5 when working in liquid [Mar16].

The employed EC-TERS setup allows the investigation of opaque single crystal electrodes in contact with bulk electrolyte solutions. The use of bulk electrolytes in comparison to liquid drops minimizes electrolyte evaporation, which can change the solution pH, requiring continuous replenishment of electrolyte otherwise. The relative tip-sample distance can be controlled by the sample bias and current setpoint. In addition, EC-STM based TERS typically provides higher enhancement factors compared to AFM [Pet12].

Experimental challenges

EC-TERS poses a number of technical and experimental challenges that are mentioned here. For additional details, the interested reader is referred to the literature about the EC-TERS setup design and its development [Mar18, Dri18]. As EC-TERS is the combination of different methods, namely SPM, Raman spectroscopy and electrochemistry, the technique is complex by its very nature [Wan17]. The electrolyte liquid and glass window that allow the laser light to enter the electrochemical cell lead to light aberrations that make laser focusing on the tip more challenging and less efficient than in air. The laser beam should only travel smallest possible distances in the liquid to minimize total focus aberrations [Mar18]. The long working distance air objective needs to be aligned with the EC-STM tip. As such, the objective reaches close to the EC-TERS cell, which introduces stringent space constraints that require precise setup engineering and particular care while operating the EC-TERS setup. In addition, much longer Au EC-STM tips (ca. 1.5 cm) are required compared to regular EC-STM experiments (ca. 0.5 cm), in which usually also more stiff tip materials such as Pt/Ir or W are used. Both material (Au) and length of the EC-TERS tips result in lower STM stability. Moreover, for electrochemical TERS, the tips need to be electronically isolated to minimize parasitic leakage currents. For EC-TERS mapping and simultaneous EC-STM imaging, an EC-TERS tip with good electronic isolation (below 50 pA), good STM imaging capabilites (low drift, high stability) and good TERS enhancement (high signal-to-noise ratio) are required. These requirements need to be fullfilled while performing electrochemical measurements and require clean electrolyte and sample preparation, a stable RE as well as precise potential control. Each step adds to the experimental complexity of an EC-TERS experiment. Finally, it is important to note that, in the case of in-situ formed surface analyte species (as will be seen later), laser fine focusing according to the EC-TERS signal is additionally complicated by the fact that EC-TERS signals can only be obtained when the surface analyte species has been generated.

2.5.4 Surface-enhanced IR absorption spectroscopy

In 1980, Hartstein et al. discovered that molecules adsorbed at metal thin films exhibit an increase in IR absorption compared to conventional measurements without the presence of a metal surface [Har80]. This surface-enhanced infrared absorption (SEIRA) effect in the visible to mid-infrared region is similar to the SERS effect and can provide IR absorption enhancements in the order of 10^1 to 10^3 [Osa91]. As in SERS, the metal surface morphology plays a crucial role for the obtainable enhancement. In general, chemisorbed molecules

tend to exhibit stronger enhancement than merely physisorbed molecules [Osa01]. Two enhancement mechanisms have been suggested to contribute to the SEIRA effect, namely an electromagnetic and a chemical enhancement mechanism. The electromagnetic enhancement originates from the excitation of localized surface plasmons within the metal thin film by the incident light and the localized electromagnetic near-field that is thereby generated [Wok84]. For continuous metal films, surface plasmons are excited by electromagnetic radiation of 200 to 800 nm wavelength. However, the metal films portraying the SEIRA effect are not continuous but composed of small metal islands of 20 to 80 nm size, on which surface plasmons can be excited in the IR range [Zhu18, Neu13]. In addition, according to the Bruggemann model [Bru35], the dipole interactions between different metal islands are also of relevance. It has been suggested that the optical properties of the metal thin films (usually portraying a large imaginary part of the dielectric function and thus leading to strong damping of the localized surface plasmons) are perturbed and adjusted by additional induced dipoles introduced by the adsorbates, which provides further explanation of the experimentally observed enhancement [Osa01]. In contrast, the chemical enhancement stems from molecule-metal surface interactions, where molecular orbitals and metal surface charge oscillations are expected to couple with each other and enlarge the absorption coefficient [Per81]. The absorption, $\mathcal{A}$, can be written as follows [Osa01]:

$$\mathcal{A} \propto |\frac{\partial \vec{u}}{\partial g}|^2 \cdot |\vec{\epsilon}|^2 \cdot cos(\Theta)\,, \tag{2.15}$$

where $\vec{u}$ is the dipole moment, g is the normal coordinate, $\vec{\epsilon}$ is the electric field and Θ describes the angle between the derivative of the dipole moment and the electric field vector. While the chemical enhancement changes the first term containing the dipole moment derivative, $|\frac{\partial \vec{u}}{\partial g}|^2$, the electromagnetic enhancement locally increases the electric field, $\vec{\epsilon}$ (Equation 2.15). Depending on the molecular orientation, the angle, Θ, is modified, which also influences the extent of absorption, $\mathcal{A}$.

The field-enhancement requires the effective coupling between the incoming light and the local surface plasmon via energy and momentum conservation (see Figure 2.15). While for SERS rough coinage metal surfaces or nanostructures allowed the corresponding dispersion curves to intersect, here IR transparent prisms, such as Si, CaF_2, Ge, ZnSe, with sufficiently high dielectric functions ($\varepsilon > 1$), schematically shown in Figure 2.21, can be utilized to ensure the necessary matching of momentum. The Otto configuration is employed for infrared reflection absorption spectroscopy (IRRAS), where the working electrode is brought as close as 1 to 10 µm to a CaF_2 prism and the IR light has to travel through the small electrolyte gap and is absorbed and reflected at the WE. This allows

the usage of well-defined single crystals, but the hindered mass transport in the narrow electrolyte gap makes static[7] measurement conditions more practial. In the Kretschmann configuration, a thin metal film (ca. 20 nm) is evaporated onto a Si prism and the IR light is internally total-reflected at the prism-metal interface. The evanescent wave only extends a few hundreds of nanometer into the electrolyte [Osa01], which is why the contribution from the bulk electrolyte is lower compared to IRRAS. In addition, the SEIRAS effect amplifies the vibrational signals and the Kretschmann configuration is utilized for attenuated total reflection surface-enhanced IR spectroscopy (ATR-SEIRAS) measurements with high surface sensitivity. For example, even water molecules at the interface were investigated [Ata98] and time-resolved monitoring of electrochemical processes has been demonstrated with fast response times from 0.1 to 10 s [Nod99].

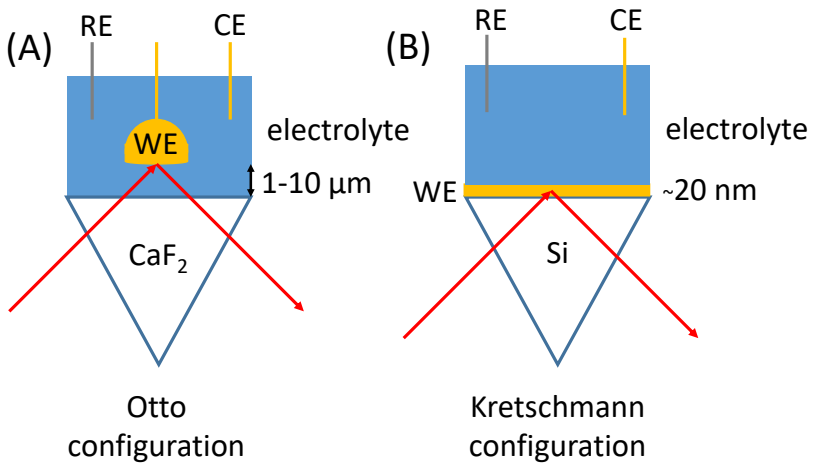

Figure 2.21. *Comparison of Otto and Kretschmann configurations, as discussed in the text. (A) The Otto configuration is employed for IRRAS. (B) The Kretschmann configuration is utilized for ATR-SEIRAS.*

EC-SEIRAS setup (Alicante)

The EC-SEIRAS setup consists of a Nicolet 8700 Thermo Scientific spectrometer that is equipped with a MCT-A detector (HgCdTe based) that is liquid-N_2-cooled, and a wire grid ZnSe polarizer (PIKE Technologies). The spectrometer is controlled by OMNIC software. The EC-SEIRAS experiments of this thesis were performed in an ATR configuration. The EC-SEIRAS sample, thermally evaporated Au deposited on a Si 60° prism (Pastec Ltd, Japan), and the spectro-electrochemical cell are mounted on top of a Veemax reflectance accessory (PIKE Technologies). Potential control is assured by the potentiostat Model

[7] i.e. at equilibrium conditions without any surface reactions occuring that require mass diffusion in the narrow electrolyte gap.

175 Universal Programmer (Princeton Applied Research) equipped with an eDAQ e-corder and Chart software. RE and CE (specified in Section 4.2) as well as Argon inlets for electrolyte degasing and blanketing are incorporated in the spectro-electrochemical cell. The EC-SEIRA spectra are typically plotted in absorbance units, $\mathcal{A}$, defined as:

$$\mathcal{A} = -log\left(\frac{I}{I_{ref}}\right) . \tag{2.16}$$

Here, I is the reflected light intensity at the sample surface at the applied sample potential and I_{ref} is accordingly the light intensity recorded at the reference potential. If reference spectra are obtained at potential regions where no (specific) ion adsorption occurs, positive and negative EC-SEIRA bands at the desired sample potential (with respect to the reference potential) correspond to the gain or loss of species.

Chapter 3

Monitoring the AuOx electro-reduction

This chapter is about to be submitted for publication as and is reproduced/adapted from 'Jonas H. K. Pfisterer, Francesco Nattino, Ulmas E. Zhumaev, Manuel Breiner, Juan M. Feliu, Nicola Marzari and Katrin F. Domke, "Observation of reaction intermediates during the gold oxide reduction reaction by EC-SERS and implicit solvent DFT", 2019' [Pfi19b]. Please contact the authors for further information. The DFT calculations underlying this chapter were performed by Francesco Nattino (EPFL, Marzari group).

Detailed molecular understanding of surface chemistry under reaction conditions is pivotal for improving electrocatalytic devices, electrochemical synthesis routes or suppressing corrosion phenomena. Operando monitoring and reliable identification of reacting species are therefore of utmost importance and require highly surface-molecular sensitive experiments under reaction conditions. Here, we employ EC-SERS to monitor short-lived reaction intermediates during the electro-reduction of AuOx in sulfuric acid. Performing potential-jumps to trigger the AuOx reduction and then monitor the evolution of reaction intermediates as a function of time over the course of several tens of seconds. We observe a peak splitting of the broad AuOx spectral feature around 594 cm^{-1} into two bands. According to DFT, they can be attributed to Au-OH and Au in a 4-fold coordination with oxygen resembling the bulk Au_2O_3 coordination. The EC-SER spectra provide evidence for temporary proton adsorption and subsequent OH-release, as well as for the adsorption of (bi)sulfate ions during the surface reduction process. The presented potential-jump experiments combined with implicit solvent DFT simulations confirm that short-lived Au-OH intermediates are formed also in acidic media during the AuOx electro-reduction, implying their relevance during surface oxidation and, potentially, for the OER.

Moreover, the following chapter highlights that EC-SERS on electrochemically roughened polycrystalline Au surfaces offers sufficient SERS enhancement to detect AuOx reaction products/intermediates under reaction conditions and provides important knowledge about the reaction system to proceed with the EC-TERS nanoscopy measurements presented in Chapter 5.

3.1 Introduction

The rational design of efficient electrochemical devices, improved electrochemical synthesis protocols or effective measures against metal corrosion all require detailed molecular understanding of the underlying reaction mechanisms and thus of the surface chemistry [She17, Pom04, Mez16]. Elucidating reaction pathways by operando monitoring and identification of reaction intermediates can provide the necessary insight to strategically modify the electrode surface structure and/or material composition to engineer surface reactivity, selectivity and stability [Ban14]. However, time-resolved detection with high sensitivity and reliable identification of surface reaction intermediates under realistic working conditions is demanding [Mei18] and require sophisticated experimental tools, because of the typically low residence times (µs to s [Ben16, Sri98, Bri00]) of the molecular adsorbates at the surface, a limited number of available active surface sites [Rei12] and thus often the presence of only small amounts of species as well as technical experimental challenges due to the aqueous electrolytes including potential control. For example, the detection of reacting OH species during oxygen reduction or noble metal corrosion reactions constitutes a huge challenge to clarify suggested reaction mechanisms [Don19, Zhu13]. Highly sensitive spectro-electrochemical tools that provide surface-molecular specificity under realistic working conditions are therefore required.

To date, Au has remained attractive as an electrocatalyst for fuel cells, electrolysis and battery applications to tune device efficiency [Rod14], for example as part of bimetallic compounds [SH10]. Besides, Au can be considered as one of the most widely spread electrochemical model systems of fundamental interest, for example, as catalytic electrode, catalyst support or model corrosive material. During water splitting, pristine Au is transformed to AuOx. However, despite long-standing research efforts, the exact nature of the electrochemically generated AuOx, its formation mechanism(s) as well as its electroreduction pathways are still not fully understood. The latter is of particular importance, as the electro-reduction of AuOx mimics the surface reduction-event during anodic oxida-

tion of small organic molecules or during water splitting at anodic potentials providing at least partly the required oxygen elements from the AuOx surface [Con95]. Based on an unusually broad and asymmetric vibrational band around 580 cm^{-1}, Weaver and co-workers already hypothesized that the AuOx surface – 'starting point' for the electro-reduction as well as the water splitting – is composed of a multitude of oxide/hydroxide structures, possibly involving a variety of different coordination geometries as well as hydration states [Des86]. However, experimental evidence has remained scarce. In neutral/alkaline media, EC-SHINERS revealed an OH-bending mode at 807 and 790 cm^{-1}, respectively, indicating the involvement of OH species in Au oxidation/reduction [Zhu13, Li15]. In acidic media, it is typically assumed that AuOx reduction as well as Au oxidation also proceed via the formation of Au-OH intermediates [AK86]. However, Au-OH species have, to the best of our knowledge, not been observed spectroscopically during AuOx reduction/Au oxidation in acidic solutions, despite the possible formation of Au-OH as key intermediate during oxide film formation [Štr88, Con95], corrosive Au dissolution [Che13], the OER [DM13] or ORR [Don19].

Experimentally, EC-SEIRAS has provided, for example, molecular insight into potential-dependent ion adsorption on Au electrodes [Osa97, Ata98], but is limited to higher wavenumber regions (>1000 cm^{-1}). The low wavenumber regions (0 to 1000 cm^{-1}), however, typically carry relevant information on molecule-metal surface interactions. Raman spectroscopy covers also lower wavenumber regions and is less hindered by absorption of water in comparison to IR light. The typically low Raman scattering cross-sections can be elegantly bypassed by EC-SERS[Fle74, Jea77], where nanoscale rough metal surfaces enhance the otherwise weak Raman signals and provide the required high surface-molecular sensitivity [Din16]. In terms of theory, recent progress in DFT simulations considering implicit solvent models allow advanced calculations of molecular vibrations at solid-liquid interfaces, potential-dependent stability investigations and a reliable interpretation of experimentally gathered spectroscopic data [Hör19].

Here, we employ potential-jump EC-SERS experiments to in-situ monitor short-lived reaction intermediates during the electro-reduction of AuOx. We jump to the onset potential of the AuOx reduction to follow the evolution of reaction intermediates as a function of time, as opposed to following an averaged EC-SERS response during CV over either a wide potential range or long acquisition/stabilization times as typically done in complementary EC-SERS experiments [Zhu13, Zha93, Bel05, Kim06, Yeo11]. The jump approach allows to track dynamically-evolving reaction intermediates in acidic media, such as OH, AuOx

and (bi)sulfate species over several tens of seconds under reaction conditions. We observe a peak splitting of the broad AuOx spectral feature ∼594 cm^{-1} into two bands. According to DFT, these bands can be attributed to Au-OH and Au in a 4-fold coordination with oxygen resembling the bulk Au_2O_3 coordination. Further, the EC-SER spectra provide evidence for temporary proton adsorption and subsequent OH-release to form water, and for the adsorption of (bi)sulfate ions during the surface reduction process. The presented potential-jump experiments show that short-lived Au-OH intermediates are formed during the AuOx electro-reduction also in acidic media, suggesting that such species play a role in the OER mechanism during concomitant surface reduction.

3.2 Materials and experimental details

The polycrystalline Au electrode (EDAQ ET053-1 Au disc electrode, 3 mm Au disc in 6 mm OD PEEK body) was electrochemically roughened following the procedure by Tian and co-workers [Tia02]. The roughening was performed in 0.1 M KCl (99.999%, Suprapur, Merck) solution with a Au wire as CE (0.5 mm diameter, Alfa Aesar, Premion, 99.9985% metals basis) and a commercial Ag/AgCl RE (3 M KCl, SI Analytics). The Au electrode was kept at -0.3 V vs. Ag/AgCl for 30 s, then ramped to 1.2 V vs. Ag/AgCl with a scan rate of 1 V/s and held at this potential for 1.2 s. Afterwards, the potential was ramped back to -0.3 V vs. Ag/AgCl with an adjusted scan rate of 0.5 V/s and again held at -0.3 V vs. Ag/AgCl for 30 s. This procedure/cycle was repeated 25 times leading to a brownish/red color of the Au electrode. Subsequently, the Au electrode was thoroughly rinsed with MilliQ water (Millipore-Q, 18 MΩ cm, Merck) as well as stored in MilliQ water and shortly before cell mounting in 0.1 M H_2SO_4 to remove any possible contaminants adsorbed during the roughening procedure.

The home-built EC-SERS setup is described in Subsection 2.5.2. A backscattering configuration and a 600 lines/mm grating was employed for the reported experiments. The laser power of ca. 20 mW at the laser focus spot was measured in air and is comparable to other EC-SERS studies [Des86]. Acquisition times between 0.5 and 1 s were used. The Pd-H RE was prepared by applying between 5 to 10 V between the Pd wire and a Au CE in 0.1 M H_2SO_4 until the evolution of hydrogen gas roughly corresponded to the oxygen gas bubble formation. The Pd-H RE was freshly prepared before each experiment and, for a pH of 1 (as used in this study), corresponds to RHE at pH of 0 (i.e. SHE). The aqueous electrolytes were 0.1 M H_2SO_4 (96%, Suprapur, Merck) prepared from either MilliQ water or deuterated water (Deuterium oxide, 99.9 atom % D, Sigma-Aldrich). For the

reliable comparison of H_2O and D_2O data sets, the EC-SERS measurements were always performed subsequently on the same day in H_2O- and D_2O-based H_2SO_4 electrolytes with the same sample electrode. The electrolytes were degased with Ar (Westfalen, 6.0 N) before transfer to the Teflon cell. The Teflon cell and all glassware were boiled in ∼40% HNO_3 (≥65%, Sigma-Aldrich). The glass cell window (1-2 mm x 25.4 mm, PLANO GmbH) and Kalrez-F sealing ring (6 mm x 2 mm, VOXTEC) were cleaned separately in Piranha solution (H_2SO_4 (96%)/H_2O_2 (30%) ratio of 3:1). After the chemical cleaning, all items were boiled in MilliQ water three times with thorough MilliQ rinsing between each boiling step.

Additional CV measurements were performed with a Metrohm Autolab PGSTAT 30 multipotentiostat using NOVA 2.1.2 software. The working electrode was a polycrystalline Au electrode as used for the EC-SERS experiments, but without the additional roughening procedure. A Au wire and a Pd-H wire were used as CE and RE, respectively. The Pd-H RE was prepared according to the same procedure specified above. Ar gas was used to degas the 0.1 M H_2SO_4 electrolyte (Milli-Q based) for 30 min and to then blanket the solution. To electrochemically clean the working electrode, 5 CV scans up to Au oxidation at 1.6 V vs. Pd-H were performed before each measurement (100 mV/s scan rate). The additional electrochemical measurements were conducted by Manuel Breiner (MPIP, Domke group).

3.3 Experimental results

Figure 3.1A shows the CV of the roughened polycrystalline Au electrode recorded in the EC-SERS cell at a scan rate of 50 mV/s in 0.1 M H_2SO_4. The oxidation of the polycrystalline Au electrode starts at ∼1.3 V vs. Pd-H and the subsequent reduction of surface AuOx commences at ∼1.2 V vs. Pd-H. The obtained CV is in accordance with the literature [Che13, DM13, Yeo10] and corresponds well with additional electrochemical measurements on polycrystalline Au without the roughening procedure necessary to provide SERS enhancement. Figure 3.2A compares the CVs of the roughened (to obtain EC-SERS enhancement) and not roughened polycrystalline Au electrodes. Both CVs portray the same features; however, the electrochemically roughened Au electrode shows higher oxidation and reduction currents, despite the lower scan rate (50 vs. 100 mV/s). The electrochemical roughening procedure (Section 3.2) introduces nanostructures leading to the enhancement of the Raman signals due to laser-excitation of surface plasmons. Therefore, the roughened electrodes possess higher surface areas, as apparent from the

higher oxidation/reduction currents. Nevertheless, the underlying surface electrochemistry is expected to be the same, as both CVs are nearly equal.

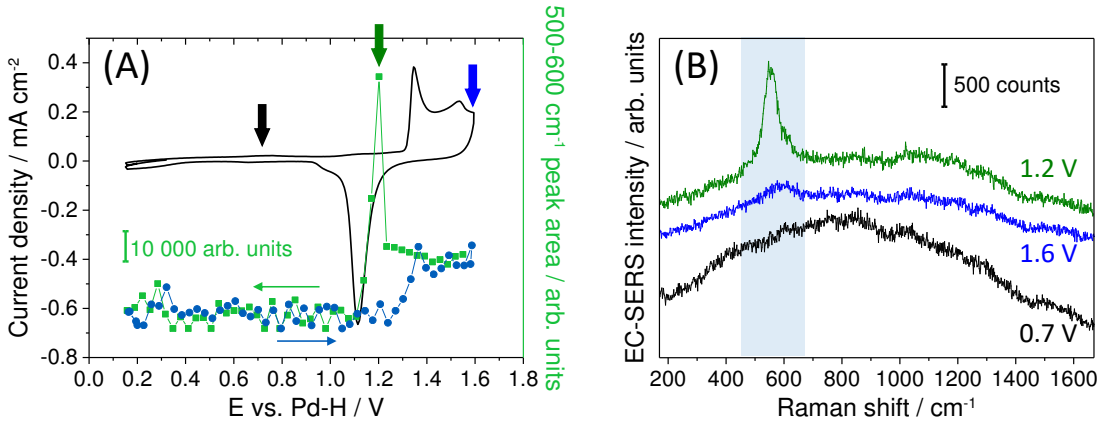

Figure 3.1. *Simultaneous operando SERS and CV measurements. (A) Integrated EC-SERS peak areas in the region between 500 to 600 cm^{-1} for up-scan (dark blue circles) and down-scan (green squares) acquired during CV (black curve, in 0.1 M H_2SO_4) at 50 mV/s scan rate. Thick arrows indicate the potentials (vs. Pd-H reference electrode) at which the respective EC-SER spectra shown in (B) were acquired. The spectra are y-offset for clarity.*

Figure 3.1B shows example EC-SER spectra acquired at different electrode potentials during CV. While at 0.7 V vs. Pd-H no peaks are apparent on top of the broad SERS background, at 1.6 V vs. Pd-H an asymmetric peak around 594 cm^{-1} is visible. During the cathodic scan toward more negative potentials, an intense peak at ∼560 cm^{-1} is observed at the onset of the AuOx reduction (∼1.2 V vs. Pd-H), which differs in peak position and intensity from the broad asymmetric peak around 594 cm^{-1}. The integrated peak intensity of the spectral region between 450 to 650 cm^{-1} (Figure 3.1A, blue dots and green squares for up- and down-scan, respectively) displays the growth of the 594 cm^{-1} peak during surface oxidation from around 1.3 V vs. Pd-H to a plateau intensity between 1.4 and 1.6 V vs. Pd-H. At ∼1.2 V vs. Pd-H during the reverse scan, the EC-SERS intensity suddenly rises and then vanishes below 1.1 V vs. Pd-H scanning further toward more negative potentials.

Further, we performed EC-SERS potential-jump experiments, in which we employed the potential-jump sequence shown in Figure 3.3A (black curve). The potential sequence starts and ends at a potential of 0.65 V vs. Pd-H with a plain Au surface with low sulfate adsorption of less than 4% surface coverage [Ede94, Pfi19c], followed by an upward potential-jump to 1.25 V vs. Pd-H that mirrors the downward potential-jump to 1.25 V vs. Pd-H after surface oxidation at 1.65 V vs. Pd-H. Note that experiments in H_2O- and D_2O-based solutions were performed with a 50 mV potential difference according to

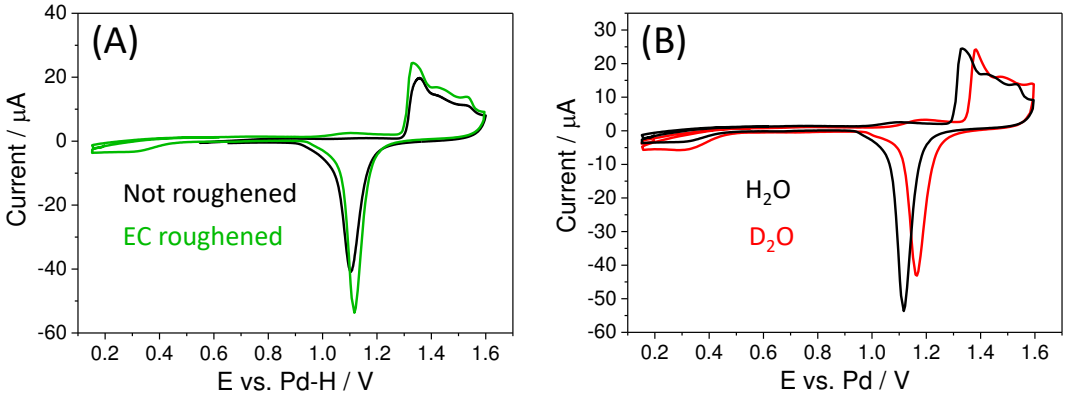

Figure 3.2. *CV of sample electrodes. (A) Comparison between the CVs of the polycrystalline Au electrode (black, scan rate = 100 mV/s) and the roughened polycrystalline Au electrode for EC-SERS experiments (green, scan rate = 50 mV/s) in 0.1 M H_2SO_4. (B) Comparison of CVs of the roughened polycrystalline Au electrode in 0.1 M H_2SO_4 water (black) and deuterium (red) based electrolytes (scan rate = 50 mV/s).*

the observed shift of the RE potential during CV (Figure 3.2B). Figure 3.3 shows the recorded current vs. time traces for the applied potential steps (blue curve) in H_2O- and D_2O-based solutions. We find a current plateau when jumping from 1.6(5) V to 1.2(5) V vs. Pd-H that differs from the exponential current decays observed for the other applied potential-jumps. To gain further insight into the electrochemical response during the

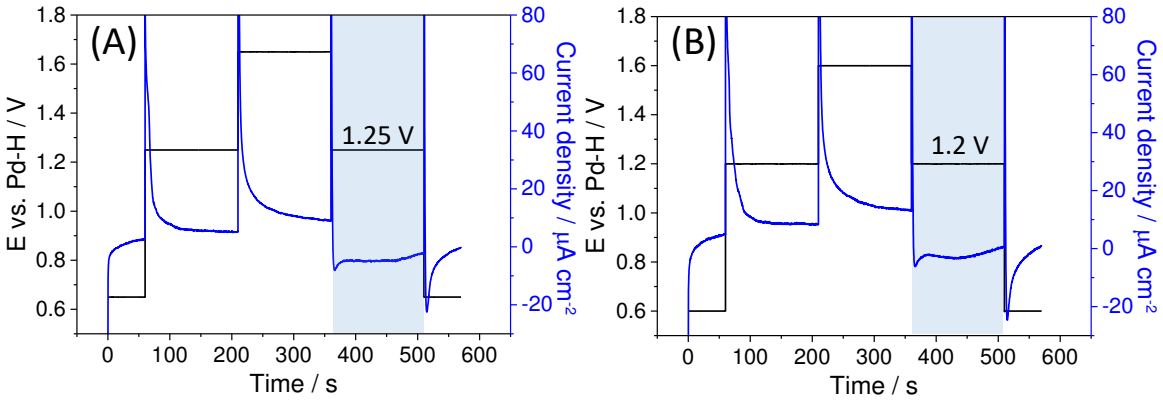

Figure 3.3. *Chronoamperometry during EC-SERS jump-experiments. Current vs. time traces (blue curve) at different applied fixed potentials (black curve) of the roughened polycrystalline Au electrode in (A) D_2O-based and (B) H_2O-based 0.1 M H_2SO_4, recorded in the EC-SERS cell. Light blue area highlights the current plateau.*

potential-jump experiments that we combine with EC-SERS in the following, a number of pure electrochemical measurements were conducted on (not roughened) polycrystalline Au electrodes in 0.1 M H_2SO_4 water-electrolyte. As Figure 3.2A exhibits a slight shift

in the AuOx reduction potential of ∼20 mV, comparing the roughened and not roughened Au electrodes, this potential difference/offset needs to be taken into consideration when comparing the presented purely electrochemical and EC-SERS potential-jump experiments.

The surface oxidation was investigated by linear potential up-scan to 1.4 V, 1.5 V and 1.6 V vs. Pd-H, subsequent potential holding for varied time periods from 0 to 600 s and a final linear potential down-scan (Figure 3.4A). The AuOx reduction peak shifts to more negative potentials with increasing holding times and the integrated charge profiles reveal a strong current increase during the first 60 s (Figure 3.4B). For longer holding times, the charge vs. time curves do not show the expected saturation value of a completely oxidized limited surface area, but show a slow linear increase. This slow linear charge increase might originate from the oxidation of the lower lying Au substrate, as previously observed [TF97].

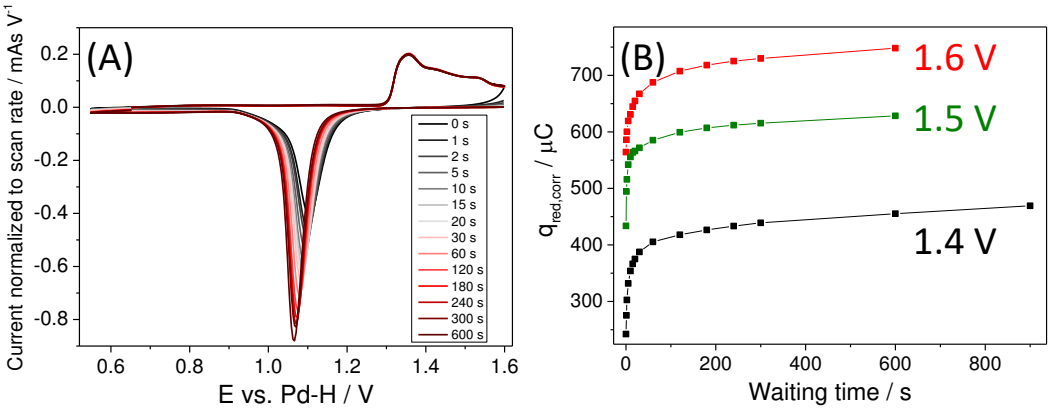

Figure 3.4. *Au surface oxidation for different waiting times. (A) CVs of the (not roughened) polycrystalline Au electrode in 0.1 M H_2SO_4 with different holding times (0 to 600 s) at 1.6 V vs. Pd-H and subsequent continuation of the CV (scan rate = 100 mV/s). (B) Integrated charges for the different holding times at varied upper vertex potentials, UVPs (1.4 V, 1.5 V, 1.6 V vs. Pd-H).*

Figure 3.5A shows the linear potential up-scan to 1.6 V vs. Pd-H that was held for 180 s. The subsequent applied potential in the range from 0.95 to 1.3 V vs. Pd-H was held for 60 s followed by linear potential down-scan shown in Figure 3.5A. The reduction peak increases above 1.125 V vs. Pd-H; for lower potentials, the AuOx surface is fully reduced when the applied constant potentials are held for 60 s. Above 1.125 V vs. Pd-H, the reduction peak increases since the applied potential for 60 s is not sufficient to com-

pletely reduce the AuOx surface. At ∼1.25 V vs. Pd-H or more positive potentials, the full AuOx reduction occurs during the subsequent potential down-scan to more negative potentials. With the increase in AuOx reduction current during the CV down-scan, the peak position shifts to more positive potentials. Figure 3.5B shows the current vs. time traces recorded after the potential-jump from 1.6 V vs. Pd-H and the observed current plateau for the range between 1.1 and 1.19 V vs. Pd-H. According to the applied AuOx reduction (over)potential, the current plateau can be adjusted in its temporal length.

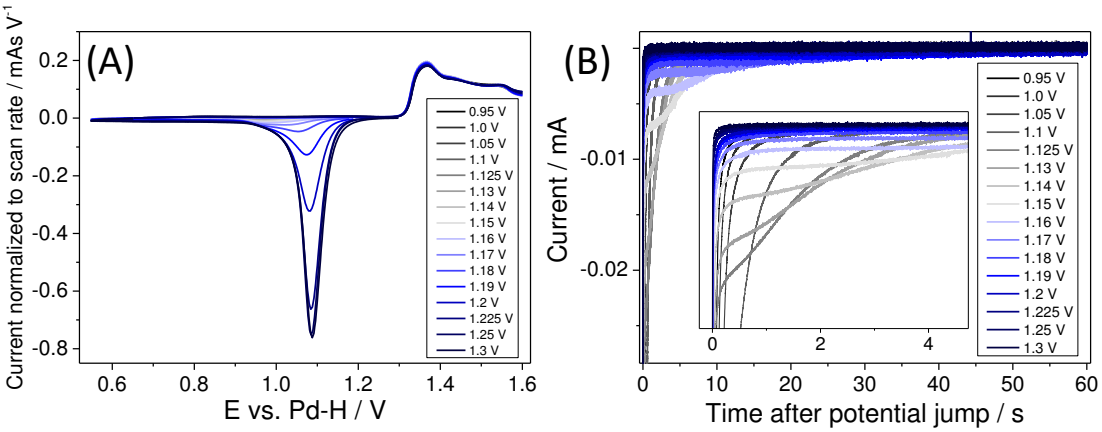

Figure 3.5. *Electrochemical potential-jump experiments. (A) CV up-scan before and CV down-scan after the potential-jumps for a surface oxidation time of 180 s at 1.6 V vs. Pd-H and a holding time of 60 s at the employed potentials (0.95 to 1.3 V vs. Pd-H). (B) Current vs. time traces recorded directly after the potential-jumps, corresponding to the CV up-scan and CV down-scan of (A).*

Further potential-jump experiments were performed with different holding times of specifically applied reduction onset potentials (Figure 3.6). Figure 3.6A shows the resulting CV curves for different holding times, t_j, from 0.1 to 60 s at 1.17 V vs. Pd-H. Figure 3.6B shows the current vs. time traces revealing the previously discussed current plateau. Charge integration of the CV reduction peak, $q_{cv,corr}$ ('corr' indicates that a calibration factor was employed as is discussed in Section 3.8, linear sweep vs. small incremental steps), and the charges detected during the applied reduction potentials, q_t, are plotted as a function of time in Figure 3.6C. As expected, while $q_{cv,corr}$ decreases with increasing t_j, q_t increases approximately in the same fashion. With increasing reduction potentials (from 1.13 to 1.17 V vs. Pd-H, Figure 3.6C), an increased holding time, t_j, is required to fully reduce the AuOx surface, as the reaction proceeds more slowly.

Figure 3.7A shows example EC-SERS raw spectra recorded after the potential-jump from

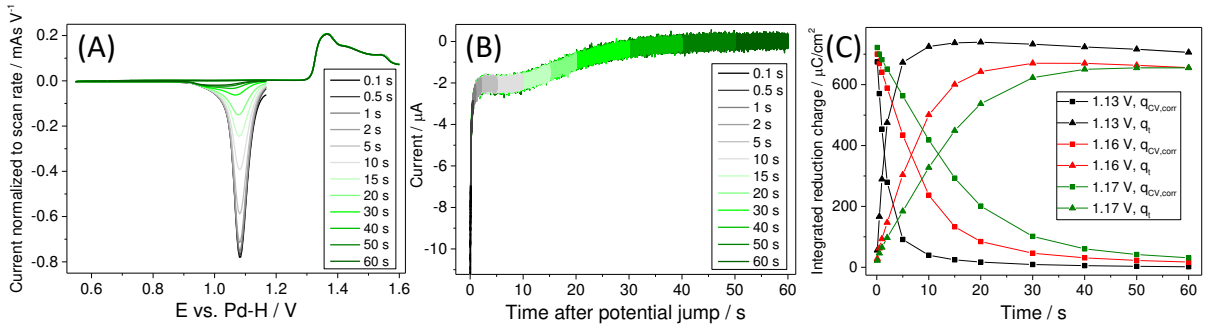

Figure 3.6. *Potential-jump experiments at 1.17 V vs. Pd-H. (A) CV up-scans and down-scans before and after the potential-jumps from 1.6 to 1.17 V vs. Pd-H (scan rate = 100 mV/s) and different potential holding times at 1.17 V vs. Pd-H (0.1 to 60 s). (B) Corresponding current vs. time traces during the variation in potential holding times. (C) Integrated charges from the current vs. time traces and the CV reduction peaks for different holding times, t_j, at 1.13, 1.16 and 1.17 V vs. Pd-H.*

1.65 to 1.25 V vs. Pd-H in D_2O-based 0.1 M H_2SO_4 electrolyte during the first 19 s. The acquisition time accounted to 0.5 s for each spectrum, which are y-offset from another for clarity. The filter cut-off at 156 cm^{-1} is visible, as well as the spectral features assigned to reaction intermediates. The surface cleanliness is confirmed, in accordance with CV measurements, by the absence of peaks in the 1300 and 1500 cm^{-1} region, characteristic for amorphous carbon [Kud00]. Figure 3.7B shows the corresponding EC-SERS intensity map as a function of time after the potential-jump to the reduction onset (1.25 V vs. Pd-H). We observe spectral features with peaks appearing at around 230 cm^{-1}, 350 cm^{-1}, 540-620 cm^{-1}, 750-850 cm^{-1}, 955 cm^{-1}, 1030-1200 cm^{-1}. The relative intensities of the different spectral regions undergo dynamical changes on the second timescale during the electro-reduction of AuOx at 1.25 V vs. Pd-H. Peak positions were determined after linear background subtraction with Lorentzian peak fitting (Section 3.8). The results of the peak fitting of averaged EC-SER spectra are summarized in Table 3.1 for experiments in H_2O- and D_2O-based sulfuric acid electrolytes. Figure 3.8 shows two example EC-SER spectra obtained by averaging the first 60 raw spectra (acquisition time = 0.5 s) after the potential-jump from 1.6(5) to 1.2(5) V vs. Pd-H in H_2O- and D_2O-based 0.1 M H_2SO_4 electrolytes, respectively.

The broad peak around 594 cm^{-1} splits into two peaks after a short delay of approx. 1 to 3 s (Figure 3.7A-C, 540-620 cm^{-1} wavenumber region). The upper peak is located at higher wavenumbers in deuterated water at 617.3 ± 0.7 cm^{-1} compared to 612.6 ± 0.2 cm^{-1} in normal water. The lower peak at 560.4 ± 1.8 cm^{-1} in normal water is located

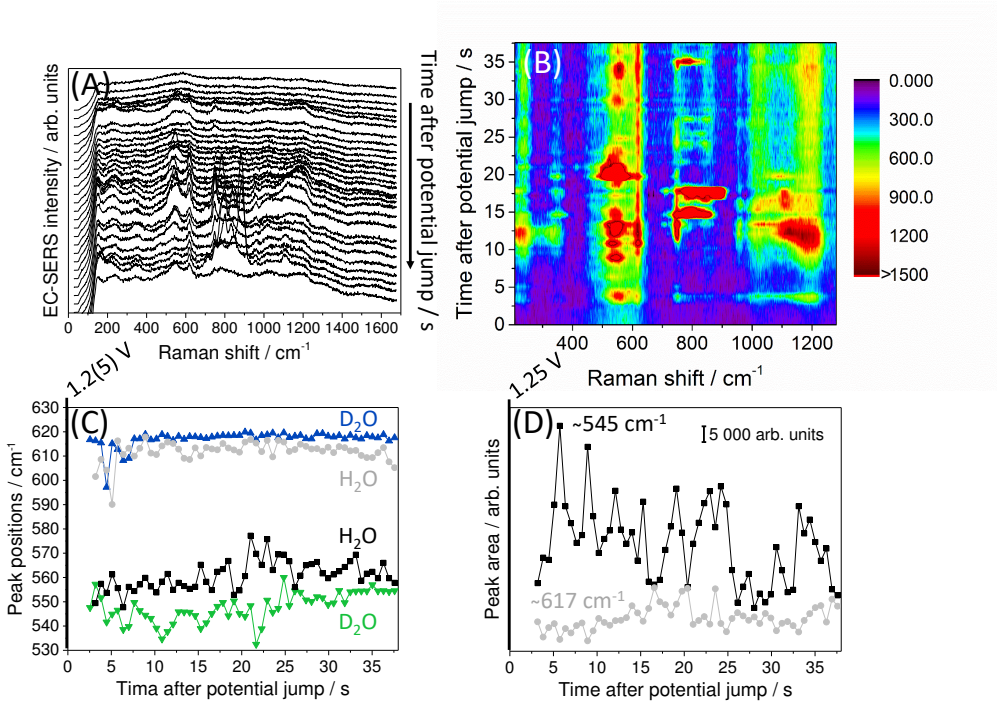

Figure 3.7. *EC-SERS potential-jump experiments. (A) EC-SER example raw spectra as a function of time after the potential-jump from 1.65 to 1.25 V vs. Pd-H in D_2O-based 0.1 M H_2SO_4 electrolyte during the first 19 s (acquisition time = 0.5 s per spectrum). (B) EC-SERS intensity map as a function of time for the first 38 s after the potential-jump from 1.65 V to 1.25 V vs. Pd-H. (C) Comparison of peak positions of the double peak feature within the 530-630 cm^{-1} spectral region in H_2O- and D_2O-based 0.1 M H_2SO_4 electrolyte experiments. (D) Peak areas of the ∼545 cm^{-1} and ∼617 cm^{-1} Raman bands as a function of time after the potential-jump from 1.65 to 1.25 V vs. Pd-H.*

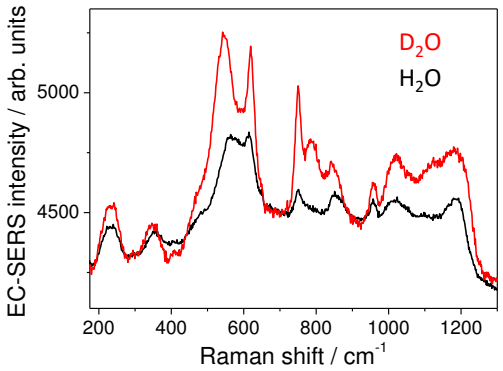

Figure 3.8. *EC-SER example spectra averaged from the first 60 raw spectra (acquisition time = 0.5 s) after the potential-jump from 1.6(5) to 1.2(5) V vs. Pd-H in H_2O- (black) and D_2O-based (red) 0.1 M H_2SO_4 electrolytes. Spectra are y-offset for clarity.*

at 545.5 ± 2.9 cm^{-1} in deuterated water. The lower wavenumber peak at ca. 560 cm^{-1} shows oscillations in intensity (Figure 3.7B,D) with an average oscillation period of 4.2 ± 1.5 s in H_2O- and D_2O-based electrolytes. The peak area oscillation frequency of the Au-OH band at ∼560 cm^{-1} was determined by Gaussian peak fitting (OriginPro) of the previously determined peak area as a function of time traces (e.g. Figure 3.7D) at 1.2(5) V vs. Pd-H (after AuOx formation) and determination of the differences of subsequent peak positions. The oscillation frequencies in H_2O- and D_2O-based 0.1 M H_2SO_4 electrolytes accounted to 4.0 ± 1.3 s and 4.5 ± 1.9 s, respectively.

The bands at 350.5 ± 0.6 cm^{-1} and 956.6 ± 1.0 cm^{-1} exhibit a slight difference in peak position of about 1 to 3 cm^{-1} when comparing H_2O- and D_2O-based electrolyte experiments (347.7 ± 1.2 cm^{-1}; 954.7 ± 0.6 cm^{-1}). All other peak positions are independent of isotope exchange (Table 3.1) according to overlapping standard deviations determined from different experimental rounds. Figure 3.9A shows the EC-SERS spectral evolution

Table 3.1. *Peak positions in H_2O and D_2O solutions. Determined peak positions in H_2O- and D_2O-based electrolyte solutions after jumping from 1.6(5) to 1.2(5) V vs. Pd-H (see Section 3.8 for analysis details), i.e. after surface oxidation, and possible peak assignment according to experiments/DFT calculations/literature as discussed in the text. Black arrows: peak up- or down-shift upon deuteration. (—): within standard deviation.*

Peak position in H_2O	Peak position in D_2O	Δpeak position	Peak assignment
232.7 ± 1.9 cm^{-1}	233.9 ± 0.9 cm^{-1}	—	$(H)SO_4^{(2)-}$ [Ata98, Bro95]
350.5 ± 0.6 cm^{-1}	347.7 ± 1.2 cm^{-1}	↓	Au–OH (weakly bound) [Exp./DFT]
560.4 ± 1.8 cm^{-1}	545.5 ± 2.9 cm^{-1}	↓	Au-OH stretching [Exp./DFT]
612.6 ± 0.2 cm^{-1}	617.3 ± 0.7 cm^{-1}	↑	O-Au(-OH) [Exp./DFT]
751.7 ± 4.9 cm^{-1}	749.7 ± 1.6 cm^{-1}	—	O-Au-O [Exp./[Wan01]]
771.4 ± 3.7 cm^{-1}	783.7 ± 11.2 cm^{-1}	—	O-Au-O [Exp./[Wan01]]
853.0 ± 1.9 cm^{-1}	850.7 ± 2.0 cm^{-1}	—	$(H)SO_4^{(2)-}$ [DFT/[Ata98, Bro95]]
956.6 ± 1.0 cm^{-1}	954.7 ± 0.6 cm^{-1}	↓	HSO_4^- [Exp./[Shi99]]
1030.6 ± 5.9 cm^{-1}	1030.0 ± 4.2 cm^{-1}	—	$(H)SO_4^{(2)-}$ [Ata98, Bro95]
1136.8 ± 21.7 cm^{-1}	1135.1 ± 29.7 cm^{-1}	—	$(H)SO_4^{(2)-}$ [Ata98, Bro95]
1190.9 ± 3.8 cm^{-1}	1197 ± 7.2 cm^{-1}	—	SO_4^{2-} [Ata98]

as a function of time at 1.25 V vs. Pd-H before jumping to the AuOx formation. Figure 3.9B reveals the spectral evolution at 1.65 V vs. Pd-H and the appearance of the broad and asymmetric peak around 594 cm^{-1} due to AuOx. Figure 3.9C-F compares the EC-SER spectral evolution at the onset reduction potential of AuOx at 1.2(5) V vs. Pd-H. Intense

spectral features, in comparison to Figure 3.9A, are apparent. By comparing different rounds of experiments (Figure 3.9C-F), it is evident that the spectral features are well reproducible; however, oxidation/reduction cycles also further roughen the nanostructure surface composition that apparently results into differences in the temporal appearance of the different spectral features (e.g. 750-850 cm^{-1} region). It is important to note that since multiple hotspots likely contribute to the acquired signal, the EC-SER spectra as a function of time do not necessarily reflect the temporal order of the observed reaction intermediates.

3.4 EC-SERS potential-jump approach

During the electro-reduction of the AuOx surface at the onset potential of 1.2 V vs. Pd-H (CV in Figure 3.1A), EC-SER spectra reveal dynamically-evolving spectral features (Figure 3.7A,B and 3.9), which we attribute to different reaction intermediates. Potential-jumps to more negative potentials than 1.2 V vs. Pd-H speed up the encountered reaction due to larger overpotentials (Figure 3.5), while less negative potentials than 1.2 V vs. Pd-H stop the reaction, making it either too fast or too slow for our experimental procedure with a spectral acquisition time of 0.5 to 1 s to efficiently follow the reaction intermediates as a function of time. Accordingly, we are able to observe the reaction intermediates of the AuOx electro-reduction only when the applied electrode potential is around the reduction onset region (∼1.2 V vs. Pd-H). Our electrochemical potential-jump measurements reveal a current plateau at potentials around 1.2 V vs. Pd-H that can be tuned according to variations in applied potentials of tens of mV and show that the time required to reduce the surface oxide is in the range from several seconds to minutes (Figure 3.3, 3.5 and 3.6). This observation is in agreement with the literature, where the AuOx reduction reaction has been reported to occur on a broad window of time scales from µs to minutes depending on the applied electrode potential [Ben16, Shr14, Gir15, Vel90]. The potential-jump from surface oxidation potentials directly to the reduction reaction onset allows spectroscopic monitoring of electrochemical species over a time range of several tens of seconds that would otherwise (mostly) be hidden during potential sweep measurements (cf. Figure 3.7A,B and Figure 3.1). The complementary approach to simultaneously acquire spectra during CV (shown in Figure 3.1) provides a more narrow time window of about 7 s (in this case) for complete surface reduction and gives potential-averaged insight. Nevertheless, the appearing spectral feature at ∼560 cm^{-1} around 1.2 V vs. Pd-H in Figure 3.1 supports the distinguished electrode behavior with reduced kinetics around the reduction onset potential.

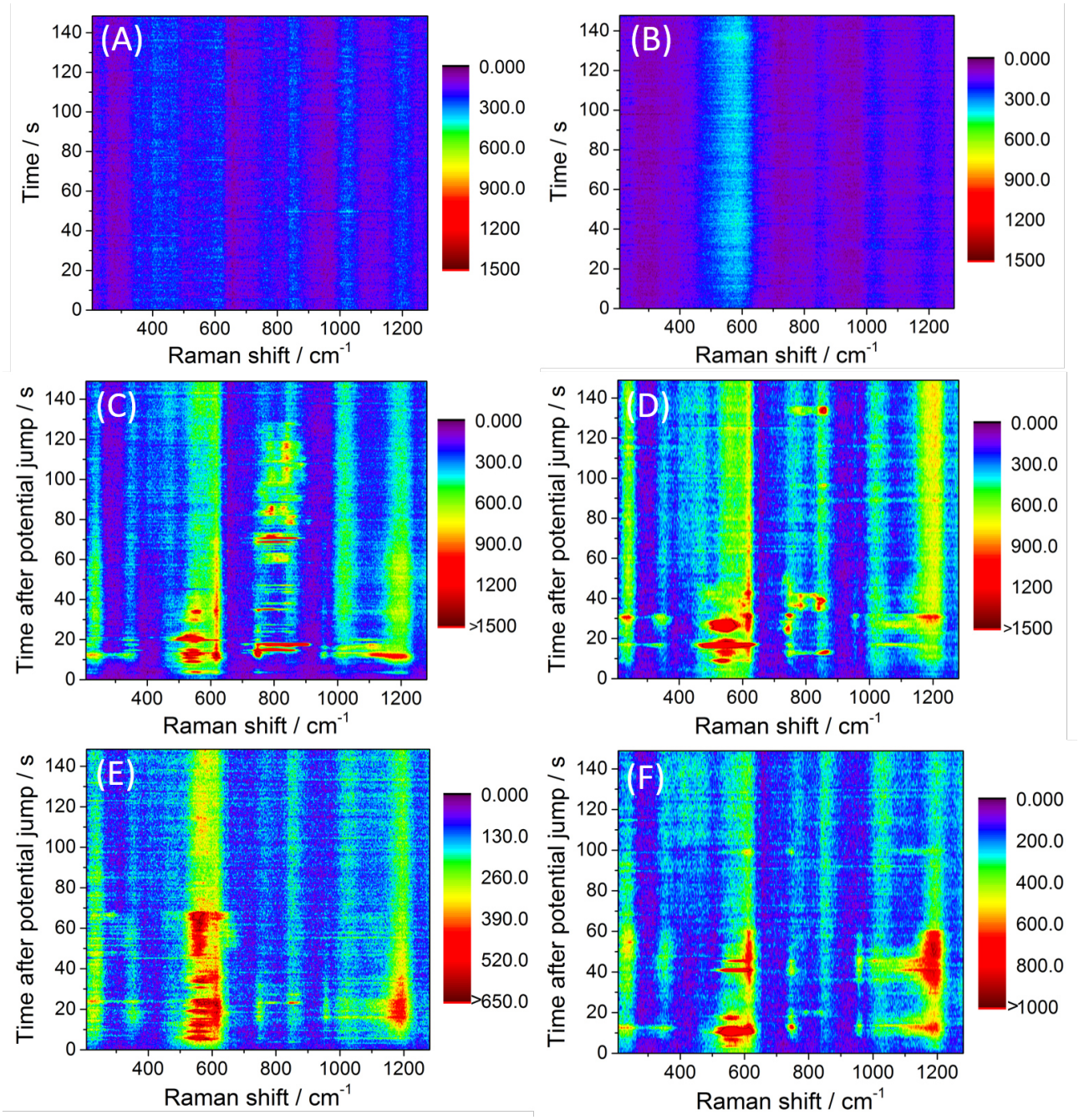

Figure 3.9. *EC-SER spectral evolution as a function of time. (A) EC-SER spectra recorded at 1.25 V vs. Pd-H before jumping to surface oxidation at 1.65 V vs. Pd-H. (B) EC-SER spectra recorded as a function of time at 1.65 V vs. Pd-H. (C-F) EC-SERS spectral evolution as a function of time at 1.25 V vs. Pd-H in D_2O-based (C, D) and at 1.2 V vs. Pd-H in H_2O-based (E,F) 0.1 M H_2SO_4. Spectral acquisition times: 0.5 s (A-C, E); 1 s (D, F).*

The recorded EC-SER spectra during potentiostatic AuOx reduction represent an ensemble response from multiple SERS-hotspots at the surface [Fan08] and the observed

spectral time-evolution is therefore also an average. During the electro-reduction, the SERS background retains its shape suggesting that the plasmonic hotspot remains intact (Figure 3.7A). To compensate for changes in the overall SERS background intensity and possible related near-field artefacts, we analyze background-subtracted data to extract the underlying surface chemistry (Section 3.8).

3.5 Identification of reaction intermediates

3.5.1 Au-OH intermediates

The broad and asymmetric peak at ∼594 cm^{-1} observed at 1.6 V vs. Pd-H (Figure 3.1B) that, according to literature [Des86], originates from formed AuOx species, splits into two peaks after the potential-jump from 1.6 to 1.2 V vs. Pd-H: one located at ∼560 cm^{-1} and one at ∼613 cm^{-1}. The 560 cm^{-1} peak can be assigned to Au-OH according to isotope exchange experiments and implicit solvent DFT calculations that reveal a difference in peak position of about 15 cm^{-1} [Pfi19b]. Assuming adsorbed OH species to behave as a simple harmonic oscillator, we calculate the expected isotopic frequency shift to be $\Delta = \sqrt{m_{OH}/m_{OD}} = \sqrt{(16+1)/(16+2)} \approx 0.972$. Using this isotopic shift factor, we calculate the expected frequency in D_2O electrolytes for the 560 cm^{-1} peak to be $0.972 \cdot 560.4$ $cm^{-1} \approx 544.7$ cm^{-1}, which corresponds very well to the experimentally obtained value of 545.5 ± 2.9 cm^{-1}. The Weaver group reported a vibrational band in alkaline media at 520-580 cm^{-1}, which was attributed to Au-OH [Des86, Zha93]. In acidic solutions, Weaver and co-workers observed potential-dependent spectral features around 550-580 cm^{-1} that partly down-shifted upon isotope exchange, but their origin remained elusive [Zha93]. DFT calculations predict the 560 cm^{-1} peak to OH species attached to Au adatoms (Figure 3.10B and Table 3.2B) supporting the Au-OH assignment. The availability of Au adatoms on rough Au is expected, also due to further surface roughening during the reported place-exchange between Au and O/OH surface atoms and the Au dissolution during AuOx reduction [Che13, Sch97].

We further confirm that such Au-OH species are metastable in acidic solutions, as the interface structure of Figure 3.10B is never predicted to be the most stable interface structure within the applied potential range [Pfi19b], which explains the challenge to monitor such intermediate species in acids experimentally. The implicit model employed could in principle underestimate the solvation energy of the OH-adsorbed species for which hydrogen bonding probably plays a relevant role. However, accounting for an additional stabilization of these interfaces through a downward shift of the corresponding formation-

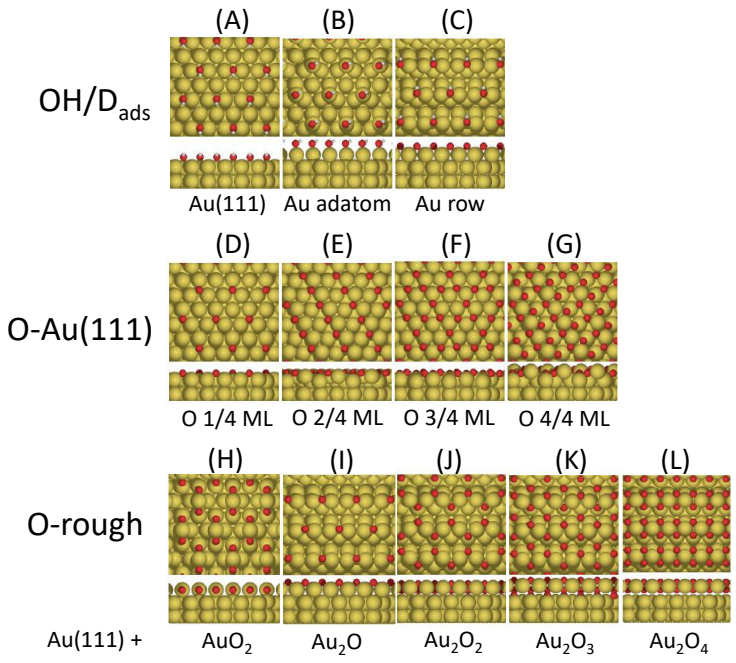

Figure 3.10. *Illustration of the most stable interface structures for the calculations of Au-OH and AuOx vibrational frequencies according to Ref. [Pfi19b]. Oxygen, hydrogen and Au atoms are shown in red, gray and yellow, respectively. For each structure, top and side views are presented. (A-C) Most stable OH-adsorption configurations (according to geometry optimization) on the flat and roughened Au surfaces. (D-G) Illustration of the partially oxidized structures originating from a flat Au(111) surface. ML denotes monolayer. (H-L) Structures originated from 'roughened' surfaces (i.e. including one or two Au adatoms per unit cell) with different amounts of oxygen atoms.*

energy curves by few hundreds of meV would not give a qualitatively different picture [Pfi19b]. Consequently, OH formation can become stable either in a very narrow potential window or through a change in local surface pH. Our results indicate that the formation of (metastable) adsorbed OH represents a step during the dynamic reduction of AuOx, as was previously suggested in the literature [AK86]. The observed periodic intensity oscillations of the Au-OH peak at 560 cm^{-1} and the disappearance of the OH signal after about 50 to 100 s (Figure 3.7 and 3.9) are in accordance with (metastable) short-lived OH-intermediates that further react to form water during the reduction process.

Moreover, another intermediate peak at ∼351 cm^{-1} (Figure 3.7A,B) is assigned to Au-OH, though less intense than the Au-OH at 560 cm^{-1}, that shows a slight down-shift in peak position of about 1 to 3 cm^{-1} moving from water to deuterium (Table 3.1). DFT calculations also show small frequency down-shifts of 3 to 6 cm^{-1} upon deuteration (Table 3.2)

Table 3.2. *Highest frequencies computed for Au-OH/D and AuOx according to Ref. [Pfi19b]. (Upper panel) Surface-OH/D stretch frequencies calculated for the structures involving adsorbed OH/D illustrated in Figure 3.10A-C. (Lower panel) Maximum frequencies calculated for the oxygen-containing structures illustrated in Figure 3.10D-L.*

Interface	Au-OH/D frequency in vacuum	Au-OH/D frequency in solvent
(A)	328/322 cm^{-1}	316/312 cm^{-1}
(B)	558/534 cm^{-1}	531/517 cm^{-1}
(C)	371/365 cm^{-1}	361/358 cm^{-1}
Interface	**Max. frequency in vacuum**	**Max. frequency in solvent**
(D)	384 cm^{-1}	381 cm^{-1}
(E)	446 cm^{-1}	442 cm^{-1}
(F)	437 cm^{-1}	441 cm^{-1}
(G)	581 cm^{-1}	583 cm^{-1}
(H)	600 cm^{-1}	599 cm^{-1}
(I)	482 cm^{-1}	480 cm^{-1}
(J)	585 cm^{-1}	585 cm^{-1}
(K)	594 cm^{-1}	601 cm^{-1}
(L)	609 cm^{-1}	621 cm^{-1}

[Pfi19b], in accordance with experiments. In alkaline media, a feature at 360-420 cm^{-1} was previously attributed to Au-OH stretching [Des86, Li15, Zha93]. With DFT, we can confirm that the 351 cm^{-1} peak originates from Au-OH species in a bridge site surface geometry (Figure 3.10A,C) less strongly bound to the Au surface compared to the Au-OH at 560 cm^{-1}. The appearance of two Au-OH species that can be assigned to adsorbed OH-species strongly (560 cm^{-1}) and less strongly bound (351 cm^{-1}) to the surface suggests that the AuOx surface is reduced by proton adsorption and electron transfer to form the adsorbed OH intermediates and subsequent release of the OH species from the surface to form water, in agreement with suggestions in the literature [Con95, AK86, Peu84].

3.5.2 Gold oxide intermediates

The broad AuOx peak at ∼594 cm^{-1} observed at 1.6 V vs. Pd-H (Figure 3.1B blue spectrum) splits into two peaks after the potential-jump from 1.6 to 1.2 V vs. Pd-H. While the lower 560 cm^{-1} peak is Au-OH, the higher wavenumber peak located at ∼613 cm^{-1} can, according to DFT simulations [Pfi19b], be attributed to a AuOx structure that is characterized by Au atoms in a 4-fold coordination with oxygen (Figure 3.10L), as the computed frequencies (vacuum: 609 cm^{-1}, solvent: 621 cm^{-1}) are close to the experimentally observed one at 613 cm^{-1}. The Au atoms in a 4-fold coordination with oxygen are also observed in the form of bulk gold oxide, Au_2O_3 [Jon80]. The experimentally

observed slight up-shift in peak position of about 4 cm^{-1} in a D_2O electrolyte can be explained by protonation of the interface structure in Figure 3.10L (i.e. adding a H-atom to the (unit cell) structure): The frequency computed in implicit solvent for the (partially) protonated surface structure is 601 cm^{-1}, and it shifts to 602 cm^{-1} when H is replaced with D, supporting the experimentally observed trend. Intuitively, this effect can be understood when the influence of OH species in close proximity to the oxide structure is considered: While the deuterium atom can be expected to be less mobile due to its higher mass compared to hydrogen, the hydrogen atom can, to some extent, be 'shared' with neighboring oxygen atoms. As a consequence, the neighboring oxygen atom has a slightly higher effective mass which results into a lower peak position in water ($\sim$613 cm^{-1}). In deuterated electrolyte, the heavier and less mobile deuterium atom remains at its Au-OD position and the neighboring atoms have a lower effective mass leading to the observed peak position up-shift to $\sim$617 cm^{-1} in the D_2O case. The oxide intermediate is apparently a more ordered AuOx surface structure, resembling a coordination symmetry similar to bulk Au_2O_3, formed during the reduction process, as the peak width of the 613 cm^{-1} peak is substantially more narrow (FWHM: $\sim$28 cm^{-1}) than the initial broad 594 cm^{-1} AuOx feature at 1.6 V vs. Pd-H (FWHM: $\sim$130 cm^{-1}).

It is important to remember that one of the challenges in understanding the AuOx reduction mechanism as well as the OER in full detail is the uncertainty about the actually formed AuOx composition. We find that the calculated surface oxide structures that involve minor surface reconstructions and that could be classified as oxygen-atom adsorption (see Figure 3.10D-F,I) are characterized by a maximum frequency that does not exceed 500 cm^{-1}. Larger frequencies (>550 cm^{-1}) are observed for interfaces where one or multiple Au atoms are clearly oxygen-coordinated, which can be classified as 'entangled' or reconstructed surface-oxide structures [Pfi19b]. These results indicate that the broad 594 cm^{-1} peak originates from a AuOx 'network' (possibly also involving hydrogen) rather than from simply adsorbed oxygen atoms, which is supported from the observed surface roughening during oxidation/reduction previously observed in XPS and STM studies and can be expected in the context of a place-exchange mechanism between Au and O/OH-species [Sch97, Rod03b]. We note that the broad 594 cm^{-1} AuOx peak could in principle also be consistent with a bulk Au_2O_3 phase, for which the calculated phonon density of states presents a broad feature in the frequency region from 500 cm^{-1} to 580 cm^{-1} [Pfi19b]. However, DFT calculations reveal a number of calculated frequencies in the region between 580 to 600 cm^{-1} (Table 3.2) indicating that the broad 594 cm^{-1} peak at 1.6 V vs. Pd-H could originate from multiple gold oxide/hydroxide structures (as proposed

by Weaver and co-workers [Des86]) rather than from a 'single species'.

The spectral features at ∼752 cm^{-1} and ∼771 cm^{-1} during AuOx reduction were stable in peak position upon change of deuterated electrolyte suggesting these species to neither contain hydrogen nor to closely interact with other hydrogen-containing species (Table 3.1; no overlap within standard deviation). It is noteworthy that peaks within this spectral region have previously been assigned to OH bending, O-OH species or H_2O_2 [Li15, DM13, Kim06, Li03]. For example in neutral and alkaline media, based on EC-SHINERS on Au single crystal electrodes, a Au-OH bending mode was reported at 807 and 790 cm^{-1}, respectively, that exhibited a shift of around 100 cm^{-1} upon H_2O/D_2O comparison [Zhu13, Li15]. Diaz-Morales et al. calculated the vibrational frequencies of adsorbed O-OH and OH species averaged for different surface geometries to be 824 ± 25 cm^{-1} and 754 ± 43 cm^{-1}, respectively [DM13]. A possible pathway to form such O-OH or H_2O_2 species might involve the formation of O_2 during Au oxidation at ∼1.6 V vs. Pd-H, as suggested in the literature [DM13], the subsequent reduction of O_2 to H_2O_2 at ∼1.2 V vs. Pd-H (which would account to an unusually low ORR overpotential), and a final H_2O_2 oxidation step. However, the formation of O-OH or H_2O_2-related intermediates during the AuOx reduction is not at all obvious. According to laser-ablation (low-temperature) IR experiments and DFT calculations by Wang and Andrews [Wan01], the peaks at ∼752 cm^{-1} and ∼771 cm^{-1} can be assigned to O-Au-O complexes. Short-lived AuOx complexes can be expected to be formed during AuOx reduction and concomitant Au dissolution [Che13], but have not been identified to date during electrochemical reduction experiments. Since the experimentally observed spectral shifts lie within the standard deviation upon deuteration for the 752 and 771 cm^{-1} peaks and in accordance with DFT calculations by Wang and Andrews [Wan01], we tentatively attribute both peaks to O-Au-O complexes.

3.5.3 Role of (bi)sulfate anions

Besides the identified OH- and oxide-intermediates, (bi)sulfate ions from the electrolyte appear at the electrode surface during the surface reduction. The band at ∼957 cm^{-1} is assigned to adsorbed HSO_4^{1-} according to work by Shingaya and Ito [Shi99]. This peak assignment is in agreement with the observed slight down-shift in peak position in deuterated water compared to H_2O-based electrolyte of about 2 cm^{-1} (Table 3.1). Using EC-SEIRAS, we have previously studied the coverage-dependent peak shift of sulfate species from ∼1173 cm^{-1} to ∼1191 cm^{-1} adsorbed on Au(111) at 1.2 V vs. RHE [Pfi19c]. Based on these results, the observed peak at 1191.9 ± 3.8 cm^{-1} is assigned to sulfate. The peaks

at ∼233 cm^{-1}, ∼1031 cm^{-1} and ∼1137 cm^{-1} can also be assigned to (bi)sulfate species with different geometry and coordination [Ata98, Bro95]. Furthermore, DFT calculations of sulfate adsorbed to Au(111) in a tri-dentate configuration suggest the experimentally observed peak at ∼853 cm^{-1} to originate from the S-O vibration where the oxygen is in contact with Au [Pfi19b]. However, such a band around 853 cm^{-1} has not been reported for EC-SHINERS measurements on single crystal Au(111) [Zhu13]. Previous IR and Raman studies of sulfuric acid solutions, though, attributed a band around 876-895 cm^{-1} to the S-OH stretching of bisulfate [Ata98, Bro95]. The well-defined ordered adlayer formed on Au(111) composed of (bi)sulfate as well as water or hydronium ions [Mag92, Cue00] can explain the deviation between our experiments/DFT simulations and the absence of the 853 cm^{-1} band on Au(111).

Sulfate adsorption is known to be strongest on Au(111) and weaker on other facets [Ata98]. Since we observe clear (bi)sulfate signal only during the potential-jump to the reduction onset, but not on the reduced rough polycrystalline Au electrode, we expect (bi)sulfate to participate in the reduction process by temporarily shielding the charged Au after Au-O bond breaking. In this process, the local surface charges and the surface pH dictate the nature (sulfate or bisulfate), orientation and adsorption geometry of the (bi)sulfate, as well as the extent of Au^+ dissolution [Che14b]. The presence of both sulfate and bisulfate species on Au(111) electrodes is supported for D_2O-based electrolytes through IR experiments performed by Shingaya and Ito [Shi99]. The number of 6 Raman active (bi)sulfate modes, the polycrystallinity of the electrode and the surface roughening upon place-exchange between Au and O/OH species support the view of different (bi)sulfate orientation and adsorption configurations.

3.6 Gold oxide electro-reduction mechanism

Considering the presented and discussed results, we can infer the following tentative reaction mechanism: Starting from a polycrystalline AuOx surface with different oxide structures (Figure 3.11A), here the Au_2O_3 structure, as indicated by the broad and asymmetric peak at ∼594 cm^{-1}, the Au-O bonds are stepwise broken resulting in a locally charged surface (Figure 3.11B). The negative surface charges promote proton adsorption and the formation of adsorbed OH-species (∼560 cm^{-1} peak), while concomitantly the positively charged Au is screened by (bi)sulfate ion adsorption (Figure 3.11C). The extent of surface charging and the underlying surface geometry determine the nature of the ions (sulfate or bisulfate) as well as their orientation configuration leading to the

different (bi)sulfate peaks. If surface charge screening by anion adsorption is insufficient, oxygenated Au species and/or (bi)sulfate-complexed/screened Au partly dissolve, as suggested by Mayrhofer and co-workers [Che13, Che14b], which explains the observed O-Au-O intermediates at 750-795 cm^{-1}. The depletion of protons close to the electrode-electrolyte interface upon OH formation presumably leads to an increase in surface pH, stabilizing the observed OH-species long enough to obtain their EC-SERS signatures. The OH-species bound to Au adatoms ($\sim$560 cm^{-1}) then leave the surface to form water resulting into the more weakly bonded Au-OH-signal at $\sim$351 cm^{-1} (Figure 3.11D). The observed intensity oscillations of the OH-signal for the first 50 to 100 s after the potential-jump from surface oxidation to reduction onset indicate the stepwise release of OH-species from the surface to form water that is replenished with subsurface-O/OH species through the place-exchange between Au and O/OH species [Con95]. The (bi)sulfate ion screening of the positively charged Au presumably promotes further Au-O bond breaking (Figure 3.11D) and further iterations of the Au-O reduction steps until a pristine Au surface is obtained.

Interestingly, such dynamic surface rearrangement accompanied by charge transfer across the electrochemical interface is expected to alter the local pH at the surface and thus enables the brief stabilization of OH-adsorbates also in acidic media. While OH-intermediates have been assumed to be formed during the AuOx reduction in sulfuric electrolytes, such adsorbed OH-species in acidic environments have, to the best of our knowledge, not been reported yet, due to the rapid proceeding of the reduction reaction at larger overpotentials in comparison to this work. We assume that such OH-intermediates can also be formed during the electro-oxidation of Au, however, are challenging to observe due to the short residence time at the surface and the spectral overlap with the AuOx peak at $\sim$594 cm^{-1}.

3.7 Conclusions and Outlook

In summary, we have employed EC-SERS electrochemical potential-jump experiments to directly monitor and identify reaction intermediates during the mild electro-reduction of AuOx in acidic solutions revealing gold oxide, OH and (bi)sulfate intermediates. We find Au-OH intermediates to be present during the AuOx electro-reduction even in acidic media and observe a peak splitting of the broad AuOx spectral feature $\sim$594 cm^{-1} into two bands originating from Au-OH and AuOx. The Au-OH stretching mode at $\sim$560 cm^{-1} further reveals periodic intensity oscillations, indicative for the stepwise release of

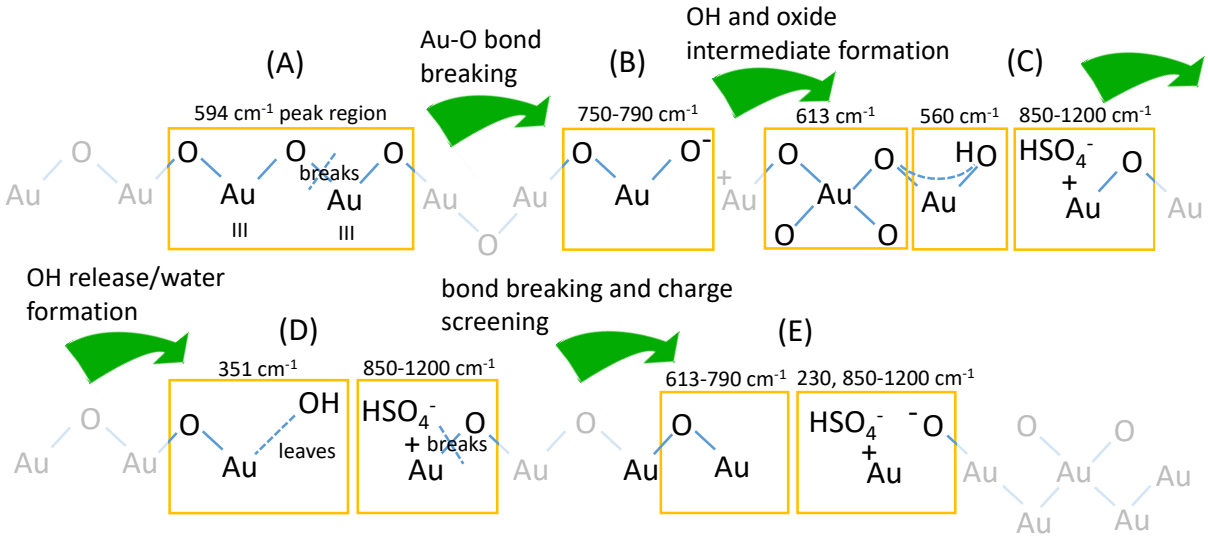

Figure 3.11. *Tentative AuOx reduction mechanism. (A-B) Surface AuOx bonds are stepwise broken. (C) Protons are subsequently adsorbed and OH-species are formed leading to the observed OH-signal at ∼560 cm^{-1} and surface AuOx at ∼613 cm^{-1}. The proton of the adsorbed OH is partly shared by the surface AuOx (indicated for the 'O-Au(-OH)'), which explains the upshift in peak position for the ∼613 cm^{-1} peak upon deuteration. (Bi)sulfate ions screen the positively charged Au after bond breaking. (D-E) Less strongly bonded OH-species are indicative for OH species leaving the surface while further bond breaking is promoted by (bi)sulfate screening. Oxygenated Au or (bi)sulfate Au complexes can possibly also partly dissolve during the dynamic place exchange between lower lying (hydr)oxides and Au atoms.*

OH from the surface during place-exchange between Au and O(H) species. We suggest a AuOx surface structure resembling a bulk Au_2O_3 configuration to be present at the surface during electro-reduction. In addition, (bi)sulfate ions are actively participating in the dynamic formation of short-lived reaction intermediates by presumably shielding local surface charges and likely promote the partly dissolution of Au and/or (bi)sulfate/oxygenated Au complexes.

It is the direct potential-jump to the onset of an electrochemical reaction for the spectroscopic monitoring of reaction intermediates as a function of time that offers a unique pathway to gain further understanding of even long-studied reaction systems (such as Au surfaces in H_2SO_4). Extending our EC-SERS potential-jump approach to the EC-SHINERS technique [Li10] and EC-TERS [Pfi18] to gain further insight on well-defined single crystal model electrodes are exciting future venues that will ultimately provide the necessary mechanistic understanding to aid the rational engineering of highly active and

robust future energy materials. We have set the scene for our nanoscale chemical imaging experiments (Chapter 5) by providing evidence that EC-SERS on simple electrochemically roughened polycrystalline Au surfaces offers sufficient SERS enhancement to detect various reaction products/intermediates under reaction conditions. With similar Raman enhancement factors as EC-SERS, EC-TERS can be expected to detect similar reaction products/intermediates at well-defined model surfaces.

3.8 Data processing and analysis

Data acquisition and processing of EC measurements

The Nova 2.1.2 software (for the Metrohm Autolab PGSTAT 30 multipotentiostat) does not provide the means to combine the potential-jump experiments with analog linear sweep/CV measurements. Therefore, a digital staircase voltage profile was utilized, in which the applied potential is adjusted in very small and adaptable step-sizes. Additional test measurements showed that the CV shapes with linear and staircase acquisition match best for a step size of 0.002 V.

To ensure that we obtain the correct absolute charge values from the CV curves, a calibration method was employed: At the start of each set of measurements, a complete CV of the desired potential range was recorded using the linear voltage profile as well as the staircase voltage profile (step size = 0.002 V). The extracted reduction charges were determined and provide a calibration factor to accurately compare the charges during the potential-jump and CV experiments, under the assumption that the calibration factor does not change upon adjustment of the potential-jump parameters.

The charges from the CVs were determined by subtraction of the local maximum (negative current range) after the reduction peak (to more negative potentials) and before the onset of the double layer currents as constant baseline. Subsequently, the peak area under the reduction peak was integrated. For the jump experiments, the areas under the current vs. time traces were determined.

EC-SERS data analysis

The peak positions from the EC-SERS jump experiments (Table 3.1) were extracted from averaged EC-SER spectra (e.g. Figure 3.8) from the first 60 or 30 single spectra recorded after the potential-jump from Au oxidation to 1.2(5) V vs. Pd-H for acquisition times of

0.5 or 1 s, respectively. A linear background (autozero = 1) was subtracted and Lorentzian peak fitting was performed with matlab software (peakfit.m, matlab file exchange). The following peak regions were considered: 182-282 cm^{-1} (single peak); 296-396 cm^{-1} (single peak); 416-686 cm^{-1} (double peak); 711-914 cm^{-1} (triple peak); 934-977 cm^{-1} (single peak); 975-1272 cm^{-1} (triple peak). For Figure 3.7C,D, single EC-SER spectra were fitted employing the same matlab code and procedure. For the broad and asymmetric peak around 594 cm^{-1} at 1.6 V vs. Pd-H, a peak region of 402-737 cm^{-1} was fitted with the least number of peaks to give a reasonable fit (determined to be 3 peaks). In addition, we have simply determined the peak maximum as shown in Table 3.3.

Table 3.3. *Determined AuOx peak positions at 1.6 V vs. Pd-H in H_2O- and D_2O-based 0.1 M H_2SO_4. The peak positions were determined either as maximum peak value or triple Lorentzian peak fit. SD stands for standard deviation.*

Determination of	Peak position in H_2O	Peak position in D_2O	Δpeak position
Max. value	593.8 ± 6.4 cm^{-1}	589.2 ± 6.6 cm^{-1}	within SD
1^{st} peak	488.0 ± 2.1 cm^{-1}	487.3 ± 1.1 cm^{-1}	within SD
2^{nd} peak	537.9 ± 5.4 cm^{-1}	541.2 ± 2.1 cm^{-1}	within SD
3^{rd} peak	599.2 ± 2.6 cm^{-1}	597.3 ± 1.5 cm^{-1}	within SD

Figure 3.9A-F and Figure 3.7B show contour plots of EC-SERS spectral evolution as a function of time. The images were constructed by plotting the acquired EC-SERS single spectra as a function of time after subtraction of an asymmetric least square background (matlab, asLS_baseline_v1.m, smoothness parameter = 1e2, break iterations if difference is less than 1e6) [Eil03].

Chapter 4

Sulfate adsorption on Au(111)

The following chapter is reproduced/adapted from 'Jonas H. K. Pfisterer, Ulmas E. Zhumaev, William Cheuquepan, Juan M. Feliu, and Katrin F. Domke, "Stark effect or coverage dependence? Disentangling the EC-SEIRAS vibrational shift of sulfate on Au(111)", Journal of Chemical Physics, 2019, 150(4), 041709', with the permission from AIP Publishing [Pfi19c].

In the previous Chapter 3, we have utilized the potential-jump from surface oxidation potentials to the onset of the AuOx electro-reduction in order to monitor the surface reduction with slowed down reaction kinetics. Here, we present an experimental approach, based on these observed slow reduction kinetics and EC-SEIRAS potential-jumps, to differentiate between and quantify potential-induced coverage dependence and field-related Stark effects observed in a sulfate band shift of 93.5 ± 1.5 cm^{-1}/V in electrochemical IR spectra during CV of the showcase sulfate/Au(111) interface. Infrared spectroscopy is a widely employed analytical tool in (electrochemical) surface science as the spectra contain a wealth of information about the interaction of interfacial adsorbates with their environment and is complementary to the EC-SERS study on polycrystalline Au electrodes of the previous Chapter 3. Separating and quantifying individual contributions, for example, of co-adsorbates, the substrate or electric field effects, on the overall spectral response is often non-trivial as the various interactions manifest themselves in similar spectral behavior. In combination with a simple linear model equation used to describe the potential-induced peak shift of the sulfate stretch vibration, we determine the coverage dependence contribution to be 15.6 ± 1.2 cm^{-1}/θ_{SO} and the Stark effect to amount to 75.6 ± 2.7 cm^{-1}/V. Our work provides a novel route to gain fundamental insight into interfacial adsorbate interactions in electrochemical surface science.

4.1 Stark effect or coverage dependence?

Infrared absorption spectroscopy (IRAS) is one of the most commonly employed experimental techniques for the in-situ or operando investigation of (electro)catalytically active interfaces as IR vibrational spectra provide a wealth of information about adsorbate species and their physico-chemical interactions, such as chemical bonding, molecular orientation, or site-selective reactivity [Zae14, Fai18]. While the electrochemical surface-enhanced variant of the technique, EC-SEIRAS, achieves excellent signal-to-noise ratios even from (sub)monolayer adsorbates under potential control of the substrate [Osa01, Rod03a], unambiguous spectral interpretation is often complicated by the joint occurrence of external field- or charge-induced Stark-type effects and the physico-chemical properties intrinsic to the system under study. Disentangling these different effects would be invaluable for an optimal exploitation of EC-SEIRAS data and provide helpful input for improved modeling approaches to enhance our fundamental understanding of (potentio-) dynamic interfacial electrochemical processes.

One prominent example for such unresolved spectral behavior is the drastic upshift by about 60 to 100 cm^{-1}/V of the sulfate/Au(111) ν_{SO} stretch vibration observed as a function of applied potential, E [Ata98, Ede94, Zhu13]. Despite the fact that the sulfate/Au electrochemical system has been studied in great detail [Mag92, Shi99, Wan04], questions about the fundamental nature of the potential-dependent molecule-substrate and molecule-molecule interactions have remained unresolved [Fag90, Pat97, Lam96, Ata96]. Particularly, quantifying the extent to which an (external) Stark effect and/or coverage-dependent sulfate-sulfate (dipole) interactions contribute to the peak shift would provide important insight into the interfacial (re)activity of this important electrochemical model system but has not yet been achieved.

The coverage dependent contribution to the shift, $\Delta\tilde{\nu}(\theta)$, can be ascribed to an increased Coulomb repulsion or dipole-dipole coupling [Hol85] between neighboring sulfate anions as the sulfate surface coverage increases with time and increasing potential until the onset of Au surface oxidation. This enhanced lateral Coulomb repulsion compresses neighboring adsorbed sulfate anions and thereby strengthens the SO molecular bond, resulting in a ν_{SO} band upshift. In contrast, the Stark shift, $\Delta\tilde{\nu}(\phi)$, is based on the surface electric field, ϕ (which is directly related to the applied potential, E) that causes the vibrational energy levels of the adsorbate to shift linearly with $\Delta\phi$ [Lam96, Bis93, Jin13]. Furthermore, the downshift of the Fermi-level of the Au electrode with increasing positive potential relative to the filled anti-bonding states of the sulfate leads to back-donation of electrons from

the anti-bonding states to the Au, thereby strengthening the SO bond and upshifting the ν_{SO} band [Fag90, Pat97, Ata96].

Note that for systems that exhibit a broad potential window with predefined stable adsorbate coverage, determining the Stark effect independently from changes in adsorbate coverage is rather straightforward: for example, Kunimatsu et al. determined the coverage and the Stark effect contributions to the overall ν_{CO} band shift for CO on smooth Au electrodes in alkaline media to be 50 to 60 cm^{-1}/θ_{CO} and about 64 cm^{-1}/V, respectively [Kun86]. The Weaver group varied the CO coverage on Pt(111) by partial CO electrooxidation and found a ν_{CO} peak shift of roughly 10 cm^{-1}/θ_{CO} for varying CO coverages [Leu88]. For the $\Delta\tilde{\nu}(\phi)$ Stark contribution, the same authors observed shifts of 34 to 44 cm^{-1}/V, depending on the CO coverage.

For sulfate adsorption on Au(111), however, the task to pinpoint and disentangle the influence of adsorbate coverage on the overall peak shift is challenging because saturated sulfate coverage is only reached within a narrow potential window. A different experimental approach to the usual CO/metal studies is thus required. Here, we propose a strategy to disentangle the total potential-dependent ν_{SO} band shift of 93.5 ± 1.5 cm^{-1}/V based on EC-SEIRAS potential-jump experiments that allow us to slow down the sulfate adsorption kinetics sufficiently to disentangle coverage from Stark effects, combined with CV. We derive a linear equation that contains both coverage dependence and Stark effect and allows us to extract numerical values to compare with the experimental data. As a result, we quantify the Stark effect to be 75.6 ± 2.7 cm^{-1}/V, while the coverage increase accounts for 15.6 ± 1.2 cm^{-1}/θ_{SO} of the total band shift. This detailed insight into the relationship between sulfate surface coverage, macroscopic electric field, and EC-SEIRAS peak position demonstrates the great potential that our approach entails to enhance our fundamental understanding of the interplay of adsorbates at electrified solid-liquid interfaces.

4.2 Materials and experimental details

The EC-SEIRAS samples were 25 nm thick Au thin films (99.999%, Kurt J. Lesker Ltd.) that were thermally evaporated on one of the faces of a low oxygen-content Si 60° prism (Pastec Ltd., Japan). Thermal evaporation was performed at a base pressure of ca. 10^{-6} Torr in the vacuum chamber of a PVD75 coating system (Kurt J. Lesker Ltd.). A quartz crystal microbalance was utilized to control both the deposition rate (0.06 Å/s) and the

thickness of the Au film. After sample mounting, the Au thin film electrodes were cleaned in the spectro-electrochemical cell by applying a few CV cycles up to the onset of Au surface oxidation in 0.1 M H_2SO_4 electrolyte.

The utilized EC-SEIRAS setup in an ATR configuration is specified in Section 2.5.4. Reference spectra were obtained at the reference potential of 0.1 V vs. RHE, which is a potential region where specific anion adsorption can be neglected. Therefore, the gain or loss of species corresponds to positive and negative EC-SEIRAS bands with respect to this chosen reference potential, respectively. The average value of the extracted ν_{SO} peak area of 20 spectra recorded in the potential range between 1.15 and 1.3 V vs. RHE, in which the peak area reaches saturation, is utilized to normalize the ν_{SO} peak area. The saturated sulfate layer is known to cover approximately 20% of the Au(111) surface [Ede94] and is denoted as the saturation coverage, θ_{SO}, in the following. For all EC-SEIRAS measurements, spectra with a resolution of 4 cm^{-1} were obtained by recording interferograms with an acquisition time of 350 ms. 90 EC-SEIRA spectra recorded at the reference potential of 0.1 V vs. RHE directly before each measurement were averaged and served as the reference spectrum. A Gaussian line shape and linear baseline subtraction were employed for the fitting of the spectral data performed in matlab.

All glassware and Teflon cell parts were thoroughly cleaned by HNO_3 boiling with subsequent cycles of rinsing and boiling in ultrapure water (18.2 MΩ cm, max. TOC 50 ppb, Elga Vivendi). A trapped hydrogen electrode (RHE) functioned as RE and consisted of a Pt wire with an H_2 reservoir. The RHE reference electrode was always prepared freshly directly before the experiments. The CE consisted of a Au wire plate. Aqueous electrolyte of 0.1 M H_2SO_4 was prepared from H_2SO_4 solution (96%, Merck Suprapur) and ultrapure water. Ar gas (N50, Air Liquide) was utilized to degas the working electrolyte and to blanket the solution during the experiments. The Au thin film stability was regularly examined by checking for changes of the recorded CVs, macroscopic mutations of the Au film and sudden spectral changes in the slope at higher wavenumbers. The Au thin films revealed the order/disorder transition peak at ca. 1.1 V vs. RHE proving to be (quasi) Au(111)-like. The Au thin films are therefore addressed as Au(111) in the following.

4.3 Continuous scan experiments

Figure 4.1 shows representative CVs of the Au(111) electrode in 0.1 M H_2SO_4. The overall shape of the CVs and the integrated charge values for the sulfate adsorption and Au

surface oxidation correspond well with values reported in the literature. The extracted charge from the double layer region and the double layer corrected charge during oxidation account to 133.6 µC cm^{-2} and 1273.2 µC cm^{-2}, respectively, suggesting a roughness factor of the Au(111) electrode of roughly two [Her95].

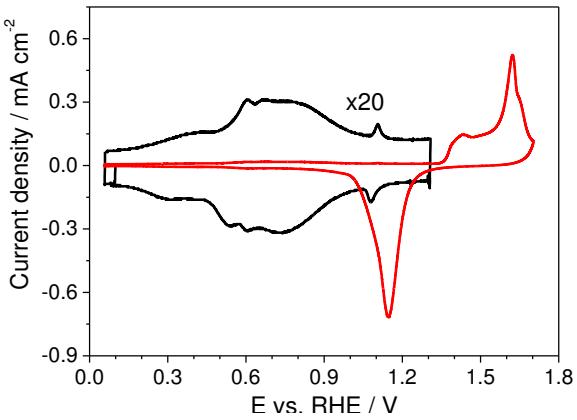

Figure 4.1. *CVs of the Au(111)-25nm electrode in 0.1 M H_2SO_4 (scan rate = 50 mV/s) in the double layer region (black curve) and up to full surface oxidation with an upper potential limit of 1.7 V vs. RHE (red curve).*

Figure 4.2A shows an example EC-SEIRA spectrum recorded at 0.91 V vs. RHE during CV. The sulfate peak, ν_{SO}, around 1200 cm^{-1}, as well as the negative-going OH stretching (∼3500 cm^{-1}) and HOH bending (∼1650 cm^{-1}) modes are visible [Ata98]. Figure 4.2B

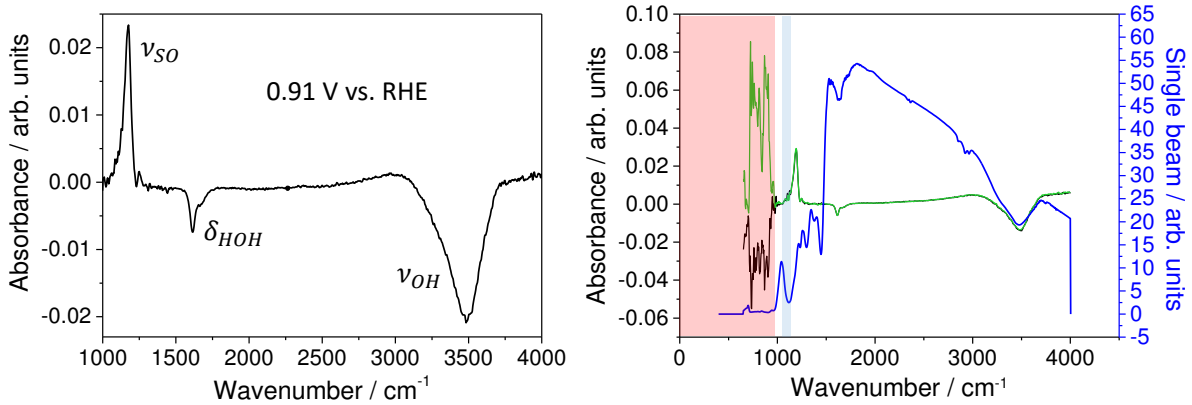

Figure 4.2. *Example EC-SEIRA spectra during CV. (A) EC-SEIRA spectrum recorded at 0.91 V vs. RHE during CV. (B) Full EC-SEIRA spectra in absorbance units, $\mathcal{A}$, defined as $\mathcal{A}$ = -log(I/I_{ref}), at sufficiently positive potentials to adsorb sulfate (green and black curves). The blue curve is a single beam spectrum at the reference potential of 0.1 V vs. RHE, which is obtained after the Fourier Transform of the (recorded) interferogram.*

shows example EC-SEIRA spectra including a noisy spectral region below 1000 cm^{-1} (red

region). The region around 1100 cm^{-1} (blue region) also exhibits spectral noise fluctuations. This noise originates from strongly decreased transmittance of the Si-prism (Figure 4.2B blue spectrum). As the absorbance is plotted in logarithmic form as -log(I/I_{ref}) (Figure 4.2B green and black spectra), small changes in the single beam spectra close to zero are strongly amplified leading to the noisy spectral regions.

Figure 4.3A shows the normalized peak area of the sulfate band, ν_{SO}, at around 1200 cm^{-1} as a function of applied potential for the up-scan to more positive potentials (black) and down-scan to more negative potentials (green) as well as the simultaneously acquired CV (gray). The ν_{SO} peak starts to grow at around 0.6 V vs. RHE and saturates between

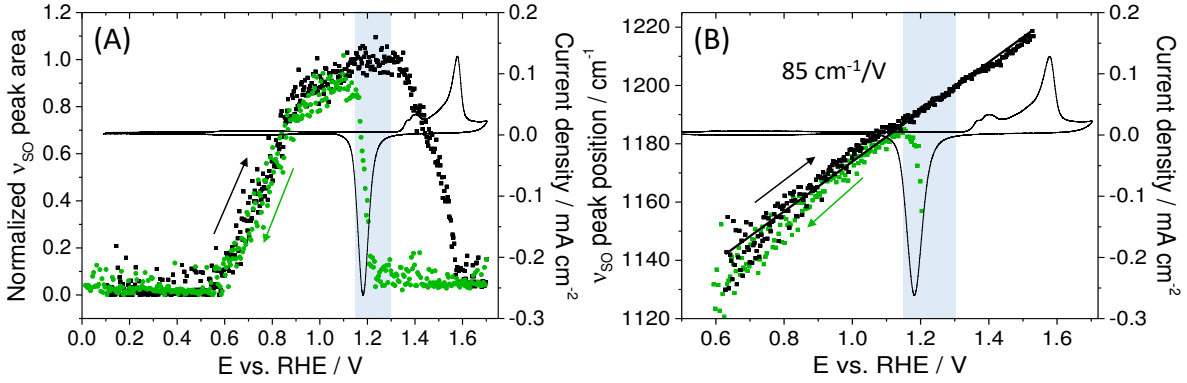

Figure 4.3. *Continuous EC-SEIRAS scan experiments. (A) Normalized ν_{SO} peak area plotted as a function of potential and (B) ν_{SO} peak position plotted as a function of potential during CV in upward (to more positive potentials, black) and downward (to more negative potentials, green) scan direction at 10 mV/s scan rate (electrolyte = 0.1 M H_2SO_4); simultaneously recorded CV (gray). The solid black line in (B) is a linear fit to the data. The blue highlighted region indicates the potential region of approximate saturated sulfate coverage.*

1.15 and 1.3 V vs. RHE. Above 1.35 V vs. RHE, coinciding with the onset of Au surface oxidation, the ν_{SO} peak decreases and vanishes at around 1.55 V vs. RHE. During the potential down-scan to more negative potentials, the ν_{SO} peak area starts to increase at approximately 1.2 V vs. RHE. The hysteresis between the peak appearance in upward and downward scan directions has been observed previously [Shi94] and can be explained by the fact that before sulfate adsorption, AuOx needs to be reduced to free Au sites, consequently delaying sulfate readsorption in the downward scan direction (sweep to more negative potentials). Note that we do not observe any spectral features that can be associated with sulfate adsorption on AuOx. We speculate that this absence of additional spectral bands indicates the occurrence of a second point of zero charge (pzc) for sulfate adsorption on AuOx at a potential of around 1.35 V vs. RHE, similar to what has been

suggested by the Eikerling group for Pt (oxide) [Hua16, Hua18]. The peak area reaches its maximum at ∼1.1 V vs. RHE before dropping continuously until reaching noise level at ∼0.6 V vs. RHE. As the recorded EC-SEIRAS peak intensities exhibit the same potential-dependence as chronocoulometric and radiotracer data that have been previously used to assess sulfate surface coverages (Ref. [Shi94] and Figure S3 in supplementary material of Ref. [Pfi19c]), we can employ the peak area as a direct measure for the sulfate surface coverage. In agreement with the literature, effects of potential-dependent surface enhancement [Zap16] or molecular reorientation [Ata98] on the band intensities can be excluded.

In Figure 4.3B, the ν_{SO} peak position is plotted as a function of applied potential for the scan to more positive potentials (black) and more negative potentials (green). The complete upward scan and the downward scan from ∼1.1 V vs. RHE (after a sharp increase in peak position between 1.1 and 1.2 V vs. RHE due to the fast recovery of the sulfate saturation coverage) exhibit similar linear behavior and can be fitted with a slope of ∼93.5 ± 1.5 cm^{-1}/V. This potential-dependent shift, $\Delta\tilde{\nu}(E)$, is close to the ones previously reported by other groups of 60 to 100 cm^{-1}/V [Ata98, Ede94, Zhu13]. It contains contributions from both the field-induced Stark effect and coverage-dependent adsorbate-adsorbate dipole interactions that cannot be easily disentangled from the EC-SEIRAS data of the continuous scan experiment. If one assumes that complete saturation coverage is reached in the potential range between 1.15 and 1.3 V vs. RHE (blue highlighted region in Figure 4.3), one can fit the corresponding region in Figure 4.3B separately (Figure 4.4). In principle, the so obtained slope of 75.6 ± 2.7 cm^{-1}/V should depict the pure Stark shift contribution, $\Delta\tilde{\nu}(\phi)$, to the total shift. As the number of data points in this region is rather limited and the assumption of full coverage may not be perfectly valid given the large scattering of data points in this region, in the following, we suggest an additional, more precise experimental approach to separate the two effects.

4.4 EC-SEIRAS potential-jump experiments

To obtain the pure coverage dependent contribution, $\Delta\tilde{\nu}(\theta)$, to the total potential-induced shift, we performed potential-jump experiments. The underlying idea of this approach is based on two observations: (i) The sulfate surface coverage starts to decrease with the onset of Au oxidation and recovers when the AuOx is reduced as sulfate ions do not adsorb on oxidized Au(111) but only on the pure Au. (ii) The reduction of AuOx around the reduction onset potential of ∼1.2 V vs. RHE is much slower, i.e. in the order of a few

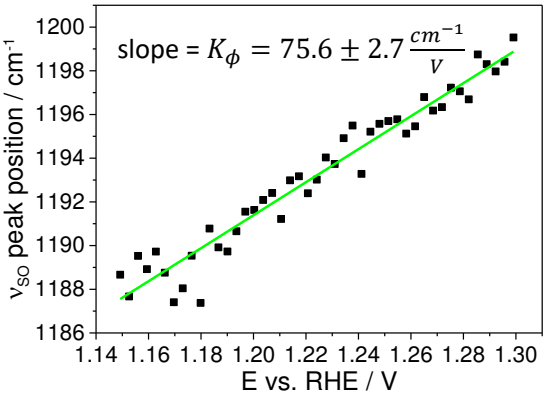

Figure 4.4. *Linear fitting of the ν_{SO} peak position as a function of potential for the potential range from 1.15 to 1.3 V vs. RHE, i.e. the region in which sulfate coverage is approximately constant, returns a slope of $K_\phi = 75.6 \pm 2.7 \frac{cm^{-1}}{V}$.*

seconds, than the kinetics of sulfate adsorption on Au. We can thus slowly reduce the oxidized Au surface at a constant potential of 1.2 V vs. RHE to create a free Au surface to slow down the sulfate coverage increase. This strategy allows us to monitor the effect of the coverage change during sulfate adsorption at a fixed (surface) potential, i.e. with a 'fixed' Fermi level, in this way disentangling the contributions of coverage dependence and Stark effect to the total potential-dependent band shift.

The proposed strategy was implemented by applying a potential-jump sequence of 0.1 $\rightarrow$ 0.75 $\rightarrow$ 1.2 $\rightarrow$ 1.7 $\rightarrow$ 1.2 $\rightarrow$ 0.75 V vs. RHE to the Au electrode while recording EC-SEIRA spectra (Figure 4.5). Each potential was held for 32 to 64 s before jumping to the next potential value. In Figure 4.5A, representative SEIRA spectra of the applied potential-jumps with an acquisition time of 350 ms are shown. The potential of 0.1 V vs. RHE represents the applied potential for the reference spectra and corresponds to the potential region in which anion adsorption is negligible. At 0.75 and 1.2 V vs. RHE, the sulfate peak around 1200 cm^{-1} is observed, together with the HOH bending and OH stretching modes of water at around 1600 and 3500 cm^{-1}, respectively [Ata98]. The SEIRA spectra are stable, even after oxidation of the Au(111) thin film (cf. dark vs. light colored curves), in particular in the region of interest for the further discussion from 1000 to 1400 cm^{-1}. The spectra at 1.2 V vs. RHE (green curves) show an increased ν_{SO} peak intensity compared to the ones at 0.75 V vs. RHE (blue curves), due to an increase in sulfate surface coverage. Further, a shift in wavenumber and narrowing in ν_{SO} peak width are apparent. At 1.7 V vs. RHE, the ν_{SO} peak at $\sim$1200 cm^{-1} vanishes as expected due to the formation of AuOx.

Figure 4.5B shows the spectral evolution of the ν_{SO} peak with time at a constant potential of 1.2 V vs. RHE after Au(111) surface oxidation. As sulfate adsorbs on the Au surface, not only the ν_{SO} peak area increases but also a shift in ν_{SO} peak position to higher wavenumbers is observed. Figure 4.6A shows the normalized ν_{SO} peak area (black

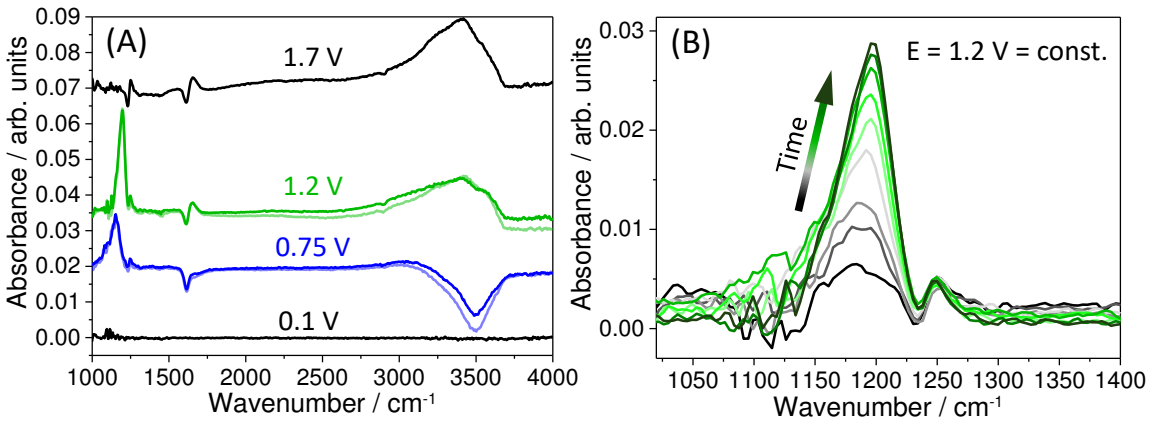

Figure 4.5. *(A) Representative EC-SEIRA spectra recorded during the potential-jump experiments, in which the potential is stepwise altered. Light blue and green colored curves correspond to the upward steps, while thick colors correspond to the downward steps after surface oxidation at 1.7 V vs. RHE. (B) Spectral evolution of the ν_{SO} peak as a function of time at a constant potential of 1.2 V vs. RHE after surface oxidation at 1.7 V vs. RHE. The arrow indicates the color code for the time line (Δt = 43 s from black to dark green).*

data points) and the respective potential steps (blue line) as a function of time for an example data set. The regions highlighted in light blue (upward jumps of 0.1 $\rightarrow$ 0.75 $\rightarrow$ 1.2 V vs. RHE) show an immediate rise in the ν_{SO} peak area due to the fast adsorption of sulfate to Au(111). The light red region (downward jump of 1.7 $\rightarrow$ 1.2 V vs. RHE) shows a slow rise of the ν_{SO} peak area as the AuOx formed at 1.7 V vs. RHE has to be reduced before sulfate adsorption can proceed, in this way providing a sufficient number of data points for analysis. As sulfate adsorption on Au(111) proceeds, a shift in ν_{SO} peak position to higher wavenumbers from about 1173 to 1191 cm^{-1} is observed until θ_{SO} is reached (Figure 4.6B, black data points). Figure 4.6B also shows the simultaneously recorded current versus time trace (blue line) recorded after stepping the potential from 1.7 to 1.2 V vs. RHE. The integration of the current curve gives a total charge of 1.45 mC/cm^2, which is in good agreement with the above-obtained values from CV. The current decays exponentially within the first couple of seconds due to the onset of AuOx reduction that is followed by a slower decay over ~15 s. Note that the sulfate ν_{SO} peak in the potential-jump EC-SEIRA spectra is only observed after the first fast current decay.

In Figure 4.7, we plot the ν_{SO} peak positions vs. the respective normalized peak areas

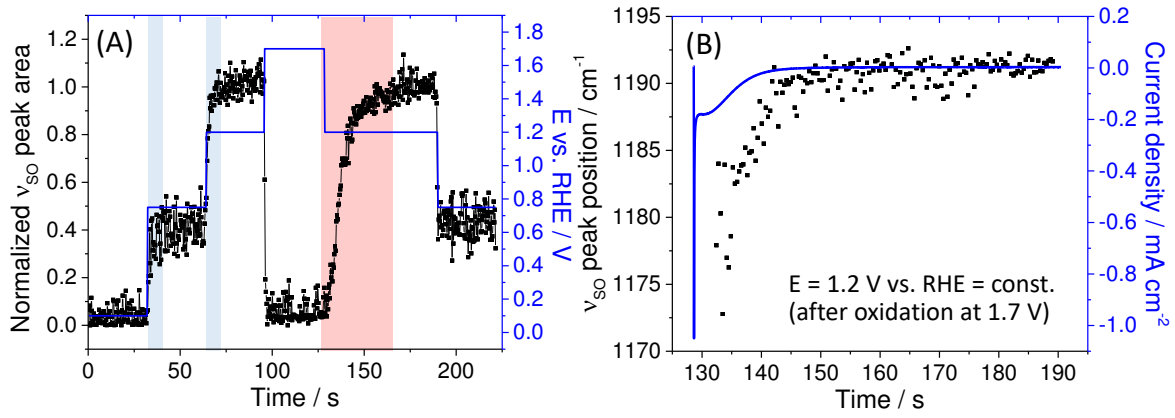

Figure 4.6. *Potential-jump EC-SEIRAS experiments. (A) Normalized ν_{SO} peak area (black) and applied potentials (blue) plotted as a function of time. (B) ν_{SO} peak position (black) and current trace (blue) as a function of time at a fixed potential of 1.2 V vs. RHE after prior surface oxidation at 1.7 V vs. RHE (electrolyte = 0.1 M H_2SO_4). Spectral (data point) acquisition time is 350 ms per spectrum.*

to summarize the results from potential-jump (black) and continuous scan (gray) experiments as displayed in Figures 4.3 and 4.6. The data from the potential-jump experiments show a linear increase in peak position with increasing peak area. As the jump experiments are performed at a fixed potential, the Stark effect contribution must be assumed to be constant throughout the investigated time window for all surface coverages (i.e. peak areas) until sulfate saturation coverage, θ_{SO}. The potential drop across the bare gold-electrolyte interface is set immediately, as suggested by the immediate rise in θ_{SO} peak area prior to oxidation (Figure 4.6A, regions highlighted in blue). From the slopes of three independent potential-jump experiments (Figure 4.8), we quantify the (average) pure coverage-dependent peak shift (i.e. the peak shift due to Coulomb repulsion and dipole-dipole interactions between the molecules within the surface adlayer), $\Delta\tilde{\nu}(\theta)$, to be 15.6 $\pm$ 1.2 cm$^{-1}/\theta_{SO}$. The average peak positions reached at θ_{SO} of 1191 cm^{-1} converge at a potential of E = 1.2 V vs. RHE (right y-axis, with the correlation between peak position and applied potential taken from Figure 4.3) as expected.

On the other hand, the collected continuous scan data points (gray) show a peak position upshift in potential regions where the sulfate coverage increases (at potentials between 0.5 and 1.3 V vs. RHE, as indicated on the right y-axis) as well as for potential regions where the sulfate coverage decreases (at potentials between 1.3 and 1.55 V vs. RHE), amounting to a total shift of 93.5 $\pm$ 1.5 cm^{-1}/V as stated above. The nonlinear trace confirms that the total EC-SEIRAS peak shift observed during CV cannot be solely explained

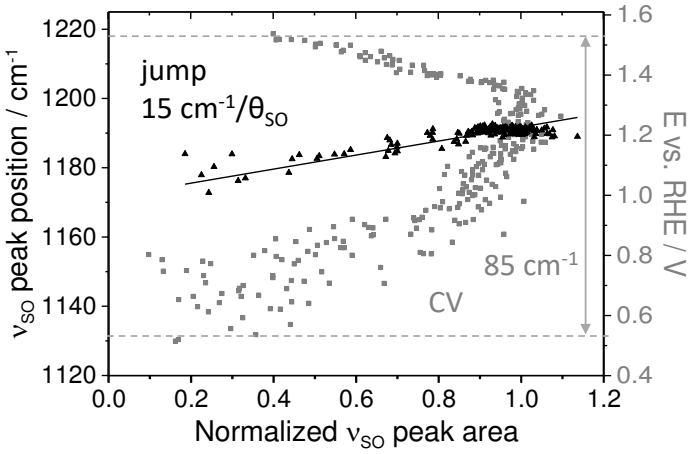

Figure 4.7. *Peak position vs. peak area plot for data points obtained from potential-jump (black) and continuous-scan CV (gray) EC-SEIRAS experiments described in Figures 4.3 and 4.6. The right y-axis notes the respective potentials during CV EC-SEIRAS.*

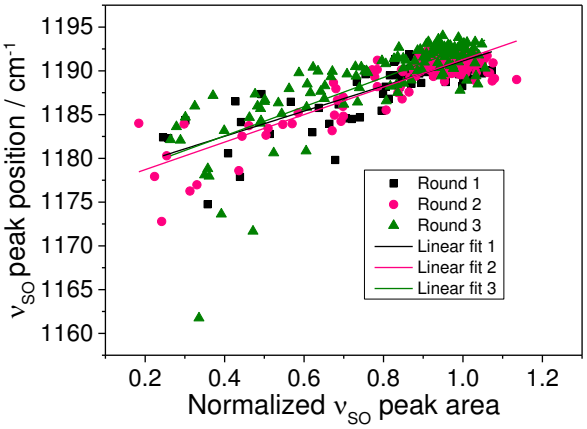

Figure 4.8. *Analysis of the potential-jump experiments. The ν_{SO} peak position is plotted as a function of normalized ν_{SO} peak area. Lines are linear fits to the individual data sets. The reported value of* 15.6 ± 1.2 *cm^{-1}/θ_{SO} (Table 4.1) represents the average value of the three data sets.*

by potential-induced sulfate coverage change. Note that for lack of spectral evidence, we neglect possible (dipole) interactions between AuOx and adsorbed sulfate anions at potentials between 1.3 and 1.55 V vs. RHE.

4.5 Modeling of the ν_{SO} peak shift

Figures 4.3B and 4.7 suggest, to a good first approximation, a linear dependence of the sulfate peak position on the applied potential and on the sulfate coverage, respectively.

Therefore, the sulfate peak position, $\tilde{\nu}_{SO}$, has to depend linearly on both the surface potential, ϕ (which is directly related to the applied potential E), and on the sulfate surface coverage (which implicitly depends on ϕ and on time, t), $\theta(\phi, t)$, and can be expressed by the following equation:

$$\tilde{\nu}_{SO}(\phi, \theta) = K_{\phi}(\phi - \phi_0) + K_{\theta}\theta + \tilde{\nu}_0\,, \tag{4.1}$$

where K_{ϕ} is the slope-constant associated with the Stark effect and K_{θ} is the slope-constant associated with the sulfate surface coverage, and $\tilde{\nu_0}$ is the (hypothetical) vibrational SO stretch frequency of an adsorbed, isolated sulfate molecule (which in earlier studies has been denoted as singleton [Hol85]) at ϕ_0, the potential at which sulfate adsorption starts. From Figure 4.3B, we can extract ϕ_0 to be 0.56 V and $\tilde{\nu_0}$ to be 1136 cm^{-1}. It is interesting to note that while there is a sulfate band observed at potentials lower than those in which the linear relation is observed in Figure 4.3B, the linear extrapolation of the peak position leads to a value so close to that from the differential capacity in the absence of any specific adsorption, i.e. to the pzc of Au(111) [Kol86, Álv00].

In the following, we test Equation 4.1 for consistency with the experimental results: Can the coverage dependence be decoupled from all other potential-dependent effects in this particular form? We are particularly interested in the comparison of K_{θ} extracted from CV and jump experiments, respectively, as additional verification of the proposed jump approach. For the CV EC-SEIRAS data (varying the (surface) potential ϕ and θ), the total derivative in ϕ of Equation 4.1 can be determined as

$$\frac{d\tilde{\nu}}{d\phi} = \frac{\partial\tilde{\nu}}{\partial\phi}\cdot\frac{d\phi}{d\phi} + \frac{\partial\tilde{\nu}}{\partial\theta}\cdot\frac{d\theta}{d\phi} = K_{\phi} + K_{\theta}\cdot\frac{d\theta}{d\phi}\,. \tag{4.2}$$

The analysis of derivatives is convenient as the explicit function of $\theta(\phi, t)$ is unknown.

Within this framework, let us consider the three limiting cases:

(i) If θ does not change, $\frac{d\theta}{d\phi} = 0$, Equation 4.2 can be simplified to $\frac{d\tilde{\nu}}{d\phi} = K_{\phi}$. To determine the constant K_{ϕ}, we identify the potential range in which θ is approximately at saturation, i.e. $\frac{d\theta}{d\phi} \approx 0$ (Figure 4.3). As already briefly described above, within this potential range of 1.15 to 1.3 V vs. RHE, a linear fit of the ν_{SO} peak position as a function of potential reveals a slope $\frac{d\tilde{\nu}}{d\phi} = K_{\phi}$ of 75.6 ± 2.7 cm^{-1}/V.

(ii) For $\frac{d\theta}{d\phi} > 0$, a positive slope is found in the potential range from 0.63 to 0.95 V vs. RHE (Figure 4.3A) that in a first approximation can be viewed as linear, i.e.

$\frac{d\tilde{\nu}}{d\phi} = const.$ From Figure 4.3B, a linear fit of the ν_{SO} peak position as a function of potential in the range from 0.63 to 0.95 V vs. RHE returns:

$$\frac{d\tilde{\nu}}{d\phi} = K_\phi + K_\theta \cdot \frac{d\theta}{d\phi} = 105.5 \pm 5.1 \frac{cm^{-1}}{V} \,. \tag{4.3}$$

Solving for K_θ leads to the following expression:

$$K_\theta = \left(105.5 \frac{cm^{-1}}{V} - K_\phi \right) \cdot \frac{d\phi}{d\theta} \,. \tag{4.4}$$

From Figure 4.3A, $\frac{d\theta}{d\phi}$ can be determined within the potential range from 0.63 to 0.95 V vs. RHE with another linear fit and amounts to $2.43 \pm 0.07\ \theta_{SO}$/V. The reciprocal, $\frac{d\phi}{d\theta}$, is 0.41 ± 0.01 V/θ_{SO}. Inserting K_ϕ and $\frac{d\phi}{d\theta}$ in Equation 4.4, K_θ amounts to 12.3 $\pm$ 3.5 cm^{-1}/θ_{SO} (see Section 4.7 for error propagation). This extracted value of K_θ matches sufficiently the corresponding value extracted from the potential-jump experiments (15.6 ± 1.2 cm^{-1}/θ_{SO}) and confirms the validity of the proposed linear Equation 4.2.

(iii) For $\frac{d\theta}{d\phi} < 0$, i.e. in the potential range from 1.3 to 1.53 V vs. RHE in Figure 4.3A, a similar analysis as for case (ii) returns an error-prone K_θ of 0.04 ± 1.7 cm^{-1}/θ_{SO} (see Section 4.7 for details). The analysis is jeopardized by the fact that Au(111) oxidation starts first at defect sites before it proceeds to (111)-terrace sites, leading to spatially inhomogeneous sulfate desorption that cannot be adequately described with a simple linear model.

According to Equation 4.2, also the total derivative in θ can be further determined as:

$$\frac{d\tilde{\nu}}{d\theta} = \frac{\partial\tilde{\nu}}{\partial\phi} \cdot \frac{d\phi}{d\theta} + \frac{\partial\tilde{\nu}}{\partial\theta} \cdot \frac{d\theta}{d\theta} = K_\phi \cdot \frac{d\phi}{d\theta} + K_\theta \,. \tag{4.5}$$

For the potential-jump experiments (varying θ, constant ϕ), Equation 4.5 simplifies to $\frac{\partial\tilde{\nu}}{\partial\theta} = K_\theta$. This notation suggests a linear trend for $\tilde{\nu}(\phi = const., \theta)$ which is indeed observed experimentally (Figure 4.7). From the potential-jump experiments, K_θ amounts to 15.6 ± 1.2 cm^{-1}/θ_{SO}, which, as already pointed out above, matches well the K_θ value of 12.3 ± 3.5 cm^{-1}/θ_{SO} extracted from Equation 4.2 using the CV EC-SEIRAS data. As it captures all experimental observations adequately, Equation 4.1 can be evaluated as an effective descriptor for decoupling the sulfate coverage dependence from the Stark effect contributions to the overall observed potential-dependent peak shift. The individual values for the peak shift contributions are summarized in Table 4.1.

Table 4.1. *Summary of ν_{SO} peak shift contributions.*

Total potential-dependent shift	$K_E = 93.5 \pm 1.5$ cm$^{-1}/V$
Stark effect contribution	$K_\phi = 75.6 \pm 2.7$ cm$^{-1}/V$
Coverage dependence contribution (potential-jump)	$K_\theta = 15.6 \pm 1.2$ cm$^{-1}/\theta_{SO}$
Coverage dependence contribution (Equation 4.2)	$K_\theta = 12.3 \pm 3.5$ cm$^{-1}/\theta_{SO}$

Note that while this simple linear treatment describes the experimental observations with surprising accuracy and allows for direct quantification of adsorbate-adsorbate and adsorbate-field interactions, a more refined modeling including potential-induced Au oxide or hydroxide formation/dissolution, water displacement and/or reorientation, and the thermodynamic specifics of heterogeneous adsorption sites would be required to increase the accuracy and transferability of the model.

4.6 Conclusions and Outlook

To summarize, we have investigated the potential-induced EC-SEIRAS ν_{SO} band shift of 93.5 ± 1.5 cm^{-1}/V of sulfate/Au(111) in 0.1 M H_2SO_4 in terms of coverage and Stark effect contributions. To assess the pure contribution of sulfate coverage increase to the peak upshift, we have performed potential-jump experiments at a fixed potential, i.e. Stark tuning. Our approach takes advantage of the slow reduction kinetics of AuOx compared to (fast) sulfate adsorption at the reduction onset at around 1.2 V vs. RHE. This experimental strategy allowed us to quantify the coverage contribution to the overall peak shift to be in the order of 15.6 ± 1.2 cm$^{-1}/\theta_{SO}$ by a linear fit of the ν_{SO} peak position versus peak intensity (i.e. sulfate coverage) plot. We have presented and tested a linear model for the peak shift to extract the contribution of the field-induced Stark effect. The derivative analysis returns reasonable estimates for the Stark shift of 75.6 ± 2.7 cm^{-1}/V and for the coverage contribution of about 12.3 ± 3.5 cm$^{-1}/\theta_{SO}$. As such, about 15% of the total shift within the investigated potential range can be attributed to sulfate-sulfate (dipole) interactions, while the remaining 85% are due to field-induced Stark effects.

Evidently, even well-defined electrochemical adsorbate model systems like sulfate/Au(111) that have been studied in great depth for a prolonged time display a high level of complexity in their fundamental potential dependent behavior whose precise nature is still far from being completely understood. As demonstrated here, spectro-electrochemical methods like EC-SEIRAS provide an enormous potential to help elucidate molecular interactions and field-dependent responses of interfacial layers at electrified surfaces by

providing direct quantitative insights about (re)active adsorbates under realistic working conditions that can furthermore be employed as reliable input for advanced simulation approaches.

4.7 Data evaluation and error propagation

Determination of K_θ and error calculation

As described in Section 4.5, K_θ is determined from the CV-SEIRAS data according to Equation 4.4. In the following, additional linear fittings are described, the calculation of K_θ is specified and the propagation of the error is computed.

First, the term $\left(\frac{d\tilde{\nu}}{d\phi} - K_\phi\right)$ had to be determined. For that reason, $\frac{d\tilde{\nu}}{d\phi} = 105.5 \pm 5.1 \frac{cm^{-1}}{V}$ and $K_\phi = 75.6 \pm 2.7 \frac{cm^{-1}}{V}$ were extracted by linear fittings according to Figure 4.9A and 4.4. This leads to:

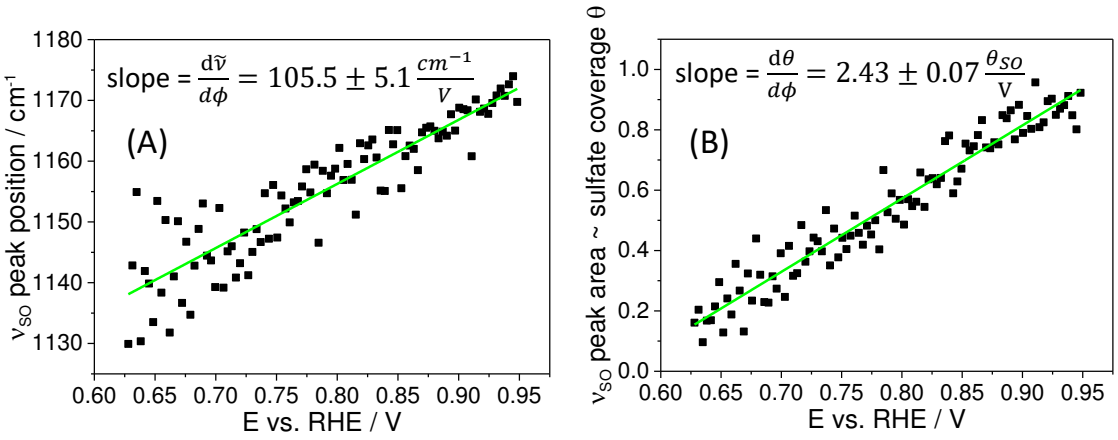

Figure 4.9. *(A) Linear fitting of the ν_{SO} peak position as a function of potential for the potential range from 0.63 to 0.95 V vs. RHE returns a slope of $\frac{d\tilde{\nu}}{d\phi} = 105.5 \pm 5.1 \frac{cm^{-1}}{V}$. (B) Linear fitting of the ν_{SO} peak area as a function of potential in the range of 0.63 to 0.95 V vs. RHE returns a slope of $\frac{d\theta}{d\phi} = 2.43 \pm 0.07 \frac{\theta_{SO}}{V}$.*

$$\left(\frac{d\tilde{\nu}}{d\phi} - K_\phi\right) = 29.9 \frac{cm^{-1}}{V}\,. \tag{4.6}$$

The corresponding error, $\Delta\gamma$, accounts to the following:

$$\Delta\gamma\left(\frac{d\tilde{\nu}}{d\phi} - K_\phi\right) = 5.1 + 2.7 = 7.8 \frac{cm^{-1}}{V}\,. \tag{4.7}$$

In the following, $\frac{d\theta}{d\phi}$ was determined according to Figure 4.9B and the reciprocal value was determined:

$$\frac{d\phi}{d\theta} = \frac{1}{\frac{d\theta}{d\phi}} = 0.41\frac{V}{\theta_{SO}}\,. \tag{4.8}$$

The corresponding error amounts to:

$$\Delta\gamma\left(\frac{d\phi}{d\theta}\right) = \left(\frac{0}{1} + \frac{0.07}{2.43}\right)\cdot 0.41 = 0.01\frac{V}{\theta_{SO}}\,. \tag{4.9}$$

Finally, all above determined values were inserted in Equation 4.4 and K_θ is computed together with the corresponding error:

$$K_\theta = \left(\frac{d\tilde{\nu}}{d\phi} - K_\phi\right)\cdot\frac{d\phi}{d\theta} = 29.9\cdot 0.41 = 12.3\frac{cm^{-1}}{\theta_{SO}}\,, \tag{4.10}$$

$$\Delta\gamma\left(K_\theta\right) = \left(\frac{7.8}{29.9} + \frac{0.01}{0.41}\right)\cdot 12.3 = 3.5\frac{cm^{-1}}{\theta_{SO}}\,. \tag{4.11}$$

Error-prone K_θ extracted for case $\frac{d\nu}{d\phi} < 0$

As before, the term $\left(\frac{d\tilde{\nu}}{d\phi} - K_\phi\right)$ had to be determined. For that reason, $\frac{d\tilde{\nu}}{d\phi} = 75.7\pm 1.5\frac{cm^{-1}}{V}$ and $K_\phi = 75.6\pm 2.7\frac{cm^{-1}}{V}$ were extracted by linear fittings according to Figure 4.10A and Figure 4.4. This leads to:

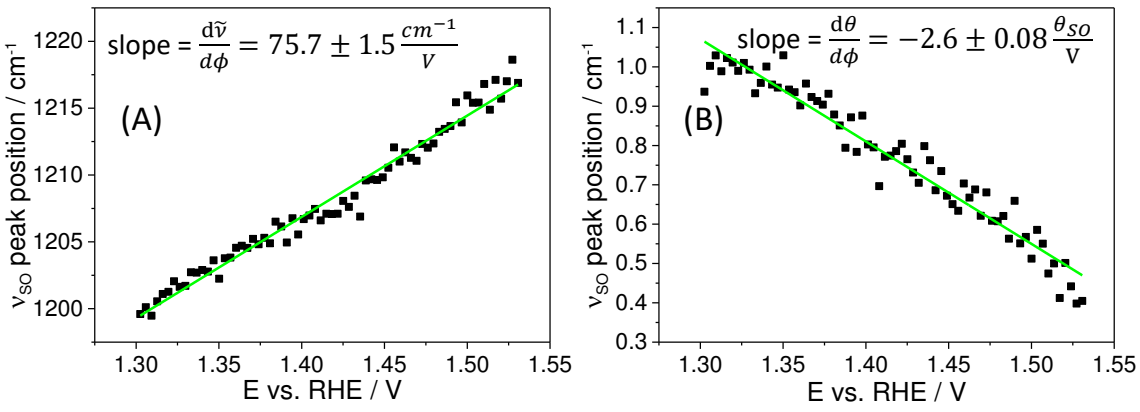

Figure 4.10. *(A) Linear fitting of the ν_{SO} peak position as a function of potential for the potential range from 1.3 to 1.53 V vs. RHE returns a slope of $\frac{d\tilde{\nu}}{d\phi} = 75.7\pm 1.5\frac{cm^{-1}}{V}$. (B) Linear fitting of the ν_{SO} peak area as a function of potential in the range of 1.3 to 1.53 V vs. RHE returns a slope of $\frac{d\theta}{d\phi} = -2.60\pm 0.08\frac{\theta_{SO}}{V}$.*

$$\left(\frac{d\tilde{\nu}}{d\phi} - K_\phi\right) = 0.1\frac{cm^{-1}}{V}\,. \tag{4.12}$$

The corresponding error, $\Delta\gamma$, accounts to the following:

$$\Delta\gamma\left(\frac{d\tilde{\nu}}{d\phi} - K_\phi\right) = 1.5 + 2.7 = 4.2\frac{cm^{-1}}{V}\,. \tag{4.13}$$

In the following, $\frac{d\theta}{d\phi}$ was determined according to Figure 4.10B and the (absolute) reciprocal value was determined:

$$\frac{d\phi}{d\theta} = \frac{1}{\frac{d\theta}{d\phi}} = 0.38\frac{V}{\theta_{SO}}\,. \tag{4.14}$$

The corresponding error amounts to:

$$\Delta\gamma\left(\frac{d\phi}{d\theta}\right) = \left(\frac{0}{1} + \frac{0.08}{2.60}\right)\cdot 0.38 = 0.01\frac{V}{\theta_{SO}}\,. \tag{4.15}$$

Finally, all above determined values were inserted in Equation 4.4 and K_θ is computed together with the corresponding error:

$$K_\theta = \left(\frac{d\tilde{\nu}}{d\phi} - K_\phi\right)\cdot\frac{d\phi}{d\theta} = 0.1\cdot 0.4 = 0.04\frac{cm^{-1}}{\theta_{SO}}\,, \tag{4.16}$$

$$\Delta\gamma\left(K_\theta\right) = \left(\frac{4.2}{0.1} + \frac{0.01}{0.38}\right)\cdot 0.04 = 1.7\frac{cm^{-1}}{\theta_{SO}}\,. \tag{4.17}$$

Chapter 5

Nanoscale EC-TERS mapping of defect reactivity

This chapter has been submitted as and is reproduced/adapted from 'Jonas H. K. Pfisterer, Masoud Baghernejad, Giovanni Giuzio and Katrin F. Domke, "Reactivity mapping of nanoscale defect-chemistry under electro-catalytic reaction conditions", 2019 [Pfi19a]. Please contact the authors directly for further information.

Heterogeneous catalysts often exhibit increased conversion rates at nanoscale protrusions, step edges or material inhomogeneities, as the local electronic landscape of the catalyst surface governs optimal molecular adsorption properties and thus its reactivity. Identification of such nanostructures and the nanoscale understanding of site-specific and potential-dependent reaction mechanisms represent two major challenges in the field of (electro)catalysis. Computer simulations, experiments under UHV conditions or macroscopic operando methodologies have greatly contributed to our current understanding of such structural and chemical material heterogeneities. However, atomistic insights into active-site chemistry under reaction conditions, i.e. in the presence of a liquid phase or flowing charges at higher temperature and pressure, is challenging to be obtained experimentally, because simultaneous acquisition of topographic and chemical information both on the nanometer scale under electrocatalytic reaction conditions is non-trivial.

Here, we demonstrate that EC-TERS, the combination of EC-SPM and near-field Raman spectroscopy, can be employed to map electrochemical water splitting at defect oxidation potentials on Au nanodefects as showcase energy conversion and corrosion reaction with a chemical spatial sensitivity of about 10 nm. We find that the electro-oxidation reactivity of the Au nanodefects is directly correlated to their surface topography and is limited

to an oxide depth of about 3 nm. The local Raman fingerprint indicates the presence of at least two spatially separated AuOx species depending on the nanodefect location. By further correlating electrode-averaged with nanosite information, we quantify a defect coverage of only ca. 4.5% to be responsible for the observed electrocatalytic water splitting reactivity of the Au(111) electrode. Delivering such nanoscale information, we provide the proof-of-concept on how EC-TERS can be utilized in the field of electrocatalysis to identify active defect sites and local chemistry on the nanometer scale.

5.1 Introduction

Nanoscale structural or chemical material heterogeneities, or defects, can markedly define macroscopic material or device properties, like (electro)chemical reactivity and energy conversion [Len19, Fes18], charge or heat management [Gao17, Ulv15] or photonic properties [Fan15]. Controlled defect engineering thus possesses an enormous potential for the strategic design of functional materials – but requires understanding of defect reactivity at the atomistic or molecular level under (non-equilibrium) operating conditions [Mül16, She17].

One prominent field where active defect sites play a pivotal role is heterogeneous (electro)catalysis that lies at the basis of many important chemical or energy conversion reactions. Detailed nanoscale understanding of both nature and location of the catalytically active surface sites is required, but atomistic/nanoscale insights obtained from UHV studies, computer simulations or macroscopic operando experiments are not always easily transferable to nanoscale catalyst behavior under complex reaction conditions at high pressure and/or temperature or in the presence of electrostatic fields [She17, Van17]. Therefore, in order to 'close the catalysis discovery loop', advanced or novel operando experimental and theoretical nano-tools are needed [Han18, Mei18]. EC-STM has recently been employed to identify active surface sites under reaction conditions by comparison of local tunneling current fluctuations above reactive and non-reactive sites [Pfi17, Lia19]. In general, however, EC-STM lacks the chemical specificity that is required to also identify local site-specific and potential-dependent reaction mechanisms, i.e. by monitoring and identifying reaction intermediates locally. EC-SERS offers the necessary surface-molecular chemical specificity [Din16, Don19], but is diffraction limited and thus provides complementary averaged-ensemble information. EC-TERS in principle provides the capabilities to assess nanoscale topographic and chemical spatial information simultaneously and could thus become one of the important operando nano-tools in electrocatalysis [Pfi18].

Employing TERS in air, the Ren group demonstrated that the energetic differences in adsorption behavior of Pd islands on Au(111) edge and terrace sites can be studied by attaching organic molecules to the bimetallic substrate and obtained impressive 3 nm chemical spatial resolution [Zho17]. Prior, Kumar et al. had monitored the photocatalytic induced dimerization of pMA on Ag nanoparticles under ambient conditions and resolved the catalytically active nanoparticles with around 20 nm chemical spatial resolution [Kum15]. Recently, Kumar et al. extended their study of this dimerization reaction on Ag substrates to liquid-drop AFM-based TERS [Kum19]. Using EC-AFM-TERS, the Van Duyne group just very recently managed to map the spatially heterogeneous surface potential distribution on ITO grains with 40 nm resolution [Kan19]. Despite these impressive results, for the field of electrocatalysis and corrosion science, one key ability had to be demonstrated yet: the operando nanoscale chemical imaging of defect reactivity under non-equilibrium electrocatalytic reaction conditions where the reaction products are spatially monitored starting from the plain catalyst surface rather than a pre-assembled organic monolayer.

Here, we map the electrochemical water splitting at defect oxidation potentials of Au nanoscale defects, an important showcase heterogeneous catalytic reaction [DM13] and model oxidative corrosion reaction, with label-free operando EC-TERS nanoscopy [Zen15, Kur15, Mar17b]. Nanoscale understanding of Au defect electro-oxidation is of great importance as it represents the inevitable starting point for further water splitting. We resolve the correlation between heterogeneous surface topography and electrochemical (re)activity under electrochemical operando conditions with a spatial precision of about 10 nm. Correlating the apparent height of defect structures with the EC-TERS AuOx band intensity allows us to quantify the local Au defect oxide layer thickness. The EC-TERS data provide experimental evidence for the existence and nanometer spatial distribution of at least two AuOx species with distinct coordination numbers on the nanodefect sites. With this demonstrated operando EC-TERS nanoscopy approach, a wide range of materials and reaction conditions can potentially be explored in the future to locate and characterize nanoscale active surface sites, for example, in electro- or photoactive materials during operation, during surface corrosion processes, or in biological environments under realistic working conditions. The insight into molecular-scale material (re)activity gained in this way will pave the way for bottom-up defect design and rational tuning of device properties.

5.2 Materials and experimental details

The Au(111) single crystal (MaTecK, 10 mm diameter) was thoroughly flame-annealed under argon (6N, Westfalen) atmosphere before mounting in the Teflon cell. The aqueous electrolyte was 0.1 M H_2SO_4 (96%, Merck, Suprapur) prepared from MilliQ water (Millipore-Q, 18 MΩ cm) or deuterated water (Deuterium oxide, 99.9 atom % D, Sigma-Aldrich). Either a Pt (0.5 mm diameter, Alfa Aesar, Premion, 99.997 % metals basis) or Au wire (0.5 mm diameter, Alfa Aesar, Premion, 99.9985 % metals basis) was utilized as CE and freshly flame-annealed and rinsed with MilliQ water before use. We advice to use a Pt CE to exclude the formation of hydrogen peroxide in the presence of subtle amounts of oxygen in the electrolyte. The RE was a hydrogen-loaded Pd wire (Pd-H), prepared as specified in Section 3.2. All glassware utilized in this study were boiled in 40% HNO_3 (≥65%, Sigma-Aldrich) and subsequently thoroughly rinsed and boiled for three times in MilliQ water.

The employed EC-TERS setup is a home-built device that has been described in Section 2.5. The 600 lines/mm grating was used for the reported experiments. The employed laser power of about 6 to 8 mW power at the focus spot was determined in air and estimated to be lowered to around 1 to 3 mW in electrolyte due to optical aberrations at the glass window [Mar16]. The spectral acquisition time ranged between 1 to 5 s and is specified at the appropriate position. EC-STM images and EC-TERS maps were simultaneously acquired in the scan-to-point mode of PicoView 1.14 software connected to LabSpec 5 software. The data analysis was performed with matlab software.

5.3 EC-TERS detects reaction products

Figure 5.1A shows a typical CV of a Au(111) single crystal surface in 0.1 M H_2SO_4 (cf. Figure 2.9 for bead single crystal), recorded in our EC-TERS spectro-electrochemical cell. The appearance of the sharp order/disorder transition peak at around 1.1 V vs. Pd-H (Figure 5.1B) and the pronounced peak around 1.55 V vs. Pd-H are characteristic for well-defined Au(111) single crystals of high quality. The anodic peak around 1.55 V vs. Pd-H corresponds to the electro-oxidation of Au(111) terraces, while its shoulder extending from roughly 1.48 to 1.32 V vs. Pd-H has been attributed to the oxidation of nanoscale surface defects (Figure 5.1A, green region) [Kol00, Zhu13]. Integration of surface charges from 1.225 to 1.6 V vs. Pd-H (full surface oxidation) corresponds to 690.4 µC/cm^2, which corresponds well to literature values of around 619 µC/cm^2 in 1 M H_2SO_4 [Zhu13]. With an upper integration boundary of 1.45 V vs. Pd-H only 58.7 µC/cm^2 are

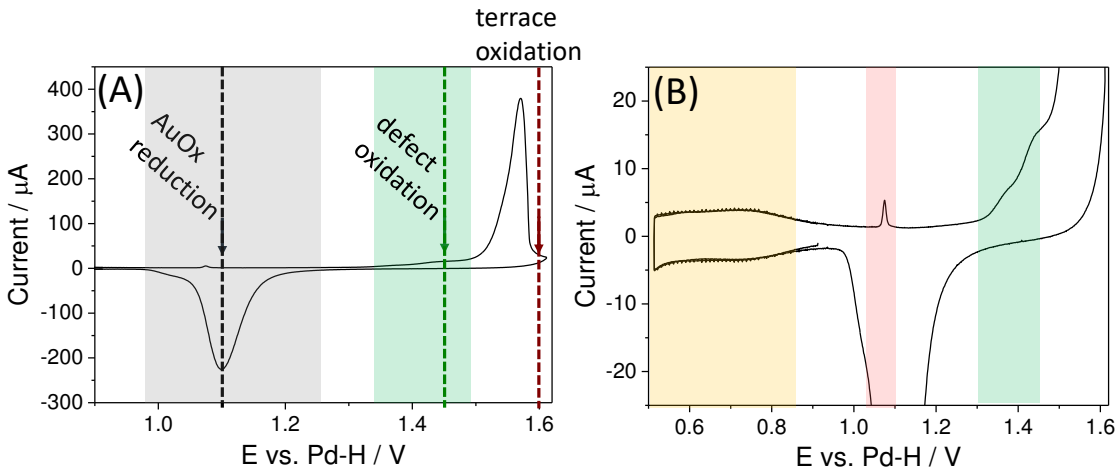

Figure 5.1. *CV of a Au(111) single crystal. (A) CV of a Au(111) electrode in 0.1 M H_2SO_4 (scan rate = 50 mV/s). (B) Zoom-in image of (A). Yellow, red, gray and green shaded areas highlight sulfate adsorption, order/disorder transition, AuOx reduction and defect oxidation regions, respectively.*

detected as only defect structures are oxidized, which is close to ∼63 µC/cm^2 detected by Conway and coworkers [AK86]. When the fully electro-oxidized Au surface is reduced (integration boundaries 1.6 to 0.85 V vs. Pd-H), the determined charge density of -668.2 µC/cm^2 is close to the surface oxidation charge value, as expected.

The essential question to address initially is whether it is at all feasible to detect reaction intermediates/products by EC-TER spectroscopy, as previous studies, so far, have focused their efforts on organic SAMs prepared before transfer to the EC-TERS cell [Zen15, Kur15, Mat16, Mar17b, Che18a, Che18b, Gou18, Yok19, Jia19, Kan19, Hua19]. Figure 5.2A demonstrates that EC-TERS can indeed detect reaction products as a function of the applied electrode potential. Increasing the applied potential from 1.15 to 1.6 V vs. Pd-H, the AuOx stretching mode around 580 cm^{-1} can be clearly detected starting from around 1.45 V vs. Pd-H. At lower potentials (e.g. 1.4 or 1.15 V vs. Pd-H, see Figure 5.2A), no EC-TERS signal of AuOx is detected, while at more positive potentials, the AuOx peak increases in intensity. When the Au-tip is retracted far from the surface (Figure 5.2A blue spectrum), conventional Raman cannot resolve the AuOx stretching band, indicating that it is the plasmonic near-field created by the Au-tip that is responsible for the Raman signal enhancement.

Figure 5.2B shows an EC-TERS spectral time-series recorded at the same position (within the limits of thermal drift of few nm/min as discussed later) on oxidized Au(111) at 1.6

V vs. Pd-H. The spectral acquisition time was 5 s per spectrum. The acquired EC-TER spectra are reproducible and stable over time, even under terrace electro-oxidation conditions at 1.6 V vs. Pd-H.

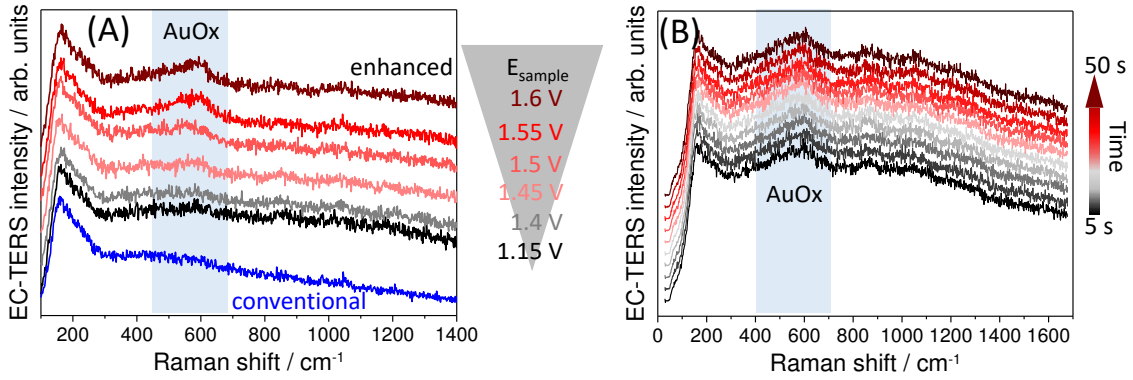

Figure 5.2. *Potential-dependent EC-TER spectra and spectral stability investigation. (A) Potential-dependent EC-TER spectra (black to red) recorded on Au(111) in 0.1 M H_2SO_4. The EC-TER spectra above 1.45 V vs. Pd-H portray a broad peak around 580 cm^{-1} (highlighted blue area), which has been assigned to AuOx [Des86]. The sample potential was continuously altered at a scan rate of 10 mV/s (constant bias at 400 mV, i.e. max. tip potential = 1.2 V vs. Pd-H at 1.6 V vs. Pd-H applied to sample electrode). The blue spectrum is a conventional Raman spectrum recorded with the tip ca. 6 µm retracted from the surface at a sample potential of 1.6 V vs. Pd-H. (B) EC-TER spectra recorded subsequently at the same spot at 1.6 V vs. Pd-H (tip potential = 1.2 V vs. Pd-H, i.e. 400 mV bias voltage). All spectra are y-offset from each other by 200 arb. units for clarity and would otherwise overlap. The colored arrow (black to dark red) represents the spectral time evolution (Δt = 45 s). For (A,B), the acquistion time was 5 s for each spectrum. The i_t setpoint was 1 nA.*

During the experiments, great care has been undertaken to ensure that the Au-tips stay oxide free and that the obtained AuOx signal originates from the electro-oxidation at the Au(111) surface. Figure 5.3 shows two CVs from the Au(111) electrode (blue) and the Au-tip (black) recorded simultaneously with 0 V bias and a scan rate of 100 mV/s. As the Au-tip is in principle a defective Au structure, the oxidation starts around the defect oxidation region above 1.3 V vs. Pd-H, as expected, and exhibits its main oxidation peak around 1.45 V vs. Pd-H. On the other hand, the Au(111) shows its strongest anodic peak around 1.55 V vs. Pd-H corresponding to (111) terrace oxidation with a shoulder extending to the defect oxidation region toward more negative potentials. Importantly, the onset of the reduction of the AuOx at approximately 1.2 V vs. Pd-H (in accordance with our EC-SERS results in Chapter 3) clearly overlap for both the Au(111) electrode and the Au-tip. Maintaining the Au-tip potential at a maximum potential of 1.2 V vs. Pd-H or below

thus ensures that the Au-tip resides in the AuOx reduction region and remains AuOx free.

We have achieved this requirement of AuOx free tips either by applying a constant bias or by keeping the tip potential fixed. For the constant bias case, we have utilized a constant bias of 400 mV or more. For a maximum upper sample potential of 1.6 V vs. Pd-H, this corresponds to 1.2 V vs. Pd-H for the Au-tip (and 400 mV bias). The second approach fixes the Au-tip potential at 1.2 V vs. Pd-H or below, e.g. at 1.0 V vs. Pd-H, assuring that the Au-tip is not oxidized.

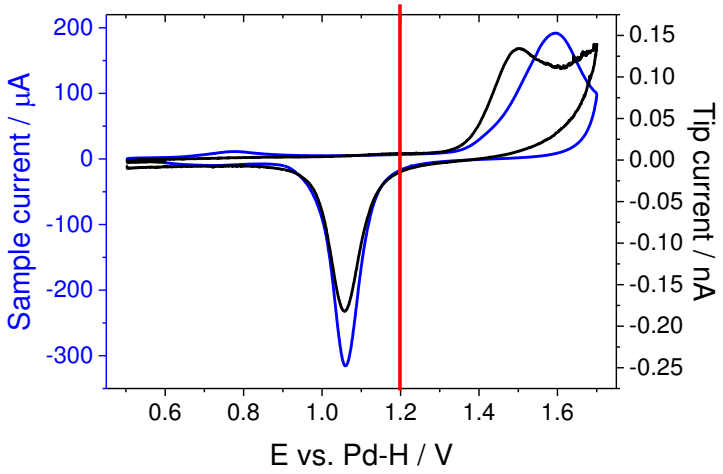

Figure 5.3. *CVs of the Au(111) sample electrode (blue) and the Au-tip (black) in 0.1 M H_2SO_4. The bias voltage is set to 0 V and the CVs were acquired simultaneously with a scan rate of 100 mV/s. The red line indicates the maximum Au-tip potential utilized within this work.*

To further roughly estimate how many AuOx bonds are probed during surface oxidation at 1.6 V vs. Pd-H using EC-TERS, an approximate surface Au_2O_3 structure can be envisioned, shown in Figure 5.4. Note that, due to place-exchange between Au- and O-atoms, the surface structure is expected to be disrupted (in accordance with e.g. Figure 3.10G). The unit cell, marked with a red square, has an area of approximately 0.136 nm^2 (1.87 nm · 0.27 nm) and includes three Au-O bonds. Assuming an approximated spatial chemical resolution of 100 nm^2 (10 nm · 10 nm) using EC-TERS and three layers of Au_2O_3 surface oxide leads to the following: (100 nm^2/0.136 nm^2) · 3 Au-O bonds per unit cell · 3 oxide layers = 6618 Au-O bonds. Therefore, within the conducted EC-TERS experiments at a fully oxidized Au(111) surface, less than 7000 Au-O bonds are approximately probed. We are thus capable to detect smallest amounts of reaction products during an electro-oxidation reaction.

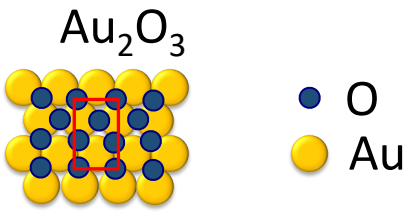

Figure 5.4. *Au_2O_3 surface structure for the estimation of the number of Au-O bonds probed by our EC-TERS experiments at 1.6 V vs. Pd-H, i.e. oxidized Au(111) terraces. Red square indicates unit cell with two Au and three oxygen atoms. The short edge of the unit cell corresponds to the atomic diameter of Au (a = 0.27 nm). The longer edge of the unit cell accounts to a + a/(2 · tan(30°)) = a + (√3/2) a = 1.87 a^2 = 0.136 nm^2.*

Having demonstrated that the in-situ formation of AuOx can be detected by EC-TERS, we can exploit the fact that Au oxidation is initialized at lower potentials compared to Au(111) terrace oxidation (cf. CV in Figure 5.1). Accordingly, only Au defects can be selectively oxidized if potentials of 1.3 to 1.45 V vs. Pd-H are applied to the Au(111) working electrode, while flat Au terraces are retained oxide free. In the following, we show that oxidized Au nano-defects can be mapped by EC-TERS pinpointing local defect reactivity.

5.4 Nanoscale mapping of Au defect oxidation

Figure 5.5 shows a schematic of the EC-TERS mapping experiment. Through electrochemical potential control of the Au(111) electrode, we reversibly switch between water splitting ON and OFF states: at a sample potential, E_{sample}, of 1.45 V vs. Pd-H, water is split to generate AuOx selectively at defect sites while the Au(111) terrace sites remain oxide free (ON). At E_{sample} = 1.1 V vs. Pd-H, the electrode including defects is in its reduced, metallic Au^0 state (OFF). The Au EC-STM probe, or plasmonic Raman enhancer, is scanned across the surface within the diffraction-limited laser far-field focus spot (diameter of ca. 500 nm). We record EC-TER spectra as a function of tip position to generate operando reactivity maps with nanometer spatial chemical resolution, i.e. providing chemical contrast between Au^0 and AuOx as a function of applied potential and surface site. It is important to note that fixing the tip potential to a specific potential value inherently changes the voltage bias when switching the working electrode. We have recently investigated that in general a larger bias will lead to an increased tip-sample dis-

tance and therefore to a decreased TERS intensity in air, but that this effect is negligible for in-liquid experiments [Mar17a]. In any case, when the sample potential is switched from 1.1 to 1.45 V vs. Pd-H (as for the following experiments), the sample bias voltage increases from 100 to 450 mV, which would (if at all) result in a larger tip-sample distance and a lower EC-TERS enhancement for the ON state compared to the OFF state. Under these conditions, we are able to detect AuOx at around 560 to 580 cm^{-1}, and we do not observe any AuOx intensity at 1.1 V vs. Pd-H.

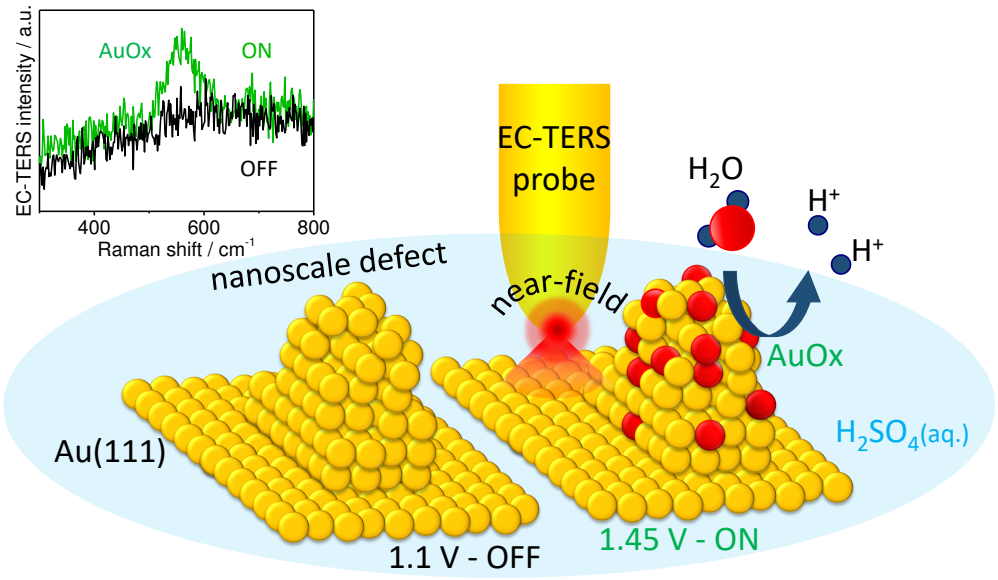

Figure 5.5. *EC-TERS of selective and reversible electrochemical water splitting and Au nanodefect oxidation. Schematic of the EC-TERS operando nanoscopy approach: Water splitting and defect oxidation OFF (left, 1.1 V vs. Pd-H) or ON (1.45 V vs. Pd-H) states can be spatially and chemically resolved by mapping the active site of interest with the EC-TERS probe with about 10 nm spatial precision. Inset: EC-TER spectra for ON (with AuOx peak at ca. 580 cm^{-1}) and OFF states recorded at a defect site.*

The full EC-TER spectra from 100 cm^{-1} (dichroic edge filter cut-off at 156 cm^{-1}) to 1700 cm^{-1} corresponding to the inset in Figure 5.5 are shown in Figure 5.6. When defect-catalyzed water splitting is ON, the AuOx stretching mode around 560 to 580 cm^{-1} is detected [Des86, Shi07]. In contrast, in the OFF state, no Raman peak is visible because all AuOx has been reduced. Small, ill-defined bands can be discerned at ca. 250 cm^{-1} and at ca. 980 cm^{-1} for both ON/OFF states and are tentatively assigned to the 0.1 M sulfuric acid aqueous electrolyte (H_2O and/or $(H)SO_4^{(2)-}$ modes). Note that the spectral background does not change when switching between ON and OFF states, indicating that

the EC-TERS gap resonance is unaffected by the potential switch.

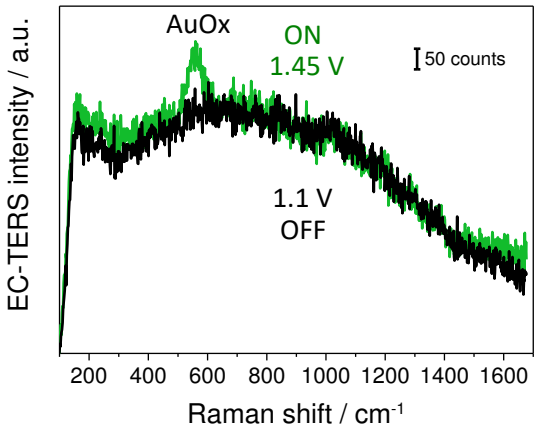

Figure 5.6. *EC-TER spectra for ON and OFF states. EC-TER spectra of Figure 5.5 inset showing the filter cut-off at 156 cm^{-1} and the overall background shape for the ON (1.45 V vs. Pd-H) and OFF (1.1 V vs. Pd-H) states.*

Figure 5.7 shows correlated images of the EC-STM apparent topography (left A,C,E) and EC-TERS AuOx band intensity (right B,D,F) of the electrochemically roughened Au(111) electrode. The EC-TERS images are constructed by linear background subtraction and simple peak area integration. For details about the image contrast determination, see additional materials in Section 5.7 and Figures 5.11, 5.12 and 5.13. Figure 5.7A shows the electrode in the OFF state. During subsequent potential switching between OFF and ON, the operando EC-TERS map (Figure 5.7B) visualizes the reversible water splitting and Au defect oxidation at good spectral contrast. Interestingly, the EC-TERS band intensity varies strongly between different locations during the ON scans, indicating a spatially heterogeneous defect density on the roughened Au(111) surface on the 10 nm length scale.

To visualize the correlation between nanoscale defect structure and reactivity, we map nanodefects of ca. 20 to 40 nm width and 2 to 4 nm height also present on the Au(111) single crystal. The (electronic) structural contours in the EC-STM map (Figure 5.7C) are excellently reproduced in the simultaneously obtained chemical-contrast EC-TERS map (Figure 5.7D), which suggests a chemical spatial resolution of at least our pixel size of 9.4 nm. Surprisingly, the catalytic activity of the topographically rather similar Au structures differs drastically: only two of the nanodefects visible in the EC-STM image exhibit clear AuOx EC-TER signals while the others remain spectrally silent. We attribute these spectral differences to the local variations in work function [Jia98] due to atomic active site heterogeneities [Zam96] that lead to varying degrees of defect reactivity

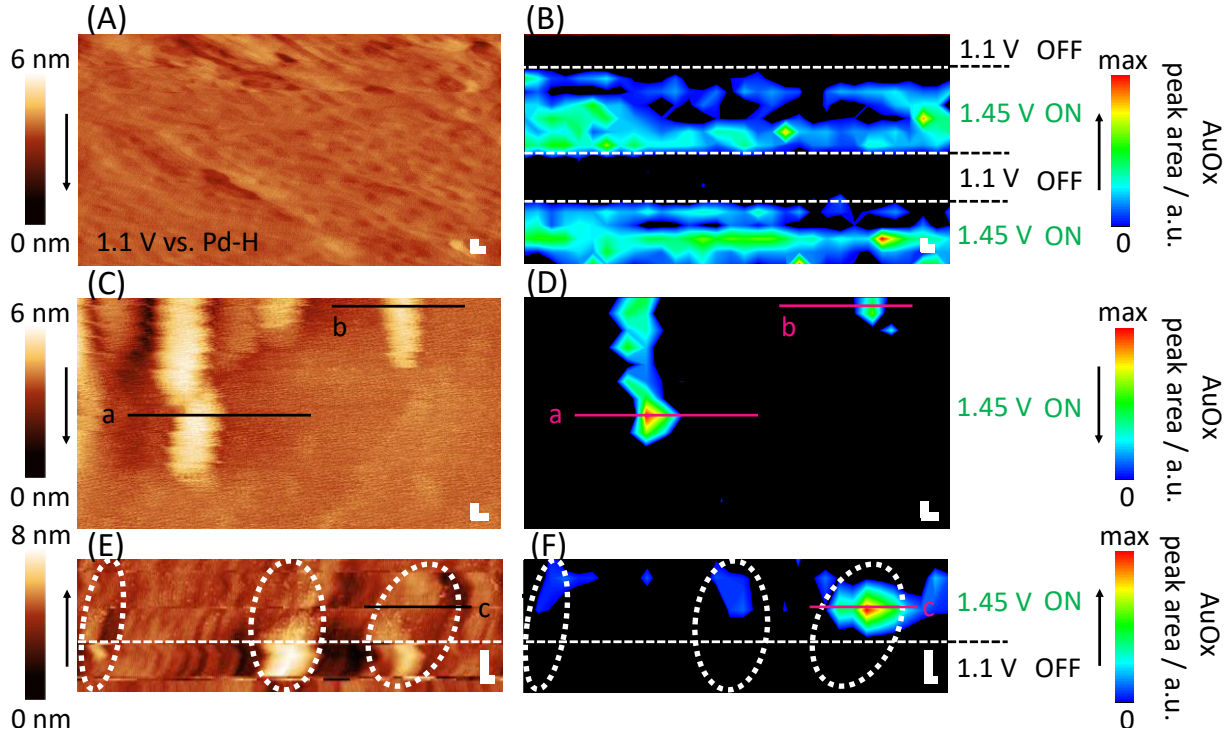

Figure 5.7. *Operando EC-TERS nanoscopy of catalytic defect reactivity. (A,C,E) EC-STM images of Au(111) in 0.1 M H_2SO_4. Scan speed = 1 line/s. (B,D,F) Corresponding EC-TERS maps reconstructed from the AuOx band intensity. Pixel size = 9.4 nm, 3 s (B,F) or 1 s (D) spectral acquisition time/pixel. (A-F) Tunneling current (i_t) = 1 nA, E_{tip} = 1.0 V vs. Pd-H, E_{sample} as indicated; scale bars = 10 nm. Black arrows indicate scan directions. Dotted white lines are guides to the eye. Solid black and pink lines are line profiles analyzed in Figure 5.8.*

directly visualized by EC-TERS mapping.

Figures 5.7E,F demonstrate the full operando nanoscopy capability of EC-TERS where we image the nanodefect chemical behavior while switching from OFF (bottom) to ON (top) states during the scan. In the OFF state, the EC-STM image indicates three distinctive structures of ca. 25 to 50 nm width and 2 to 4 nm height (Figure 5.7E, white dotted lines); as expected, the EC-TERS maps show no AuOx formation, neither at the nanodefects nor on the Au(111) terrace sites (Figure 5.7F). When defect oxidation is initiated, the EC-STM noise level increases, similarly to what has been previously reported for hydrogen evolution on Pt [Pfi17]. The simultaneously recorded EC-TER spectra exhibit the strongest AuOx peak intensities at the nanodefects. The flat Au region remains largely AuOx free, i.e. it does not exhibit significant water splitting reactivity.

Furthermore, our approach allows us to correlate the apparent structure and chemical reactivity of the nanodefects by investigating the EC-STM and EC-TERS line profiles (solid

lines marked in Figure 5.7). The AuOx peak intensity (after background correction to exclude possible near-field artefacts) uniformly follows the changes in the EC-STM apparent height profiles (Figure 5.8A to C and Figure 5.14). The apparent height of the defect steps is in the order of 0.5 nm, or of multiples of 0.5 nm, which corresponds excellently to the height of a monolayer Au_2O_3 of 0.47 to 0.5 nm as suggested to be formed during complete oxidation of a Au monolayer and subsequent Au-O place-exchange [TF97, Oes83]. Changes in apparent topography are accompanied by changes in EC-TERS band intensity within typically one pixel, an effect particularly evident for the broad stepped structure profiled in Figure 5.8C. These results underline that we resolve chemical heterogeneities with a spatial sensitivity of about 10 nm. Plotting the AuOx Δpeak area vs. topographic

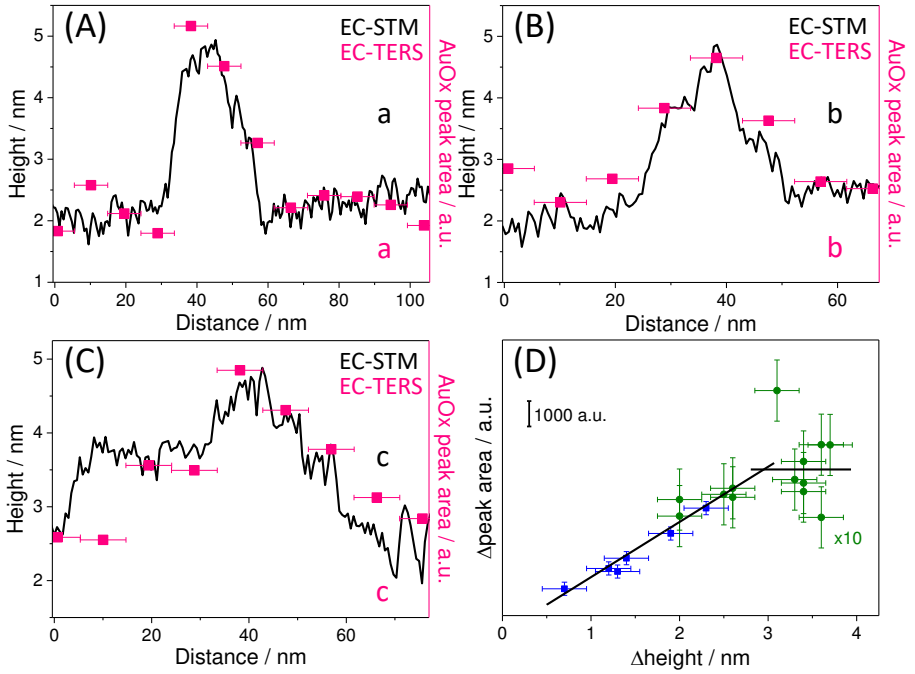

Figure 5.8. *Correlation between height profiles and EC-TERS AuOx band intensities. (A,B,C) EC-STM (black) and corresponding EC-TERS (pink) line profiles from regions marked with a,b,c in Figure 5.7C-F. Distance error bars are extimated to be ±0.47 nm. (D) Difference in AuOx peak area vs. difference in defect structure height. Blue and green data sets were recorded with different tips on different days and samples. The Δheight error bars are estimated to be ±0.25 nm. The Δpeak-area error bars are determined from the standard deviation either at flat Au regions or in the OFF state. Solid lines are guides to the eye.*

height difference on the nanodefect displays a linear relation up to about 3 nm height difference before saturation of the EC-TERS signal (Figure 5.8D). As the EC-TER signal intensity is linearly proportional to the number of scatterers, the observed linear increase

in signal intensity with increasing amount of AuOx at the defects is reasonable. The intensity saturation above 3 nm structure height is likely due to a limited film thickness of AuOx. Surface AuOx growth was reported to be limited to three monolayer equivalents of oxygen, or 6 monolayer equivalents of AuOx due to Au-O place exchange, and higher anodic potentials are required for Au oxidation of lower-lying (bulk) Au layers [TF97, AK86]. In other words, in the ON state, only surface oxidation of defects is selectively triggered up to a depth of maximum 6 monolayers of AuOx, corresponding to a AuOx film thickness of ca. 3 nm. Note that one might additionally expect a lowering in plasmonic enhancement because of a decreased gap mode efficiency with increasing dielectric layer thickness >2 nm [Mub12]. However, this effect is expected to be at least partly compensated by the feedback regulation of the EC-STM that leads to a decreased tip-sample distance and thus leads to an increased gap enhancement on AuOx compared to on Au at a fixed i_t. Moreover, Al_2O_3 thin films of comparable thickness are commonly used as protective coatings on TERS tips and have been reported to not significantly alter the plasmonic enhancement [Bar09].

Our experimental approach allows us to directly correlate the single-site EC-TERS nanoscopic information with the macroscopic CV that displays the average response of the whole electrode surface. Theoretically, one monolayer (ML) AuOx (or 1/2 ML O_2) amounts to 222 µC/cm^2 on Au(111) for 1-electron transfer [AK86]. A complete surface oxidation reaching 6 ML AuOx would amount to 1332 µC/cm^2, roughly twice the amount of total charge we measure. Therefore, terrace oxidation likely is limited to the topmost one or two surface (mostly terrace) layers, in agreement with literature [Peu84]. In contrast, the oxidation of the defect sites, however, reaches about 6 ML as inferred from EC-TERS and EC-STM data. Given the total electrode defect charge density of ca. 60 µC/cm^2 and the surface-limited oxide growth of 6 ML AuOx at defect sites, we quantify the surface defect coverage to be about 4.5% for the well-defined Au(111) electrode, a non-negligible amount despite the high quality of the employed single crystal. Our data thus provides direct experimental evidence for the importance of few active (defect) sites for the total catalytic surface reactivity and additionally confirms that the macroscopic CV potential region around 1.45 V vs. Pd-H originates from nanodefect oxidation, as previously found in the literature [Kol00, Zhu13].

5.5 Revealing defect chemistry on the 10 nm scale

In addition to nanoscopic localization and quantification of reaction products, operando EC-TERS nanoscopy provides valuable insight into the local chemical nature of the surface specimen from band position analysis, owing to the extreme energy (frequency) resolution of Raman spectroscopy of typically around 1.6 cm^{-1} (0.2 meV) [Mar17b]. Figure 5.9 shows two example EC-TER spectra recorded at different positions on an oxidized Au nanodefect and the respective Gaussian peak fits, which are clearly separated by about 10 cm^{-1}.

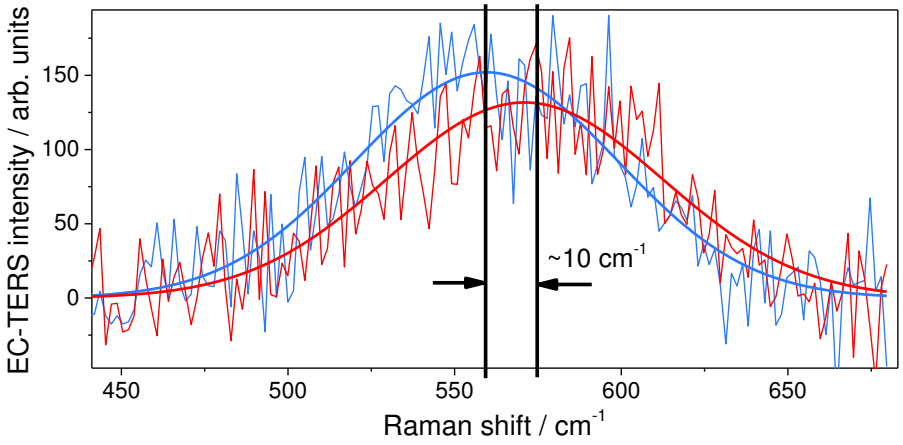

Figure 5.9. *Example (linear background subtracted) EC-TER spectra with similar peak intensities recorded at two different locations on the oxidized Au nanodefect and corresponding Gaussian peak fits. The peak centers are significantly separated by about 10 cm^{-1}.*

Figure 5.10A shows an EC-TERS map reconstructed from the AuOx peak positions as obtained from an unconstrained single Gaussian peak fit (see Section 5.7 for further details) from the data set shown in Figure 5.7F, ON. The AuOx peak position differs markedly between ca. 582 and 553 cm^{-1} as a function of probe location on the nanodefects. Notably, for flat areas, the peak is located at Raman shifts above 565 cm^{-1} (Figure 5.10B, Figure 5.10C sides), while for stepped defect parts, the Raman shift is smaller than 565 cm^{-1} (Figure 5.10C middle). Generally, the Raman shift decreases with a lowering of the metal-site coordination [DM13]. For (bulk) AuOx species, two prominent geometries, Au_2O_3 and Au_2O, were calculated to exhibit Au-O vibrations at 581 and 563 cm^{-1}, respectively [Shi07], which are very close to the Raman shifts observed in our experiments. Thus we conclude that at least two distinct AuOx species of different geometric coordination are locally present within the nanodefects. The species with the higher Au-O coordination

(larger Raman shift), possibly Au_2O_3, can be found on wider defect terraces while the structure with lower Au-O coordination (smaller Raman shift), possibly Au_2O, is located at the sharper protrusions of the nanodefects (Figure 5.10D)[1]. Such intra-defect spatial reaction heterogeneity has recently been predicted theoretically for electrocatalytic H_2 dissociation on Pt [Len19].

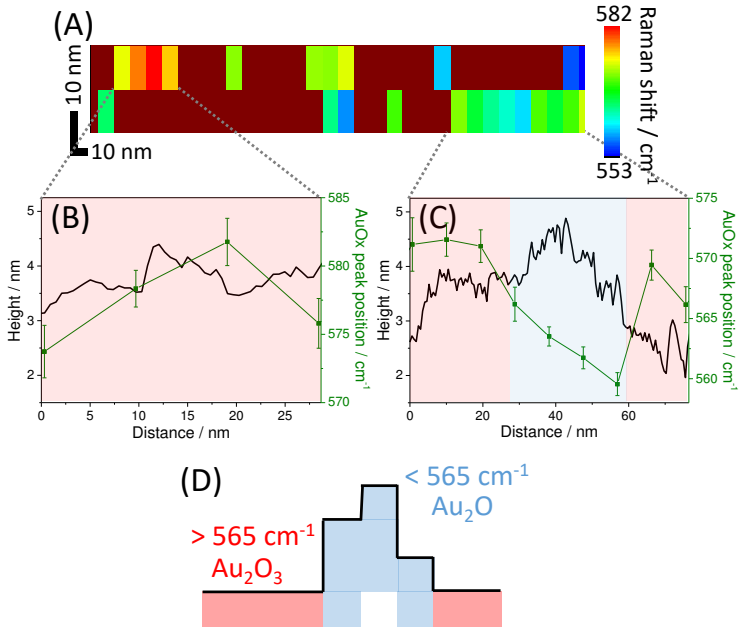

Figure 5.10. *Nanometer-resolved chemical nature of AuOx species. (A) EC-TERS map reconstructed from the AuOx peak position corresponding to the upper part of Figure 5.7F. (B,C) Correlation between height profiles and EC-TERS peak positions. The y-error bars represent the standard deviation of the bootstrapping fitting analysis (see Section 5.7 for details). (C) Schematic illustrating the difference in AuOx peak position, i.e. in chemical nature, at different locations on the nanodefect.*

5.6 Conclusions and Outlook

In summary, we have demonstrated how label-free operando EC-TERS can be used to resolve inter- and intra-defect reactivity heterogeneity for water splitting at defect oxidation potentials on Au with 10 nm chemical spatial feature sensitivity. EC-TERS maps have revealed site-specific surface oxidation of Au nanodefects up to a maximum of 3 nm AuOx layer thickness. The highly local spectral fingerprints indicate formation of

[1]Note that no apparent difference between experiments in H_2O- and D_2O-based electrolytes was detected.

at least two AuOx species with distinct coordination numbers located at defect terrace or defect protrusion sites that are tentatively assigned to Au_2O_3 and Au_2O, respectively. Correlating electrode averaged and nanoscopic site-specific information, we infer a defect coverage of ca. 4.5% on the high-quality Au(111) single crystal.

With help of optics, e.g. by implementation of a spatial light modulator (SLM) to compensate focus distortion due to light aberration at the air-glass-electrolyte interface [Mar18], implementation of an electron multiplying (EM) CCD instead of a conventional CCD camera [Bha19b], additional insulation adaptations and further methodology development, we expect to reach a spatial chemical sensitivity of <3 nm as previously reported for in-air TERS catalytic studies [Su18]. Minimizing thermal drift, by reducing acquisition times from seconds to milliseconds and thus increasing scanning speed, is one of the important next technical/experimental objectives. Further setup modifications to include temperature control and to completely oxygen free electrochemical environments would broaden the operando conditions accessible with EC-TERS. Additional EC-TERS spectro-electrochemical cell design considerations, e.g. enlarging the electrolyte volume and moving the CE to a separate cell compartment, would free additional space making it easier to view the tip-sample junction and EC-STM tip during approach and will thus improve setup handling. Such EC-TERS cell adaptations would also allow introduction of commercially available micro-reference electrodes, which, paired with modifications of the EC-TERS tip coating materials (possibly required depending on the electrolyte), would provide means to work in a wider range of different electrolytes and pH.

Further EC-TERS experiments will ultimately aid, for example, to resolve the long-standing quests concerning the broad and asymmetric AuOx peak shape and chemical interpretation thereof [Des86] and the nanoscale distribution and chemical composition of reaction intermediates and products, essential for the development of advanced water splitting or oxygen evolution catalysts [Gri17, Rei17]. Here, the next important step is to achieve EC-TERS monitoring of temporarily adsorbed reaction intermediates during OER and ORR, as recently demonstrated by EC-SERS [DM13, Don19]. With further methodology development and continuous technical setup improvement, we believe that EC-TERS can provide extra-ordinary insights on a wealth of (electro)chemical reactions occurring at the nanoscale, possibly reaching even the single catalytically active site in the future.

5.7 EC-TERS data analysis

EC-TERS reactivity mapping

The EC-TERS reactivity maps presented in Figure 5.7 were obtained in the scan-to-point mode. This scan-to-point mode records the EC-STM image while scanning to the points at which EC-TER spectra are recorded. Due to thermal drift and a spectral acquisition time of 1 to 3 s, slight shifts in the surface morphology before and after spectral acquisition are apparent. In Figure 5.11C, this phenomenon is further highlighted. The EC-STM image recorded under reaction conditions at 1.45 V vs. Pd-H exhibits 'lines', at which the EC-TER spectra were acquired. Since the spectral acquisition time is larger than the time required for the EC-STM to record a single line (32 pixels x 1-3 s vs. 1 line/s), thermal drift is more apparent. For Figure 5.7A,C,E and Figure 5.11A,C, the recorded EC-STM images were flattened according to the standard procedure in Gwyddion (5^{th} polynomial degree). The images were recorded with 1 line/s scan speed and 512 points per 300 nm distance. The tunneling current setpoint was 1 nA.

The EC-TERS reactivity maps were created as follows: First, the raw EC-TER spectra were Fourier-filtered in matlab using the interactive Fourier Filter (iFilter.m; matlab file exchange) to remove high frequency noise. Figure 5.12A shows example filtered and unfiltered EC-TER spectra. The filter parameters were as follows: frequency = 0.00060677; period = 1648.0761; width = 0.005-0.015; shape = 5. A linear baseline was determined within the boundaries of 440 to 680 cm^{-1} for each individual Fourier-filtered EC-TER spectrum and then subtracted from the Fourier-filtered EC-TER spectrum (Figure 5.12). Afterwards, the AuOx peak area with the boundaries between 440 and 680 cm^{-1} was determined by simple integration (trapz, matlab). The obtained peak area of the 440 to 680 cm^{-1} peak region was then plotted in OriginPro 9.1 (contour plot). In Figure 5.7, the zero scale bar value was determined by averaging 64 pixels at the OFF state (1.1 V vs. Pd-H) and adding three times the standard deviation (3649 + 3*656 = 5617). The maximum scale bar value accounts to 17550. In Figure 5.7D, the zero scale bar value was set to the average of 64 pixels at a flat Au surface region and adding three times the standard deviation (969 + 3*87 = 1230). The maximum scale bar value accounts to 1715. In Figure 5.7F, the zero scale bar value was set to the average of 8 spectra within the flat Au surface region (ON state) and adding three times the standard deviation (5130 + 3*998 = 8124). The maximum scale bar value accounts to 20800. If the zero scale bar value is determined from the OFF state (average from 64 pixels), as for Figure 5.7B, the determined zero scale bar value is 6319 (3961 + 3*786). Figure 5.13 compares the

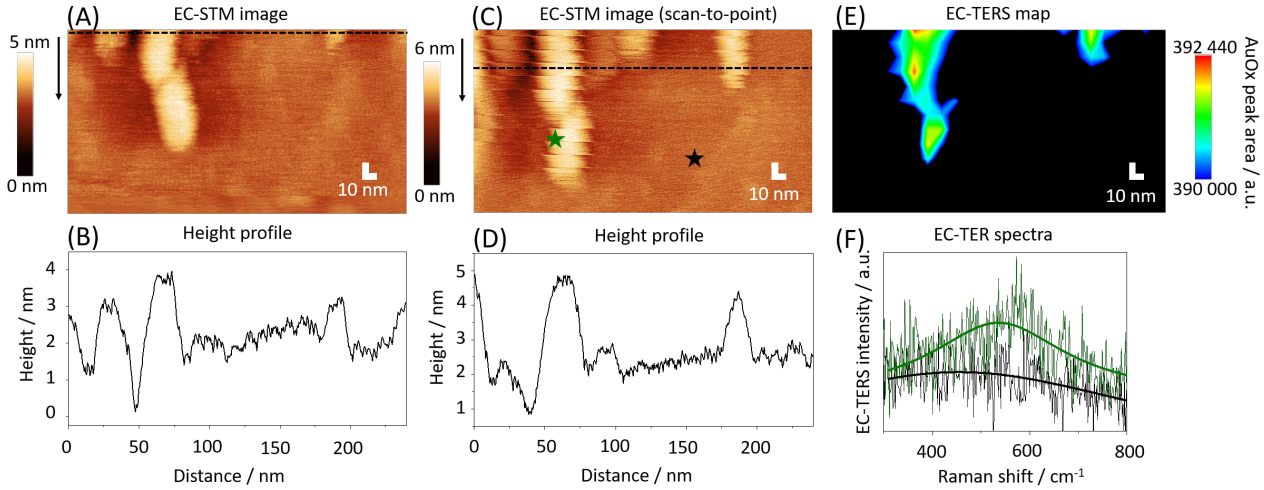

Figure 5.11. *EC-TERS mapping. (A) EC-STM image recorded from top to bottom at 1.45 V vs. Pd-H (i_t = 1 nA, E_{tip} = 1.0 V vs. Pd-H, 140 nm x 240 nm, scan speed = 1 line/s) before EC-TERS mapping. (B) Corresponding EC-STM line profile along the dotted black line in (A). (C) EC-STM image recorded as scan-to-point image while simultaneously acquiring EC-TER spectra at the equidistant 'lines' with 9.4 nm distance (mismatch due to thermal drift). Black arrow indicates scan direction. (D) Height profile along the dotted black line in (C). (E) EC-TERS map indicating the peak area of the 560-580 cm^{-1} AuOx peak as well as changes in EC-TER background (pixel size = 9.4 nm, 1 s acquisition time per pixel). The EC-TERS map was created by integrating the AuOx region without background subtraction (cf. Figure 5.7 for background-subtracted map). (F) EC-TER spectra recorded during defect oxidation (at 1.45 V vs. Pd-H) at defect site (green) and flat Au region (black), corresponding to the marked green and black stars in (C). The acquisition time accounted to 3 s. Thick green and black lines represent guides to the eye.*

resulting maps using both determined zero scale bar values. The EC-TERS maps directly reveal that the three nano-defective structural features in Figure 5.7E and Figure 5.13A,C are most reactive toward the electro-oxidation of Au.

Estimated thermal drift

The thermal drift of our EC-TERS measurements can be estimated from subsequently recorded EC-STM images and the time needed to record the EC-STM images. From the EC-STM images underlying Figure 5.11A and B, we estimated a thermal drift of ca. 120 nm/h in x-direction and 45 nm/h in y-direction. These values correspond well to thermal drift values reported in the literature of about 1 to 2 nm/min for STM instruments [Che14a]. EC-TERS intensity profiles in Figures 5.8A to C were adjusted to the apparent thermal drift of less than half a pixel.

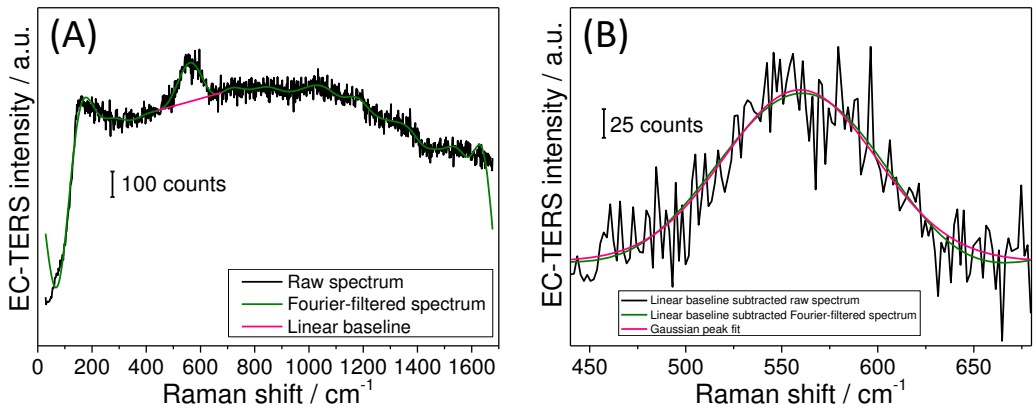

Figure 5.12. *Data treatment for mapping and fitting. (A) Example raw and Fourier-filtered EC-TER spectra (black vs. green) and the linear baseline (pink). (B) Linear baseline subtracted raw and Fourier-filtered EC-TER spectra as well as the single unconstraint Gaussian peak fit.*

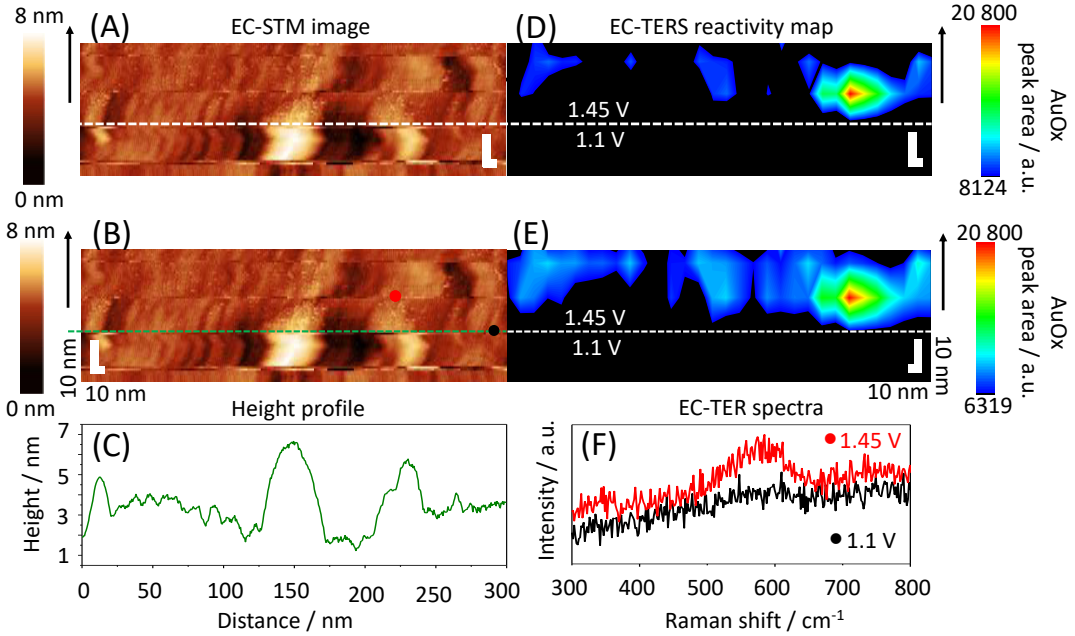

Figure 5.13. *Influence of different scale bar boundaries. (A,B) EC-STM image recorded from bottom to top while the sample potential was switched from 1.1 to 1.45 V vs. Pd-H halfway through the image (white and green dotted line). (C) Height-profile along the dotted green line revealing three distinct surface structures. (D,E) EC-TERS reactivity map with different lower boundaries emphasizing the most reactive spots on the Au surface. Black arrows indicate scan directions. (F) Example EC-TER spectra at 1.45 V vs. Pd-H (red) and 1.1 V vs. Pd-H (black) at the corresponding red and black marks in (B).*

Peak position determination

Figure 5.12B shows an example unconstraint fitting result of the AuOx peak region around 560 to 580 cm^{-1} with a single Gaussian peak shape using matlab software (peakfit.m, matlab file exchange) after linear background subtraction as described earlier. In this way, the peak positions of Figure 5.10 were determined from the Fourier-filtered EC-TER spectra. The fitting errors were estimated by fitting the unfiltered raw spectra with a bootstrapping analysis incorporated in the matlab software (peakfit.m, matlab file exhange).

Additional EC-TERS/STM line profiles

Figure 5.14 shows additional line profiles across the defective nano-structures of Figure 5.7C. EC-TERS is capable to correlate EC-STM electronic topography with EC-TERS chemical information. The defective nano-structures portray reproducibly the largest AuOx EC-TERS signal in comparison to rather flat surface regions. Nano-structures of 20 to 50 nm lateral dimensions can be resolved (Figure 5.8A,B and Figure 5.14). Moreover, Figure 5.8C demonstrates that for the different step structures the EC-TERS intensity changes sharply within the 9.4 nm pixel size, suggesting that the spatial chemical feature sensitivity is likely even lower than the pixel size used in this work.

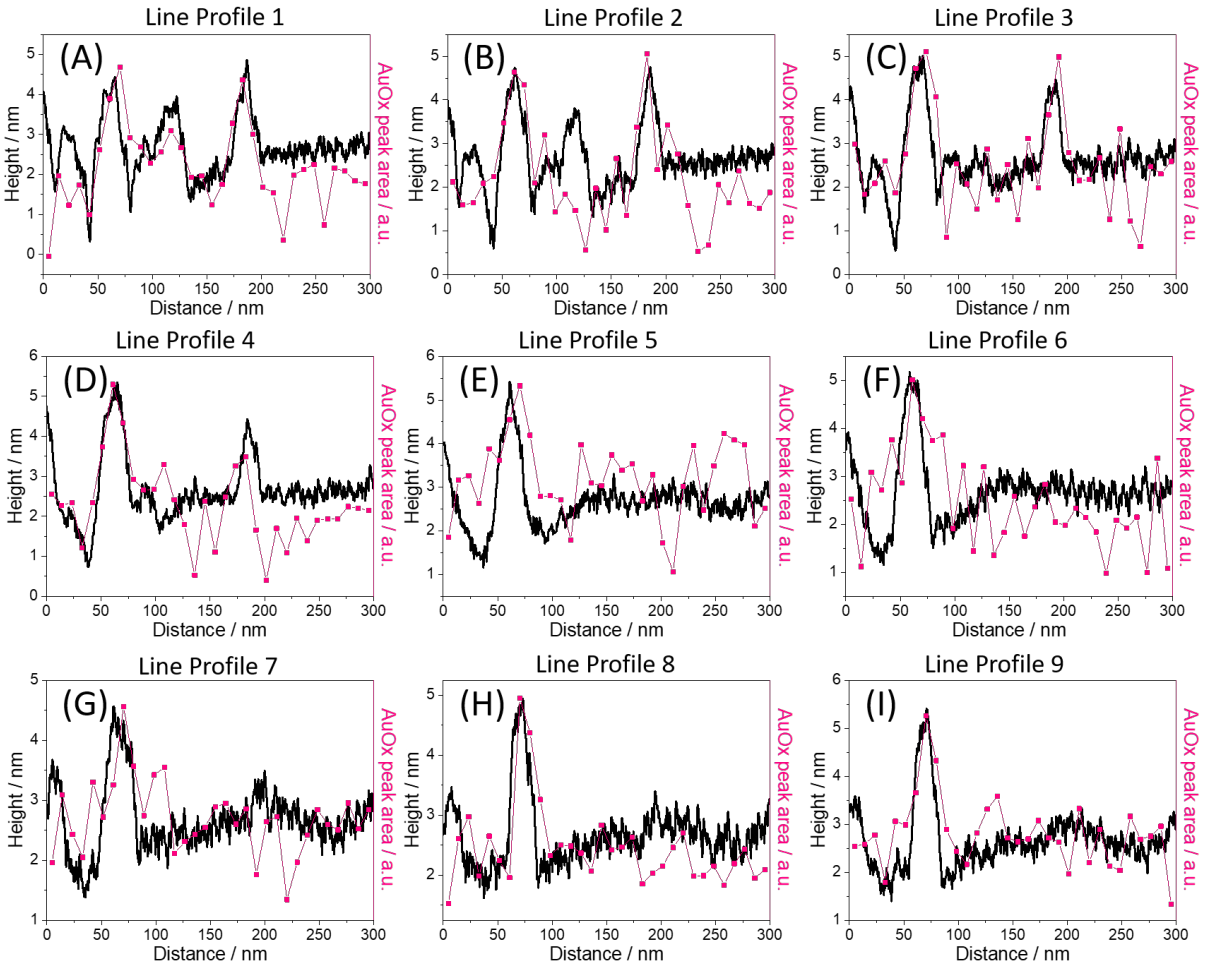

Figure 5.14. *Simultaneously acquired EC-STM and EC-TERS line profiles. Additional line profiles of Figure 5.7C,D correlating EC-STM (black) and EC-TERS AuOx peak area (pink).*

Chapter 6

Conclusions and Outlook

This chapter is partly reproduced/adapted from 'Jonas H. K. Pfisterer and Katrin F. Domke, "Unfolding the versatile potential of EC-TERS for electrocatalysis", Current Opinion in Electrochemistry, 2018, 8, 96-102', published by Elsevier in 2018 [Pfi18].

In the following chapter, we conclude the thesis by first summarizing the most important overall findings elaborated within this work and finally discussing subsequent experiments currently underway in our laboratory and possible research directions for the future.

6.1 Conclusions

The presented results of this thesis show that electrochemical plasmon-enhanced vibrational spectroscopies constitute powerful experimental techniques that allow detailed molecular insight into electro-catalytic surface reactivity under realistic electrochemical reaction conditions. EC-SERS, EC-SEIRAS and EC-TERS are complementary to each other, but also complementary to other experimental methods in the field of electrochemical surface science, such as electrochemical impedance spectroscopy or cyclic voltammetry, by providing surface-molecular specific information in addition to the current-voltage response.

Combining classical electrochemical potential-step experiments with EC-SERS, we show how EC-SERS potential-jump experiments can be utilized to monitor short-lived reaction intermediates during the electro-reduction of polycrystalline AuOx in sulfuric acid electrolyte. Electrochemical potential-jump experiments from Au oxidation potentials to the onset potential of the AuOx reduction provide means to study the reaction processes at a reduced reaction speed, which is of interest for a variety of spectro-electrochemical

techniques, such as EC-SEIRAS and -SERS, and is expected to be applicable to numerous other electrochemical reactions, for example formic acid oxidation. With EC-SERS potential-jump measurements, we identify AuOx and Au-OH intermediates in acidic media, which are challenging to detect and important for various electrocatalytic reactions. The combined efforts of advanced computer calculations considering implicit solvent contributions and smart experiments are required to gain mechanistic insight into the complex working principles of surface reactivity and material degradation effects under reaction conditions.

Employing EC-TERS in the fields of electrocatalysis and corrosion science for the first time, the potential-dependent detection of the operando formation of surface reaction products at the nanoscale is possible. This is a crucial step for the implementation of the EC-TERS technique in electrocatalysis and corrosion science because, in contrast to previous EC-TERS studies, the detected surface species is formed in situ and does not represent a pre-deposited organic SAM electrode. Our EC-TERS setup is sensitive enough to detect AuOx reaction products during Au(111) electro-oxidation. We demonstrate the EC-TERS reactivity mapping capability by differentiating between active Au nanodefects selectively oxidized at 1.45 V vs. Pd-H and non-active flat Au regions with a chemical spatial feature sensitivity of about 10 nm.

Moreover, EC-TERS is capable to locally resolve differences in the local nanoscale chemistry. We observe significant changes in the AuOx peak position depending on the location on the Au nanodefect. This result suggests that the broad AuOx peak in the 500 to 600 cm^{-1} region appearing during complete Au surface oxidation most likely originates from different AuOx species formed at the surface. The scence is set for exciting future EC-TERS projects in the fields of electrocatalysis, corrosion science or related solid-liquid interface disciplines, offering unprecedented insight into the working mechanisms of various energy materials on the nanoscale level.

6.2 A bright EC-TERS future for electrocatalysis

The in-situ surface-enhanced Raman analog, EC-SERS, has repeatedly been used to resolve vibrational signals of reaction intermediates important for key energy conversion reactions [Smi97, Zhu13, DM13, Hua16, Don19]. Providing similar Raman enhancement factors as EC-SERS, EC-TERS can thus be expected to further extend our understanding of such fuel cell reactions to nanoscale detail. For the application of EC-TERS in elec-

trocatalysis, the next step for our EC-TERS methodology is to show that key reaction intermediates, such as CO, OOH or OH species, temporarily adsorbed at the catalyst surface can be detected. Moreover, the chemical spatial resolution achievable at solid-liquid interfaces remains to be pushed to reach, ideally, a few nanometers or better by further technical advances such as optimizing the laser focus in liquid and improving setup stability. Borrowing from UHV-STM approaches, active (thermal) drift correction can possibly help to correlate EC-TERS and SPM images more easily in the future [Rah10]. Note that as extreme field gradients act on the species under investigation in (EC-)TERS, both in air and in liquid experiments, utmost care has to be taken to exclude (photo)thermal damage of the species of interest or the catalyst, or undesired laser-induced (side) reactions. As EC-TERS is still in its infancy, systematic exploration of laser-induced artefacts will be required on well-defined and understood model systems to provide a thorough understanding of the full capabilities and limitations of the technique for electrocatalytic studies.

Currently, the EC-TERS work in the Domke lab is extended to bimetallic electrocatalyst systems, such as monoatomically high Pd and Ir islands deposited on Au(111) electrodes. Pd and Ir electro-oxidize at more negative potentials compared to Au. Selectively oxidizing the Pd or Ir islands, while keeping the Au(111) substrate oxide free, should allow EC-TERS detection of the PdOx and IrOx only at the oxidized metal islands. Variation in island size with diameters of about 3 to 30 nm and EC-TERS mapping of the oxide islands would then allow determination of the currently achievable chemical spatial resolution of our EC-TERS setup. At the same time, such EC-TERS mapping experiments would resolve the question about the potential-dependent chemical nature of IrOx and PdOx of such nanostructures, i.e. which oxide species form at these monoatomically high islands as a function of applied potential. In addition, possible edge boundary effects could be directly investigated, where the edge atoms of the metal islands possibly exhibit increased reactivity, as in the case for HER on Pd on Au(111) [Pfi17]. Moreover, possible corrosion effects can be studied by excursions to higher applied overpotentials and subsequent EC-TERS inspection of the metallic islands. The well-defined bimetallic systems can further be utilized to study the electro-oxidation of formic acid, HCOOH, at low overpotentials (to assure island stability). The reaction intermediates are expected to be detectable under continuous reaction conditions due to the incorporated CO bonds and previously reported EC-SERS experiments [Bel05]. It is important to note that island stability during EC-TERS measurements is of particular importance and the applied electrode potentials need to be carefully chosen. For example, experiments of MoS_2 islands on Au(111) revealed their instablity during the HCOOH electro-oxidation.

To increase both sensitivity and resolution, further setup development is currently underway in our laboratory. Implementation of a spatial light modulater (SLM) can help to optimize the laser focusing by phase-modulation of the laser excitation beam [Mar18] and implementation of an EMCCD camera will provide an additional increase in signal intensity. The increased signal-to-noise ratios will allow reduction of the acquisition time per pixel from seconds to hundreds of milliseconds. Additional vibrational damping adds to the reduction of thermal drift. Furthermore, adaptations of the electrochemical cell design, such as increasing the cell volume and offering oxygen free work environments, will allow improved setup handling and extend the range of systems to be investigated. In addition, recent results of the Ren group suggest that the implementation of a water immersion objective would further increase our EC-TERS setup sensitivity [Hua19].

In the future, EC-TERS potential-jump experiments are envisioned to provide the desired nanoscale insight of the analog EC-SERS experiments presented in this work. According to recent achievements with the EC-SERS technique under electro-catalytic reaction conditions, EC-TERS can potentially provide the nanoscale insight into numerous electrochemical reactions, for example ORR and OER, the oxidation of small organic molecules or CO_2 electro-reduction. Methodologically, exciting future research questions are for example how we can discriminate between adsorbed sulfate ions and the bulk solution or how we can distinguish interfacial water from bulk water. Is it possible to combine video-EC-STM with the EC-TERS approach, can EC-TERS measurements be performed on single Pt nanoparticles of different shape and size or can EC-AFM-TERS be employed on realistic rough catalyst electrodes? Can EC-TERS provide the necessary parameter input for the development of advanced theoretical simulation tools that can adequately predict electrified solid-liquid interfaces under non-equilibrium reaction conditions on a molecuar and/or atomic level? Moreover, recent studies on functionalized EC-TERS tips [Pie16, Tou17, Gou18] hold promise for the combination of the SECM, EC-TERS and EC-SERS methodologies in the future. Attaching SERS-active EC-SHINER nanoparticles to an SECM tip or ultra-microelectrode or possibly using the EC-TERS-tip as a nano-SECM electrode quantifying the faradaic currents during electrochemical reactions are additional exciting future venues.

With further methodology development and continuous technical setup improvements, the EC-TERS technique will mature into the versatile operando nano-tool required to answer (or contribute to answer) the above-mentioned questions and to identify local active

site chemistry for a wealth of electrochemical reactions at the nanoscale level. Providing high chemical, spatial and temporal resolution, EC-TERS can thus help us to understand the fundamental processes of electrocatalysis, corrosion science and electrochemical surface science in general. The detailed molecular and nanoscale understanding gained in this way will aid the rational engineering of improved energy materials contributing to a sustainable and affordable energy future and thus to one of the great challenges of our time.

Bibliography

[AK86] H. Angerstein-Kozlowska, B. E. Conway, A. Hamelin and L. Stoicoviciu: *Elementary steps of electrochemical oxidation of single-crystal planes of Au-I. Chemical basis of processes involving geometry of anions and the electrode surfaces*, Electrochimica Acta **31**, 1051 (1986).

[AK87] H. Angerstein-Kozlowska, B. E. Conway, A. Hamelin and L. Stoicoviciu: *Elementary steps of electrochemical oxidation of single-crystal planes of Au Part II. A chemical and structural basis of oxidation of the (111) plane*, Journal of Electroanalytical Chemistry **228**, 429 (1987).

[Álv00] B. Álvarez, V. Climent, J. M. Feliu and A. Aldaz: *Determination of different local potentials of zero charge of a Pd-Au(111) heterogeneous surface*, Electrochemistry Communications **2**, 427 (2000).

[And00] M. S. Anderson: *Locally enhanced Raman spectroscopy with an atomic force microscope*, Applied Physics Letters **76**, 3130 (2000).

[Ata96] K.-i. Ataka, T. Yotsuyanagi and M. Osawa: *Potential-dependent reorientation of water molecules at an electrode/electrolyte interface studied by surface-enhanced infrared absorption spectroscopy*, The Journal of Physical Chemistry **100**, 10664 (1996).

[Ata98] K.-i. Ataka and M. Osawa: *In situ infrared study of water-sulfate coadsorption on gold(111) in sulfuric acid solutions*, Langmuir **14**, 951 (1998).

[Ban08] M. J. Banholzer, J. E. Millstone, L. Qin and C. A. Mirkin: *Rationally designed nanostructures for surface-enhanced Raman spectroscopy*, Chemical Society Reviews **37**, 885 (2008).

[Ban14] A. S. Bandarenka, E. Ventosa, A. Maljusch, J. Masa and W. Schuhmann: *Techniques and methodologies in modern electrocatalysis: evaluation of activity, selectivity and stability of catalytic materials*, The Analyst **139**, 1274 (2014).

[Bar61] J. Bardeen: *Tunneling from a many-particle point of view*, Physical Review Letter **6**, 57 (1961).

[Bar90] J. V. Barth, H. Brune, G. Ertl and R. J. Behm: *Scanning tunneling microscopy observations on the reconstructed Au(111) surface: Atomic structure, long-range superstructure, rotational domains and surface defects*, Physical Review B **42**, 9307 (1990).

[Bar01] A. J. Bard and L. R. Faulkner: *Electrochemical methods: Fundamentals and applications*, vol. 2, John Wiley & Sons New York, 2001.

[Bar09] C. A. Barrios, A. V. Malkovskiy, A. M. Kisliuk, A. P. Sokolov and M. D. Foster: *Highly stable, protected plasmonic nanostructures for tip enhanced Raman spectroscopy*, Journal of Physical Chemistry C **113**, 8158 (2009).

[Bar13] M. M. Barsan, M. Emilia Ghica and C. M. Brett: *Electrochemical biosensors*, Chemical Society Reviews **39**, 1747 (2013).

[Bel03] A. T. Bell: *The impact of nanoscience on heterogeneous catalysis*, Science **299**, 1688 (2003).

[Bel05] G. L. Beltramo, T. E. Shubina and M. T. M. Koper: *Oxidation of formic acid and carbon monoxide on gold electrodes studied by surface-enhanced Raman spectroscopy and DFT*, ChemPhysChem **6**, 2597 (2005).

[Ben16] C. L. Bentley, M. Kang and P. R. Unwin: *Time-resolved detection of surface oxide formation at individual gold nanoparticles: Role in electrocatalysis and new approach for sizing by electrochemical impacts*, Journal of the American Chemical Society **138**, 12755 (2016).

[Ben19] C. L. Bentley, J. Edmondson, G. N. Meloni, D. Perry, V. Shkirskiy and P. R. Unwin: *Nanoscale electrochemical mapping*, Analytical Chemistry **91**, 84 (2019).

[Bha19a] A. Bhattarai and P. Z. El-Khoury: *Nanoscale chemical reaction imaging at the solid–liquid interface via TERS*, The Journal of Physical Chemistry Letters **10**, 2817 (2019).

[Bha19b] A. Bhattarai, A. G. Joly, A. Krayev and P. Z. El-Khoury: *Taking the plunge: Nanoscale chemical imaging of functionalized gold triangles in H_2O via TERS*, Journal of Physical Chemistry C **123**, 7376 (2019).

[Bin82a] G. Binnig, H. Rohrer, C. Gerber and E. Weibel: *Surface studies by scanning tunneling microscopy*, Physical Review Letters **49**, 57 (1982).

[Bin82b] G. Binnig, H. Rohrer, C. Gerber and E. Weibel: *Tunneling through a controllable vacuum gap*, Applied Physics Letters **40**, 178 (1982).

[Bin86] G. Binning, C. F. Quate and C. Gerber: *Atomic force microscope*, Physical Review Letters **56**, 930 (1986).

[Bin87] G. Binnig and H. Rohrer: *Scanning tunneling microscopy - from birth to adolescence*, Reviews of Modern Physics **59**, 615 (1987).

[Bis93] D. M. Bishop: *The vibrational Stark effect*, Journal of Chemical Physics **98**, 3179 (1993).

[Bli07] T. Bligaard and J. K. Nørskov: *Ligand effects in heterogeneous catalysis and electrochemistry*, Electrochimica Acta **52**, 5512 (2007).

[Boc13] J. O. M. Bockris: *The hydrogen economy: Its history*, International Journal of Hydrogen Energy **38**, 2579 (2013).

[Bri00] L. E. Briand, W. E. Farneth and I. E. Wachs: *Quantitative determination of the number of active surface sites and the turnover frequencies for methanol oxidation over metal oxide catalysts*, Catalysis Today **62**, 219 (2000).

[Bro95] G. M. Brown and G. A. Hope: *In-situ spectroscopic evidence for the adsorption of SO_4^{2-} ions at a copper electrode in sulfuric acid solution*, Journal of Electroanalytical Chemistry **382**, 179 (1995).

[Bru35] D. A. G. Bruggeman: *"Calculation of various physical constants of heterogeneous substances, part I: Dielectric constants and conductivities of mixtures of isotropic substances*, Annalen der Physik **24**, 636 (1935).

[Can09] L. Cancado, A. Jorio, A. Ismach, E. Joselevich, A. Hartschuh and L. Novotny: *Mechanism of near-field Raman enhancement in two-dimensional systems*, Physical Review Letters **103**, 1 (2009).

[Can11] H. Cang, A. Labno, C. Lu, X. Yin, M. Liu, C. Gladden, Y. Liu and X. Zhang: *Probing the electromagnetic field of a 15-nanometre hotspot by single molecule imaging*, Nature **469**, 385 (2011).

[Cha17] S. Chaunchaiyakul, A. Setiadi, P. Krukowski, F. C. I. Catalan, M. Akai-Kasaya, A. Saito, N. Hayazawa, Y. Kim, H. Osuga and Y. Kuwahara: *Nanoscale dehydrogenation observed by tip-enhanced Raman spectroscopy*, Journal of Physical Chemistry C **121**, 18162 (2017).

[Che07] X. Cheng, Z. Shi, N. Glass, L. Zhang, J. Zhang, D. Song, Z. S. Liu, H. Wang and J. Shen: *A review of PEM hydrogen fuel cell contamination: Impacts, mechanisms, and mitigation*, Journal of Power Sources **165**, 739 (2007).

[Che13] S. Cherevko, A. A. Topalov, A. R. Zeradjanin, I. Katsounaros and K. J. Mayrhofer: *Gold dissolution: Towards understanding of noble metal corrosion*, RSC Advances **3**, 16516 (2013).

[Che14a] C. Chen, N. Hayazawa and S. Kawata: *A 1.7 nm resolution chemical analysis of carbon nanotubes by tip-enhanced Raman imaging in the ambient*, Nature communications **5**, 3312 (2014).

[Che14b] S. Cherevko, A. R. Zeradjanin, G. P. Keeley and K. J. J. Mayrhofer: *A comparative study on gold and platinum dissolution in acidic and alkaline media*, Journal of The Electrochemical Society **161**, H822 (2014).

[Che18a] X. Chen, V. Brasiliense and R. P. Van Duyne: *Operando observation of molecular-scale manipulation using electrochemical tip-enhanced Raman spectroscopy*, Journal of Physical Chemistry C **122**, 24329 (2018).

[Che18b] X. Chen, G. Goubert, S. Jiang and R. P. Van Duyne: *Electrochemical STM tip-enhanced Raman spectroscopy study of electron transfer reactions of covalently tethered chromophores on Au(111)*, Journal of Physical Chemistry C **122**, 11586 (2018).

[Che19] X. Chen, P. Liu, Z. Hu and L. Jensen: *High-resolution tip-enhanced Raman scattering probes sub-molecular density changes*, Nature Communications **10**, 1 (2019).

[Chu12] S. Chu and A. Majumdar: *Opportunities and challenges for a sustainable energy future*, Nature **488**, 294 (2012).

[Cla79] J. Clavilier, R. Faure, G. Guinet and R. Durand: *Preparation of monocrystalline Pt microelectrodes and electrochemical study of the plane surfaces cut in the direction of the 111 and 110 planes*, Journal of Electroanalytical Chemistry and Interfacial Electrochemistry **107**, 205 (1979).

[Col16] V. Colic, M. D. Pohl, D. Scieszka and A. S. Bandarenka: *Influence of the electrolyte composition on the activity and selectivity of electrocatalytic centers*, Catalysis Today **262**, 24 (2016).

[Con95] B. E. Conway: *Electrochemical oxide film formation at noble metals as a surface-chemical process*, Progress in Surface Science **49**, 331 (1995).

[Cue00] A. Cuesta, M. Kleinert and D. M. Kolb: *The adsorption of sulfate and phosphate on Au(111) and Au(100) electrodes: An in situ STM study*, Physical Chemistry Chemical Physics **2**, 5684 (2000).

[CV15] F. Calle-Vallejo, J. Tymoczko, V. Colic, Q. H. Vu, M. D. Pohl, K. Morgenstern, D. Loffreda, P. Sautet, W. Schuhmann and A. S. Bandarenka: *Finding optimal surface sites on heterogeneous catalysts by counting nearest neighbors*, Science **350**, 185 (2015).

[Deb12] M. K. Debe: *Electrocatalyst approaches and challenges for automotive fuel cells*, Nature **486**, 43 (2012).

[Des86] J. Desilvestro and M. J. Weaver: *Surface structural changes during oxidation of gold electrodes in aqueous media as detected using surface-enhanced Raman spectroscopy*, Journal of Electroanalytical Chemistry **209**, 377 (1986).

[Din16] S.-Y. Ding, J. Yi, J.-F. Li, B. Ren, D.-Y. Wu, R. Panneerselvam and Z.-Q. Tian: *Nanostructure-based plasmon-enhanced Raman spectroscopy for surface analysis of materials*, Nature Reviews Materials **1**, 16021 (2016).

[DM13] O. Diaz-Morales, F. Calle-Vallejo, C. de Munck and M. T. M. Koper: *Electrochemical water splitting by gold: evidence for an oxide decomposition mechanism*, Chemical Science **4**, 2334 (2013).

[Dom06] K. F. Domke: *Tip-enhanced Raman spectroscopy – Topographic and chemical information on the nanoscale*, Ph.D. thesis, Freie Universität Berlin (2006).

[Dom07] K. F. Domke, D. Zhang and B. Pettinger: *Tip-enhanced Raman spectra of picomole quantities of DNA nucleobases at Au(111)*, Journal of the American Chemical Society **129**, 6708 (2007).

[Dom09] K. F. Domke and B. Pettinger: *In situ discrimination between axially complexed and ligand-free Co porphyrin on Au(111) with tip-enhanced Raman spectroscopy*, ChemPhysChem **10**, 1794 (2009).

[Dom10] K. F. Domke and B. Pettinger: *Studying surface chemistry beyond the diffraction limit: 10 years of TERS*, ChemPhysChem **11**, 1365 (2010).

[Don19] J.-C. Dong, X.-G. Zhang, V. Briega-Martos, X. Jin, J. Yang, S. Chen, Z.-L. Yang, D.-Y. Wu, J. M. Feliu, C. T. Williams, Z.-Q. Tian and J.-F. Li: *In situ Raman spectroscopic evidence for oxygen reduction reaction intermediates at platinum single crystal surfaces*, Nature Energy **4**, 60 (2019).

[Dri18] L. Driessen: *Development of a tip-enhanced Raman spectrometer to investigate solid-liquid interfaces*, Ph.D. thesis, Johannes Gutenberg Universität (2018).

[Ede94] G. J. Edens, X. Gao and M. J. Weaver: *The adsorption of sulfate on gold(111) in acidic aqueous media: Adlayer structural inferences from infrared spectroscopy and scanning tunneling microscope*, Journal of Electroanalytical Chemistry **375**, 357 (1994).

[EE16] M. Escudero-Escribano, P. Malacrida, H. M. Hansen, U. Vej-Hansen, A. Velazquez-Palenzuela, V. Tripkovic, J. Schiøtz, J. Rossmeisl, I. E. L. Stephens and I. Chorkendorff: *Tuning the activity of Pt alloy electrocatalysts by means of the lanthanide contraction*, Science **352**, 73 (2016).

[Eil03] P. H. Eilers: *A perfect smoother*, Analytical Chemistry **75**, 3631 (2003).

[Elg18] N. Elgrishi, K. J. Rountree, B. D. McCarthy, E. S. Rountree, T. T. Eisenhart and J. L. Dempsey: *A practical beginner's guide to cyclic voltammetry*, Journal of Chemical Education **95**, 197 (2018).

[Fag90] P. W. Faguy, N. Markovic, R. R. Adzic, C. A. Fierro and E. B. Yeager: *A study of bisulfate adsorption on Pt(111) single crystal electrodes using in situ Fourier transform infrared spectroscopy*, Journal of Electroanalytical Chemistry **289**, 245 (1990).

[Fai18] F. Faisal, M. Bertram, C. Stumm, F. Waidhas, O. Brummel and J. Libuda: *Preparation of complex model electrocatalysts in ultra-high vacuum and transfer into the electrolyte for electrochemical IR spectroscopy and other techniques*, Review of Scientific Instruments **89**, 114101 (2018).

[Fan08] Y. Fang, N.-H. Seong and D. D. Dlott: *Measurement of the distribution of site enhancements in surface-enhanced Raman scattering*, Science **321**, 388 (2008).

[Fan15] Z. Fang, B. Bueken, D. E. De Vos and R. A. Fischer: *Defect-engineered metal-organic frameworks*, Angewandte Chemie - International Edition **54**, 7234 (2015).

[Fes17] J. Fester, M. Bajdich, A. S. Walton, Z. Sun, P. N. Plessow, A. Vojvodic and J. V. Lauritsen: *Comparative analysis of cobalt oxide nanoisland stability and edge structures on three related noble metal surfaces: Au(111), Pt(111) and Ag(111)*, Topics in Catalysis **60**, 503 (2017).

[Fes18] J. Fester, A. Makoveev, D. Grumelli, R. Gutzler, Z. Sun, J. Rodríguez-Fernández, K. Kern and J. V. Lauritsen: *The structure of the cobalt oxide/Au catalyst interface in electrochemical water splitting*, Angewandte Chemie - International Edition **57**, 11893 (2018).

[Fle74] M. Fleischmann, P. Hendra and A. McQuillan: *Raman spectra of pyridine adsorbed at a silver electrode*, Chemical Physics Letters **26**, 163 (1974).

[Gao17] P. Gao, P. Metz, T. Hey, Y. Gong, D. Liu, D. D. Edwards, J. Y. Howe, R. Huang and S. T. Misture: *The critical role of point defects in improving the specific capacitance of δ-MnO_2 nanosheets*, Nature Communications **8**, 1 (2017).

[Gir15] R. G. P. Giron and G. S. Ferguson: *Development of cathodic silence in an oxide film on a gold electrode*, Electrochimica Acta **180**, 560 (2015).

[Gjo12] B. Gjonaj, P. Johnson, M. Bonn and K. F. Domke: *Index mismatch aberration correction over long working distances using spatial light modulation*, Applied Optics **51**, 8034 (2012).

[Got98] S. Gottesfeld and J. Pafford: *A new approach to the problem of carbon monoxide poisoning in fuel cells operating at low temperatures*, Journal of The Electrochemical Society **135**, 2651 (1998).

[Gou18] G. Goubert, X. Chen, S. Jiang and R. P. Van Duyne: *In situ electrochemical tip-enhanced Raman spectroscopy with a chemically modified tip*, Journal of Physical Chemistry Letters **9**, 3825 (2018).

[Gri17] A. Grimaud, O. Diaz-Morales, B. Han, W. T. Hong, Y. L. Lee, L. Giordano, K. A. Stoerzinger, M. T. Koper and Y. Shao-Horn: *Activating lattice oxygen redox reactions in metal oxides to catalyse oxygen evolution*, Nature Chemistry **9**, 457 (2017).

[Ham96a] A. Hamelin: *Cyclic voltammetry at gold single-crystal surfaces. Part 1. Behaviour at low-index faces*, Journal of Electroanalytical Chemistry **407**, 1 (1996).

[Ham96b] A. Hamelin and A. M. Martins: *Cyclic voltammetry at gold single-crystal surfaces. Part 2. Behaviour of high-index faces*, Journal of Electroanalytical Chemistry **407**, 13 (1996).

[Han18] A. D. Handoko, F. Wei, Jenndy, B. S. Yeo and Z. W. Seh: *Understanding heterogeneous electrocatalytic carbon dioxide reduction through operando techniques*, Nature Catalysis **1**, 922 (2018).

[Har80] A. Hartstein, J. R. Kirtley and J. C. Tsang: *Enhancement of the infrared absorption from molecular monolayers with thin metal overlayers*, Physical Review Letters **45**, 201 (1980).

[Hay00] N. Hayazawa, Y. Inouye, Z. Sekkat and S. Kawata: *Metallized tip amplification of near-field Raman scattering*, Optics Communications **183**, 333 (2000).

[Hay01] S. Hayashi: *Spectroscopy of gap modes in metal particle - surface systems*, in *Near-field optics and surface plasmon polaritons*, Springer, 2001, 71–95.

[Her95] E. Herrero, J. M. Feliu, A. Wieckowski and J. Clavilier: *The unusual adsorption states of Pt(111) electrodes studied by an iodine displacement method: Comparison with Au(111) electrodes*, Surface Science **325**, 131 (1995).

[Her07] J. Hernández, J. Solla-Gullón, E. Herrero, A. Aldaz and J. M. Feliu: *Electrochemistry of shape-controlled catalysts: Oxygen reduction reaction on cubic gold nanoparticles*, Journal of Physical Chemistry C **111**, 14078 (2007).

[Hic42] A. Hickling: *Studies in electrode polarisation. Part IV. - The automatic control of the potential of a working electrode.*, Transactions of the Faraday Society **38**, 27 (1942).

[Hol85] P. Hollins and J. Pritchard: *Infrared studies of chemisorbed layers on single crystals*, Progress in Surface Science **19**, 275 (1985).

[Hör19] N. G. Hörmann, O. Andreussi and N. Marzari: *Grand canonical simulations of electrochemical interfaces in implicit solvation models*, Journal of Chemical Physics **150**, 041730 (2019).

[Hou14] J. Hou, M. Fang, A. J. P. Cardenas, W. J. Shaw, M. L. Helm, R. M. Bullock, J. A. Roberts and M. O'Hagan: *Electrocatalytic H_2 production with a turnover frequency >10^7 s^{-1}: The medium provides an increase in rate but not overpotential*, Energy and Environmental Science **7**, 4013 (2014).

[Hua16] J. Huang, A. Malek, J. Zhang and M. H. Eikerling: *Non-monotonic Surface Charging Behavior of Platinum: A Paradigm Change*, Journal of Physical Chemistry C **120**, 13587 (2016).

[Hua18] J. Huang, T. Zhou, J. Zhang and M. Eikerling: *Double layer of platinum electrodes: Non-monotonic surface charging phenomena and negative double layer capacitance*, Journal of Chemical Physics **148**, 044704 (2018).

[Hua19] S.-C. Huang, J.-Z. Ye, X.-R. Shen, Q.-Q. Zhao, Z. Zeng, M.-H. Li, D.-Y. Wu, X. Wang and B. Ren: *Electrochemical tip-enhanced Raman spectroscopy with improved sensitivity enabled by a water immersion objective*, Analytical Chemistry **x**, 1 (2019).

[Iba15] D. Ibañez, A. Santidrian, A. Heras, M. Kalbáč and A. Colina: *Study of adenine and guanine oxidation mechanism by surface-enhanced Raman spectroelectrochemistry*, Journal of Physical Chemistry C **119**, 8191 (2015).

[Ino99] Y. Inouye, N. Hayazawa, K. Hayashi, Z. Sekkat and S. Kawata: *Near-field scanning optical microscope using a metallized cantilever tip for nanospectroscopy*, SPIE **3791**, 40 (1999).

[Jar07] T. F. Jaramillo, K. P. Jørgensen, J. Bonde, J. H. Nielsen, S. Horch and I. Chorkendorff: *Identification of active edge sites for electrochemical H_2 evolution from MoS_2 nanocatalysts*, Science **317**, 100 (2007).

[Jea77] D. L. Jeanmaire and R. P. Van Duyne: *Surface Raman spectroelectrochemistry Part I. Heterocyclic, aromatic, and aliphatic amines adsorbed on the anodized silver electrode*, Journal of Electroanalytical Chemistry **84**, 1 (1977).

[Jia98] J. Jia, K. Inoue and Y. Hasegawa: *Variation of the local work function at steps on metal surfaces studied with STM*, Physical Review B - Condensed Matter and Materials Physics **58**, 1193 (1998).

[Jia15] S. Jiang, Y. Zhang, R. Zhang, C. Hu, M. Liao, Y. Luo, J. Yang, Z. Dong and J. G. Hou: *Distinguishing adjacent molecules on a surface using plasmon-enhanced Raman scattering*, Nature Nanotechnology **10**, 865 (2015).

[Jia16] N. Jiang, D. Kurouski, E. A. Pozzi, N. Chiang, M. C. Hersam and R. P. Van Duyne: *Tip-enhanced Raman spectroscopy: From concepts to practical applications*, Chemical Physics Letters **659**, 16 (2016).

[Jia19] S. Jiang, Z. Chen, X. Chen, D. Nguyen, M. Mattei, G. Goubert and R. P. Van Duyne: *Investigation of cobalt phthalocyanine at the solid/liquid interface by electrochemical tip-enhanced Raman spectroscopy*, Journal of Physical Chemistry C **123**, 9852 (2019).

[Jin13] R. Jinnouchi, T. Hatanaka, Y. Morimoto and M. Osawa: *Stark effect on vibration frequencies of sulfate on Pt(1 1 1) electrode*, Electrochimica Acta **101**, 254 (2013).

[Jon80] P. G. Jones, H. Rumpel, G. M. Sheldrick and E. Schwarzmann: *Gold(III) oxide and oxychloride*, Gold Bulletin **13**, 56 (1980).

[Kan19] G. Kang, M. Yang, M. S. Mattei, G. C. Schatz and R. P. Van Duyne: *In situ nanoscale redox mapping using tip-enhanced Raman spectroscopy*, Nano Letters **19**, 2106 (2019).

[Ker82] M. Kerker and C. G. Blatchford: *Elastic scattering, absorption, and surface-enhanced Raman scattering by concentric spheres comprised of a metallic and a dielectric region*, Physical Review B **26**, 4052 (1982).

[Kib03] L. A. Kibler: *Preparation and characterization of noble metal single crystal electrode surfaces*, International Society of Electrochemistry (2003).

[Kim00] Y. G. Kim, J. B. Soriaga, G. Vigh and M. P. Soriaga: *Atom-resolved EC-STM studies of anion adsorption at well-defined surfaces: Pd(111) in sulfuric acid solution*, Journal of Colloid and Interface Science **227**, 505 (2000).

[Kim06] J. Kim and A. A. Gewirth: *Mechanism of oxygen electroreduction on gold surfaces in basic media*, Journal of Physical Chemistry B **110**, 2565 (2006).

[Kli14] J. M. Klingsporn, M. D. Sonntag, T. Seideman and R. P. Van Duyne: *Tip-enhanced Raman spectroscopy with picosecond pulses*, The Journal of Physical Chemistry Letters **5**, 106 (2014).

[Kne97] K. Kneipp, Y. Wang, H. Kneipp, L. T. Perelman, I. Itzkan, R. R. Dasari and M. S. Feld: *Single molecule detection using surface-enhanced Raman scattering (SERS)*, Physical Review Letters **78**, 1667 (1997).

[Kne06] K. Kneipp, M. Moskovits and H. Kneipp: *Surface-enhanced Raman scattering*, Springer, 2006.

[Kod16] K. Kodama, R. Jinnouchi, N. Takahashi, H. Murata and Y. Morimoto: *Activities and stabilities of Au-modified stepped-Pt single-crystal electrodes as model cathode catalysts in polymer electrolyte fuel cells*, Journal of the American Chemical Society **138**, 4194 (2016).

[Kol86] D. M. Kolb and J. Schneider: *Surface reconstruction in electrochemistry: Au(100)-(5 x 20), Au(111)-(1 x 23) and Au(110)-(1 x 2)*, Electrochimica Acta **31**, 929 (1986).

[Kol00] D. M. Kolb: *Structure studies of metal electrodes by in-situ scanning tunneling microscopy*, Electrochimica Acta **45**, 2387 (2000).

[Kon07] T. Kondo, J. Morita, K. Hanaoka, S. Takakusagi, K. Tamura, M. Takahasi, J. N. Mizuki and K. Uosaki: *Structure of Au(111) and Au(100) single-crystal electrode surfaces at various potentials in sulfuric acid solution determined by in situ surface X-ray scattering*, Journal of Physical Chemistry C **111**, 13197 (2007).

[Kra17] S. Kradolfer, E. Lipiec, C. Baldacchini, A. R. Bizzarri, S. Cannistraro and R. Zenobi: *Vibrational changes induced by electron transfer in surface bound azurin metalloprotein studied by tip-enhanced Raman spectroscopy and scanning tunneling microscopy*, ACS Nano **11**, 12824 (2017).

[Kud00] A. Kudelski and B. Pettinger: *SERS on carbon chain segments: Monitoring locally surface chemistry*, Chemical Physics Letters **321**, 356 (2000).

[Kum15] N. Kumar, B. Stephanidis, R. Zenobi, A. J. Wain and D. Roy: *Nanoscale mapping of catalytic activity using tip-enhanced Raman spectroscopy*, Nanoscale **7**, 7133 (2015).

[Kum18] N. Kumar, W. Su, M. Veselý, B. M. Weckhuysen, A. J. Pollard and A. J. Wain: *Nanoscale chemical imaging of solid–liquid interfaces using tip-enhanced Raman spectroscopy*, Nanoscale **10**, 1815 (2018).

[Kum19] N. Kumar, C. S. Wondergem, A. J. Wain and B. M. Weckhuysen: *In situ nanoscale investigation of catalytic reactions in the liquid phase using zirconia-protected tip-enhanced Raman spectroscopy probes*, Journal of Physical Chemistry Letters **10**, 1669 (2019).

[Kun86] K. Kunimatsu, A. Aramata, N. Nakajima and H. Kita: *Infrared spectra of carbon monoxide adsorbed on a smooth gold electrode*, Journal of Electroanalytical Chemistry and Interfacial Electrochemistry **207**, 293 (1986).

[Kur15] D. Kurouski, M. Mattei and R. P. Van Duyne: *Probing redox reactions at the nanoscale with electrochemical tip-enhanced Raman spectroscopy*, Nano Letters **15**, 7956 (2015).

[Kur16] D. Kurouski: *Advances of tip-enhanced Raman spectroscopy (TERS) in electrochemistry, biochemistry, and surface science*, Vibrational Spectroscopy **91**, 3 (2016).

[Lam96] D. K. Lambert: *Vibrational Stark effect of adsorbates at electrochemical interfaces*, Electrochimica Acta **41**, 623 (1996).

[Le 07] E. C. Le Ru, E. Blackie, M. Meyer and P. G. Etchegoint: *Surface enhanced Raman scattering enhancement factors: A comprehensive study*, Journal of Physical Chemistry C **111**, 13794 (2007).

[Le 09] E. Le Ru and P. Etchegoin: *Principles of surface-enhanced Raman spectroscopy: And related plasmonic effects*, Elsevier, 2009.

[Lee19] J. Lee, K. T. Crampton and N. Tallarida: *Visualizing vibrational normal modes of a single molcule with atomically confined light*, Nature **568**, 78 (2019).

[Len19] R. van Lent, S. V. Auras, K. Cao, A. J. Walsh, M. A. Gleeson and L. B. F. Juurlink: *Site-specific reactivity of molecules with surface defects - the case of H_2 dissociation on Pt*, Science **363**, 155 (2019).

[Leu87] L. W. H. Leung and M. J. Weaver: *Extending surface-enhanced Raman spectroscopy to transition-metal surfaces: Carbon monoxide adsorption and electrooxidation on platinum- and palladium-coated gold electrodes*, Journal of the American Chemical Society **109**, 5113 (1987).

[Leu88] L. W. H. Leung, A. Wieckowski and M. J. Weaver: *In situ infrared spectroscopy of well-defined single-crystal electrodes: Adsorption and electrooxidation of carbon monoxide on platinum(111)*, The Journal of Physical Chemistry **92**, 6985 (1988).

[Li03] X. Li and A. A. Gewirth: *Peroxide electroreduction on Bi-modified Au surfaces: Vibrational spectroscopy and density functional calculations*, Journal of the American Chemical Society **125**, 7086 (2003).

[Li10] J. F. Li and Z. Q. Tian: *Shell-isolated nanoparticle-enhanced Raman spectroscopy (SHINERS)*, Nature **464**, 163 (2010).

[Li15] C. Y. Li, J. C. Dong, X. Jin, S. Chen, R. Panneerselvam, A. V. Rudnev, Z. L. Yang, J. F. Li, T. Wandlowski and Z. Q. Tian: *In situ monitoring of electrooxidation processes at gold single crystal surfaces using shell-isolated nanoparticle-enhanced Raman spectroscopy*, Journal of the American Chemical Society **137**, 7648 (2015).

[Lia19] Y. Liang, D. McLaughlin, C. Csoklich, O. Schneider and A. S. Bandarenka: *The nature of active centers catalyzing oxygen electro-reduction at platinum surfaces in alkaline media*, Energy and Environmental Science **12**, 351 (2019).

[Liu86] H. Y. Liu, F. R. F. Fan, C. W. Lin and A. J. Bard: *Scanning electrochemical and tunneling ultramicroelectrode microscope for high-resolution examination of electrode surfaces in solution*, Journal of the American Chemical Society **108**, 3838 (1986).

[Liu11] Z. Liu, S.-Y. Ding, Z.-B. Chen, X. Wang, J.-H. Tian, J. R. Anema, X.-S. Zhou, D.-Y. Wu, B.-W. Mao, X. Xu, B. Ren and Z.-Q. Tian: *Revealing the molecular structure of single-molecule junctions in different conductance states by fishing-mode tip-enhanced Raman spectroscopy*, Nature communications **2**, 305 (2011).

[Luo18] L. Luo, M. Su, P. Yan, L. Zou, D. K. Schreiber, D. R. Baer, Z. Zhu, G. Zhou, Y. Wang, S. M. Bruemmer, Z. Xu and C. Wang: *Atomic origins of water-vapour-promoted alloy oxidation*, Nature Materials **17**, 514 (2018).

[Mag92] O. M. Magnussen, J. Hageböck, J. Hotlos and R. J. Behm: *In situ scanning tunnelling microscopy observations of a disorder–order phase transition in hydrogensulfate adlayers on Au(111)*, Faraday Discuss. **94**, 329 (1992).

[Mar01] F. Maroun, F. Ozanam, O. M. Magnussen and R. J. Behm: *The role of atomic ensembles in the reactivity of bimetallic electrocatalysts*, Science **293**, 1811 (2001).

[Mar16] N. Martín Sabanés, L. Driessen and K. F. Domke: *A versatile side-illumination geometry for tip-enhanced Raman spectroscopy at solid/liquid interfaces*, Analytical Chemistry **88**, 7108 (2016).

[Mar17a] N. Martín Sabanés, A. Elizabeth, J. H. Pfisterer and K. F. Domke: *The effect of STM parameters on tip-enhanced Raman spectra*, Faraday Discussions **205**, 233 (2017).

[Mar17b] N. Martín Sabanés, T. Ohto, D. Andrienko, Y. Nagata and K. F. Domke: *Electrochemical TERS elucidates potential-induced molecular reorientation of adenine/Au(111)*, Angewandte Chemie - International Edition **56**, 9796 (2017).

[Mar18] N. Martín Sabanés: *Electrochemical tip-enhanced Raman spectroscopy, development and applications*, Ph.D. thesis, Johannes Gutenberg Universität (2018).

[Mat16] M. Mattei, G. Kang, G. Goubert, D. V. Chulhai, G. C. Schatz, L. Jensen and R. P. Van Duyne: *Tip-enhanced Raman voltammetry: Coverage dependence and quantitative modeling*, Nano Letters **17**, 590 (2016).

[Mei18] F. Meirer and B. M. Weckhuysen: *Spatial and temporal exploration of heterogeneous catalysts with synchrotron radiation*, Nature Reviews Materials **3**, 324 (2018).

[Men15] L. Meng, Z. Yang, J. Chen and M. Sun: *Effect of electric field gradient on sub-nanometer spatial resolution of tip-enhanced Raman spectroscopy*, Scientific Reports **5**, 1 (2015).

[Mez16] S. Mezzavilla, S. Cherevko, C. Baldizzone, E. Pizzutilo, G. Polymeros and K. J. Mayrhofer: *Experimental methodologies to understand degradation of nanostructured electrocatalysts for PEM fuel cells: Advances and opportunities*, ChemElectroChem **3**, 1524 (2016).

[Mis16] H. Mistry, A. S. Varela, S. Kühl, P. Strasser and B. R. Cuenya: *Nanostructured electrocatalysts with tunable activity and selectivity*, Nature Reviews Materials **1**, 16009 (2016).

[Mub12] S. Mubeen, S. Zhang, N. Kim, S. Lee, S. Krämer, H. Xu and M. Moskovits: *Plasmonic properties of gold nanoparticles separated from a gold mirror by an ultrathin oxide*, Nano Letters **12**, 2088 (2012).

[Mül16] K. Müllen: *Molecular defects in organic materials*, Nature Reviews Materials **1**, 15013 (2016).

[Nak13] A. Nakata, T. Nomoto, T. Toyota and M. Fujinami: *Tip-enhanced Raman spectroscopy of lipid bilayers in water with an alumina- and silver-coated tungsten tip*, Analytical Sciences **29**, 865 (2013).

[Neu13] F. Neubrech and A. Pucci: *Plasmonic enhancement of vibrational excitations in the infrared*, IEEE Journal on Selected Topics in Quantum Electronics **19**, 4600809 (2013).

[Nod99] H. Noda, K. Ataka, L. J. Wan and M. Osawa: *Time-resolved surface-enhanced infra-red study of molecular adsorption at the electrochemical interface*, Surface Science **427**, 190 (1999).

[Oes83] U. Oesch and J. Janata: *Electrochemical study of gold electrodes with anodic oxide films-I. Formation and reduction behaviour of anodic oxides on gold*, Electrochimica Acta **28**, 1237 (1983).

[O'M14] A. P. O'Mullane: *From single crystal surfaces to single atoms: Investigating active sites in electrocatalysis*, Nanoscale **6**, 4012 (2014).

[Osa91] M. Osawa, K. Ataka, M. Ikeda, H. Uchihara and R. Nanba: *Surface-enhanced infrared absorption spectroscopy: Mechanism and application to trace analysis*, Analytical Sciences **7**, 503 (1991).

[Osa97] M. Osawa: *Dynamic processes in electrochemical reactions studied by surface-enhanced infrared absorption spectroscopy (SEIRAS)*, Bulletin of the Chemical Society of Japan **70**, 2861 (1997).

[Osa01] M. Osawa: *Near-field optics and surface plasmon polaritons*, Springer, 2001.

[Ott92] A. Otto, I. Mrozek, H. Grabhorn and W. Akemann: *Surface-enhanced Raman scattering*, Journal of Physics: Condensed Matter **4**, 1143 (1992).

[Our13] K. Oura, V. G. Lifshits, A. A. Saranin, A. V. Zotov and M. Katayama: *Surface science: An introduction*, Springer Science & Business Media, 2013.

[Pat97] E. M. Patrito, P. Paredes Olivera and H. Sellers: *On the nature of the SO_4^{2-}/Ag(111) and SO_4^{2-}/Au(111) surface bonding*, Surface Science **380**, 264 (1997).

[Per81] B. N. Persson and R. Ryberg: *Vibrational interaction between molecules adsorbed on a metal surface: The dipole-dipole interaction*, Physical Review B **24**, 6954 (1981).

[Pet00] B. Pettinger, G. Piccardi, R. Schuster and G. Etrl: *Surface enhanced Raman spectroscopy: Towards single molecule spectroscopy*, Electrochemistry **68**, 942 (2000).

[Pet05] B. Pettinger, B. Ren, G. Picardi, R. Schuster and G. Ertl: *Tip-enhanced Raman spectroscopy (TERS) of malachite green isothiocyanate at Au(111): Bleaching behavior under the influence of high electromagnetic fields*, Journal of Raman Spectroscopy **36**, 541 (2005).

[Pet07] B. Pettinger, K. F. Domke, D. Zhang, R. Schuster and G. Ertl: *Direct monitoring of plasmon resonances in a tip-surface gap of varying width*, Physical Review B - Condensed Matter and Materials Physics **76**, 1 (2007).

[Pet12] B. Pettinger, P. Schambach, C. J. Villagómez and N. Scott: *Tip-enhanced Raman spectroscopy: Near-fields acting on a few molecules*, Annual Review of Physical Chemistry **63**, 379 (2012).

[Peu84] M. Peuckert, F. P. Coenen and H. P. Bonzel: *On the surface oxidation of a gold electrode in 1N H_2SO_4 electrolyte*, Surface Science **141**, 515 (1984).

[Pfi17] J. H. K. Pfisterer, Y. Liang, O. Schneider and A. S. Bandarenka: *Direct instrumental identification of catalytically active surface sites*, Nature **549**, 74 (2017).

[Pfi18] J. H. K. Pfisterer and K. F. Domke: *Unfolding the versatile potential of EC-TERS for electrocatalysis*, Current Opinion in Electrochemistry **8**, 96 (2018).

[Pfi19a] J. H. K. Pfisterer, M. Baghernejad, G. Giuzio and K. F. Domke: *Reactivity mapping of nanoscale defect chemistry under electro-catalytic reaction conditions*, submitted (2019).

[Pfi19b] J. H. K. Pfisterer, F. Nattino, U. E. Zhumaev, M. Breiner, J. M. Feliu, N. Marzari and K. F. Domke: *Observation of OH intermediates during the gold oxide reduction reaction by EC-SERS and implicit solvent DFT*, in preparation (2019).

[Pfi19c] J. H. K. Pfisterer, U. E. Zhumaev, W. Cheuquepan, J. M. Feliu and K. F. Domke: *Stark effect or coverage dependence? Disentangling the EC-SEIRAS vibrational shift of sulfate on Au(111)*, The Journal of Chemical Physics **150**, 041709 (2019).

[Pie16] P. Pienpinijtham, S. Vantasin, Y. Kitahama, S. Ekgasit and Y. Ozaki: *Nanoscale pH profile at a solution/solid interface by chemically modified tip-enhanced Raman scattering*, Journal of Physical Chemistry C **120**, 14663 (2016).

[Pod79] J. J. Podesta, R. C. V. Piatti and A. J. Arvia: *Periodic current oscillations at the gold/acid aqueous interfaces induced by HCl additions*, Electrochimica Acta **24**, 633 (1979).

[Pom04] A. J. L. Pombeiro and C. Amatore: *Trends in molecular electrochemistry*, Taylor & Francis Group, 2004.

[Rah10] P. Rahe, R. Bechstein and A. Kühnle: *Vertical and lateral drift corrections of scanning probe microscopy images*, Journal of Vacuum Science & Technology B, Nanotechnology and Microelectronics: Materials, Processing, Measurement, and Phenomena **28**, C4E31 (2010).

[Ram28] C. V. Raman and K. S. Krishnan: *A new type of secondary Radiation*, Nature **121**, 501 (1928).

[Rei12] T. Reier, M. Oezaslan and P. Strasser: *Electrocatalytic oxygen evolution reaction (OER) on Ru, Ir, and Pt catalysts: A comparative study of nanoparticles and bulk materials*, ACS Catalysis **2**, 1765 (2012).

[Rei17] T. Reier, H. N. Nong, D. Teschner, R. Schlögl and P. Strasser: *Electrocatalytic oxygen evolution reaction in acidic environments - reaction mechanisms and catalysts*, Advanced Energy Materials **7**, 1601275 (2017).

[Ren04] B. Ren, G. Picardi and B. Pettinger: *Preparation of gold tips suitable for tip-enhanced Raman spectroscopy and light emission by electrochemical etching*, Review of Scientific Instruments **75**, 837 (2004).

[RL17] M. Richard-Lacroix, Y. Zhang, Z. Dong and V. Deckert: *Mastering high resolution tip-enhanced Raman spectroscopy: Towards a shift of perception*, Chemical Society Reviews **46**, 3922 (2017).

[Rod03a] A. Rodes, J. M. Orts, J. M. Pérez, J. M. Feliu and A. Aldaz: *Sulphate adsorption at chemically deposited silver thin film electrodes: Time-dependent behaviour as studied by internal reflection step-scan infrared spectroscopy*, Electrochemistry Communications **5**, 56 (2003).

[Rod03b] F. J. Rodríguez Nieto, G. Andreasen, M. E. Martins, F. Castez, R. C. Salvarezza and A. J. Arvia: *Scanning tunneling microscopy, voltammetry, and X-ray photoelectron spectroscopy study of the early stages of electrochemical faceting of gold (111) in aqueous sulfuric and perchloric acid*, The Journal of Physical Chemistry B **107**, 11452 (2003).

[Rod14] P. Rodriguez and M. T. Koper: *Electrocatalysis on gold*, Physical Chemistry Chemical Physics **16**, 13583 (2014).

[Sam05] G. Samjeské and M. Osawa: *Current oscillations during formic acid oxidation on a Pt electrode: Insight into the mechanism by time-resolved IR spectroscopy*, Angewandte Chemie - International Edition **44**, 5694 (2005).

[Sar10] D. Sarid and W. A. Challener: *Modern introduction to surface plasmons: Theory, Mathematica modeling, and applications*, Cambridge University Press, 2010.

[Sch97] M. A. Schneeweiss and D. M. Kolb: *Oxide formation on Au(111) An in situ STM study*, Solid State Ionics **94**, 171 (1997).

[Sch98] F. Schwabl: *Quantenmechanik*, Springer Berlin Heidelberg, 1998.

[Sch03] A. Schlapka, M. Lischka, A. Groß, U. Käsberger and P. Jakob: *Surface strain versus substrate interaction in heteroepitaxial metal layers: Pt on Ru(0001)*, Physical Review Letters **91**, 016101 (2003).

[Sch05] H. Schmidbaur, S. Cronje, B. Djordjevic and O. Schuster: *Understanding gold chemistry through relativity*, Chemical Physics **311**, 151 (2005).

[Sch09] T. Schmid, B. S. Yeo, G. Leong, J. Stadler and R. Zenobi: *Performing tip-enhanced Raman spectroscopy in liquids*, Journal of Raman Spectroscopy **40**, 1392 (2009).

[Sch13] T. Schmid, L. Opilik, C. Blum and R. Zenobi: *Nanoscale chemical imaging using tip-enhanced Raman spectroscopy: A critical review*, Angewandte Chemie - International Edition **52**, 5940 (2013).

[Sch14] S. Schlücker: *Surface-enhanced Raman spectroscopy: Concepts and chemical applications*, Angewandte Chemie - International Edition **53**, 4756 (2014).

[Set17] M. Setvín, M. Wagner, M. Schmid, G. S. Parkinson and U. Diebold: *Surface point defects on bulk oxides: Atomically-resolved scanning probe microscopy*, Chemical Society reviews **46**, 1772 (2017).

[SH10] Y. Shao-Horn, Y. C. Lu, Z. C. Xu, H. A. Gasteiger, S. Chen and K. Hamad-Schifferli: *Platinum-gold nanoparticles: A highly active bifunctional electrocatalyst for rechargeable lithium-air batteries*, Journal of the American Chemical Society **132**, 12170 (2010).

[Sha98] V. M. Shalaev and A. K. Sarychev: *Nonlinear optics of random metal-dielectric films*, Physical Review B **57**, 265 (1998).

[Sha15] G. Sharma, T. Deckert-Gaudig and V. Deckert: *Tip-enhanced Raman scattering - Targeting structure-specific surface characterization for biomedical samples*, Advanced Drug Delivery Reviews **89**, 42 (2015).

[She17] Z. W. She, J. Kibsgaard, C. F. Dickens, I. Chorkendorff, J. K. Nørskov and T. F. Jaramillo: *Combining theory and experiment in electrocatalysis: Insights into materials design*, Science **355**, 1 (2017).

[Shi94] Z. Shi, J. Lipkowski, M. Gamboa, P. Zelenay and A. Wieckowski: *Investigations of SO_4^{2-} adsorption at the Au (111) electrode by chronocoulometry and radiochemistry*, Journal of Electroanalytical Chemistry **366**, 317 (1994).

[Shi99] Y. Shingaya and M. Ito: *Comparison of a bisulfate anion adsorbed on M(111) (M = Pt, Rh, Au, Ag and Cu)*, Journal of Electroanalytical Chemistry **467**, 299 (1999).

[Shi07] H. Shi, R. Asahi and C. Stampfl: *Properties of the gold oxides Au_2O_3 and Au_2O: First-principles investigation*, Physical Review B **75**, 1 (2007).

[Shi17] X. Shi, N. Coca-López, J. Janik and A. Hartschuh: *Advances in tip-enhanced near-field Raman microscopy using nanoantennas*, Chemical Reviews **117**, 4945 (2017).

[Shr14] B. R. Shrestha, T. Baimpos, S. Raman and M. Valtiner: *Angstrom-resolved real-time dissection of electrochemically active noble metal interfaces*, ACS Nano **8**, 5979 (2014).

[Sie08] F. Siebert and P. Hildebrandt: *Vibrational spectroscopy in life science*, John Wiley & Sons, 2008.

[Smi97] B. D. Smith and D. E. Irish: *A surface enhanced Raman scattering study of the intermediate and poisoning species formed during the electrochemical reduction of CO_2 on copper*, Journal of the Electrochemical Society **144**, 4288 (1997).

[Son86] R. Sonnenfeld and P. K. Hansma: *Atomic-resolution microscopy in water*, Science **232**, 211 (1986).

[Sri98] S. Sriramulu, T. Jarvi and E. Stuve: *A kinetic analysis of distinct reaction pathways in methanol electrocatalysis on Pt(111)*, Electrochimica Acta **44**, 1127 (1998).

[Sta12] J. Stadler, T. Schmid and R. Zenobi: *Developments in and practical guidelines for tip-enhanced Raman spectroscopy*, Nanoscale **4**, 1856 (2012).

[Ste08] J. Steidtner and B. Pettinger: *Tip-enhanced Raman spectroscopy and microscopy on single dye molecules with 15 nm resolution*, Physical Review Letters **100**, 1 (2008).

[Ste11] I. E. Stephens, A. S. Bondarenko, F. J. Perez-Alonso, F. Calle-Vallejo, L. Bech, T. P. Johansson, A. K. Jepsen, R. Frydendal, B. P. Knudsen, J. Rossmeisl and I. Chorkendorff: *Tuning the activity of Pt(111) for oxygen electroreduction by subsurface alloying*, Journal of the American Chemical Society **133**, 5485 (2011).

[Stö00] R. M. Stöckle, Y. D. Suh, V. Deckert and R. Zenobi: *Nanoscale chemical analysis by tip-enhanced Raman spectroscopy*, Chemical Physics Letters **318**, 131 (2000).

[Štr88] S. Štrbac, R. R. Adžić and A. Hamelin: *Oxide formation on gold single crystal stepped surfaces*, Journal of Electroanalytical Chemistry **249**, 291 (1988).

[Su18] H. S. Su, X. G. Zhang, J. J. Sun, X. Jin, D. Y. Wu, X. B. Lian, J. H. Zhong and B. Ren: *Real-space observation of atomic site-specific electronic properties of a Pt nanoisland/Au(111) bimetallic surface by tip-enhanced Raman spectroscopy*, Angewandte Chemie - International Edition **57**, 13177 (2018).

[Sun12] M. Sun, Z. Zhang, H. Zheng and H. Xu: *In-situ plasmon-driven chemical reactions revealed by high vacuum tip-enhanced Raman spectroscopy*, Scientific reports **2**, 647 (2012).

[Sun14] T. Sun, Y. Yu, B. J. Zacher and M. V. Mirkin: *Scanning electrochemical microscopy of individual catalytic nanoparticles*, Angewandte Chemie - International Edition **53**, 14120 (2014).

[Sun19] T. Sun, H. Zhang, X. Wang, J. Liu, C. Xiao, S. U. Nanayakkara, J. L. Blackburn, M. V. Mirkin and E. M. Miller: *Nanoscale mapping of hydrogen evolution on metallic and semiconducting MoS_2 nanosheets*, Nanoscale Horizons **4**, 619 (2019).

[Tay25] H. S. Taylor: *A theory of the catalytic surface*, Proceedings of the Royal Society of London A: Mathematical, Physical and Engineering Sciences **108**, 105 (1925).

[Ter83] J. Tersoff and D. R. Hamann: *Theory and application for the scanning tunneling microscope*, Physical Review Letter **50**, 1998 (1983).

[TF97] G. Tremiliosi-Filho, L. H. Dall'Antonia and G. Jerkiewicz: *Limit to extent of formation of the quasi-two-dimensional oxide state on Au electrodes*, Journal of Electroanalytical Chemistry **422**, 149 (1997).

[TF05] G. Tremiliosi-Filho, L. H. Dall'Antonia and G. Jerkiewicz: *Growth of surface oxides on gold electrodes under well-defined potential, time and temperature conditions*, Journal of Electroanalytical Chemistry **578**, 1 (2005).

[Tho14] J. M. Thomas and W. J. Thomas: *Principles and practice of heterogeneous catalysis*, John Wiley & Sons, 2014.

[Tia02] Z. Q. Tian, B. Ren and D. Y. Wu: *Surface-enhanced Raman scattering: From noble to transition metals and from rough surfaces to ordered nanostructures*, Journal of Physical Chemistry B **106**, 9463 (2002).

[Toc16] C. Toccafondi, G. Picardi and R. Ossikovski: *Molecular bending at the nanoscale evidenced by tip-enhanced Raman spectroscopy in tunneling mode on thiol self-assembled monolayers*, Journal of Physical Chemistry C **120**, 18209 (2016).

[Tou16] T. Touzalin, A. L. Dauphin, S. Joiret, I. T. Lucas and E. Maisonhaute: *Tip-enhanced Raman spectroscopy imaging of opaque samples in organic liquid*, Physical Chemistry Chemical Physics **18**, 2 (2016).

[Tou17] T. Touzalin, S. Joiret, E. Maisonhaute and I. T. Lucas: *Complex electron transfer pathway at a microelectrode captured by in situ nanospectroscopy*, Analytical Chemistry **89**, 8974 (2017).

[Tra86] S. Trasatti: *The absolute electrode potential: An explanatory note*, Pure and Applied Chemistry **58**, 955 (1986).

[Tro89] A. P. van Troostwijk and J. R. Deiman: *Sur une maniere de decomposer l'eau en air inflammable et en air vital*, Obs Phys **35**, 369 (1789).

[Tym16] J. Tymoczko, F. Calle-Vallejo, W. Schuhmann and A. S. Bandarenka: *Making the hydrogen evolution reaction in polymer electrolyte membrane electrolysers even faster*, Nature Communications **7**, 10990 (2016).

[Ulv15] A. Ulvestad, A. Singer, J. N. Clark, H. M. Cho, J. W. Kim, R. Harder, J. Maser, Y. S. Meng and O. G. Shpyrko: *Topological defect dynamics in operando battery nanoparticles*, Science **348**, 1344 (2015).

[Van69] R. Van Hardeveld and F. Hartog: *The statistics of surface atoms and surface sites on metal crystals*, Surface Science **15**, 189 (1969).

[van12] E. M. van Schrojenstein Lantman, T. Deckert-Gaudig, A. J. Mank, V. Deckert and B. M. Weckhuysen: *Catalytic processes monitored at the nanoscale with tip-enhanced Raman spectroscopy*, Nature Nanotechnology **7**, 583 (2012).

[Van13] P. Vandenabeele: *Practical Raman spectroscopy - An introduction*, vol. 1, Wiley, 2013.

[Van17] M. A. Van Spronsen, J. W. Frenken and I. M. Groot: *Observing the oxidation of platinum*, Nature Communications **8**, 1 (2017).

[Vel90] M. E. Vela, R. C. Salvarezza and A. J. Arvia: *The electroreduction kinetics of the hydrous gold oxide layers and growth modes and roughness of the electroreduced gold overlayers*, Electrochimica Acta **35**, 117 (1990).

[Voi15] B. Voigtländer: *Scanning probe microscopes*, Springer, 2015.

[Wan01] X. Wang and L. Andrews: *Precious metal-molecular oxygen complexes: Neon matrix infrared spectra and density functional calculations for $M(O_2)$, $M(O_2)_2$ (M = Pd, Pt, Ag, Au)*, Journal of Physical Chemistry A **105**, 5812 (2001).

[Wan04] T. Wandlowski, K. Ataka, S. Pronkin and D. Diesing: *Surface enhanced infrared spectroscopy - Au(111-20 nm)/sulphuric acid - New aspects and challenges*, Electrochimica Acta **49**, 1233 (2004).

[Wan17] X. Wang, S. C. Huang, T. X. Huang, H. S. Su, J. H. Zhong, Z. C. Zeng, M. H. Li and B. Ren: *Tip-enhanced Raman spectroscopy for surfaces and interfaces*, Chemical Society Reviews **46**, 4020 (2017).

[Wen16] B. Y. Wen, X. Jin, Y. Li, Y. H. Wang, C. Y. Li, M. M. Liang, R. Panneerselvam, Q. C. Xu, D. Y. Wu, Z. L. Yang, J. F. Li and Z. Q. Tian: *Shell-isolated nanoparticle-enhanced Raman spectroscopy study of the adsorption behaviour of DNA bases on Au(111) electrode surfaces*, Analyst **141**, 3731 (2016).

[Wes85] J. Wessel: *Surface-enhanced optical microscopy*, Journal of the Optical Society of America B **2**, 1538 (1985).

[Wil19] K. A. Willets: *Probing nanoscale interfaces with electrochemical surface-enhanced Raman scattering*, Current Opinion in Electrochemistry **13**, 18 (2019).

[Wok84] A. Wokaun: *Surface-enhanced electromagnetic processes*, in *Solid state physics*, vol. 38, Elsevier, 1984, 223–294.

[Wu08] D.-Y. Wu, J.-F. Li, B. Ren and Z.-Q. Tian: *Electrochemical surface-enhanced Raman spectroscopy of nanostructures.*, Chemical Society reviews **37**, 1025 (2008).

[Yao08] J. L. Yao, Y. X. Yuan, X. M. Fan, B. Ren, R. A. Gu and Z. Q. Tian: *The reorientation of benzonitrile on platinum electrode probed by surface enhanced Raman spectroscopy*, Journal of Electroanalytical Chemistry **624**, 129 (2008).

[Yeo10] B. S. Yeo, S. L. Klaus, P. N. Ross, R. A. Mathies and A. T. Bell: *Identification of hydroperoxy species as reaction intermediates in the electrochemical evolution of oxygen on gold*, ChemPhysChem **11**, 1854 (2010).

[Yeo11] B. S. Yeo and A. T. Bell: *Enhanced activity of gold-supported cobalt oxide for the electrochemical evolution of oxygen*, Journal of the American Chemical Society **133**, 5587 (2011).

[Yok19] Y. Yokota, N. Hayazawa, B. Yang, E. Kazuma, F. C. I. Catalan and Y. Kim: *Systematic assessment of benzenethiol self-assembled monolayers on Au(111) as a standard sample for electrochemical tip-enhanced Raman spectroscopy*, The Journal of Physical Chemistry C **123**, 2953 (2019).

[You18] B. You and Y. Sun: *Innovative strategies for electrocatalytic water splitting*, Accounts of Chemical Research **51**, 1571 (2018).

[Zae14] F. Zaera: *New advances in the use of infrared absorption spectroscopy for the characterization of heterogeneous catalytic reactions*, Chemical Society Reviews **43**, 7624 (2014).

[Zam96] T. Zambelli, J. Wintterlin, J. Trost and G. Ertl: *Identification of the "active sites" of a surface-catalyzed reaction*, Science **273**, 1688 (1996).

[Zap16] M. Zapata Herrera, J. Aizpurua, A. K. Kazansky and A. G. Borisov: *Plasmon response and electron dynamics in charged metallic nanoparticles*, Langmuir **32**, 2829 (2016).

[Zen15] Z.-C. Zeng, S.-C. Huang, D.-Y. Wu, L.-Y. Meng, M.-H. Li, T.-X. Huang, Z. Jin-Hui, X. Wang, Z.-L. Yang and B. Ren: *Electrochemical tip-enhanced Raman spectroscopy*, Journal of the American Chemical Society **137**, 11928 (2015).

[Zha93] Y. Zhang, X. Gao and M. J. Weaver: *Nature of surface bonding on voltammetrically oxidized noble metals in aqueous media as probed by real-time surface-enhanced Raman spectroscopy*, The Journal of Physical Chemistry **97**, 8656 (1993).

[Zha10] D. Zhang, K. F. Domke and B. Pettinger: *Tip-enhanced Raman spectroscopic studies of the hydrogen bonding between adenine and thymine adsorbed on Au (111)*, ChemPhysChem **11**, 1662 (2010).

[Zha13a] R. Zhang, Y. Zhang, Z. C. Dong, S. Jiang, C. Zhang, L. G. Chen, L. Zhang, Y. Liao, J. Aizpurua, Y. Luo, J. L. Yang and J. G. Hou: *Chemical mapping of a single molecule by plasmon-enhanced Raman scattering.*, Nature **498**, 82 (2013).

[Zha13b] Z. Zhang, L. Chen, M. Sun, P. Ruan, H. Zheng and H. Xu: *Insights into the nature of plasmon-driven catalytic reactions revealed by HV-TERS*, Nanoscale **5**, 3249 (2013).

[Zho17] J.-H. Zhong, X. Jin, L. Meng, X. Wang, H.-S. Su, Z.-L. Yang, C. T. Williams and B. Ren: *Probing the electronic and catalytic properties of a bimetallic surface with 3 nm resolution*, Nature Nanotechnology **12**, 132 (2017).

[Zhu13] U. Zhumaev, A. V. Rudnev, J. F. Li, A. Kuzume, T. H. Vu and T. Wandlowski: *Electro-oxidation of Au(1 1 1) in contact with aqueous electrolytes: New insight from in situ vibration spectroscopy*, Electrochimica Acta **112**, 853 (2013).

[Zhu18] U. Zhumaev and K. Domke: *Surface-enhanced infrared absorption spectroscopy*, 1, Elsevier, 2018.

Publications

Publications covered in this thesis

Jonas H. K. Pfisterer, Masoud Baghernejad, Giovanni Giuzio, Katrin F. Domke, "Reactivity mapping of nanoscale defect-chemistry under electro-catalytic reaction conditions", submitted.

Jonas H. K. Pfisterer, Francesco Nattino, Ulmas E. Zhumaev, Manuel Breiner, Juan M. Feliu, Nicola Marzari, Katrin F. Domke, "Observation of reaction intermediates during the gold oxide reduction reaction by EC-SERS and implicit solvent DFT", to be submitted.

Jonas H. K. Pfisterer, Ulmas E. Zhumaev, William Cheuquepan, Juan M. Feliu, Katrin F. Domke, "Stark effect or coverage dependence? Disentangling the EC-SEIRAS vibrational shift of sulfate on Au(111)", Journal of Chemical Physics, 2019, 150(4), 041709.

Jonas H. K. Pfisterer and Katrin F. Domke, "Unfolding the versatile potential of EC-TERS for electrocatalysis", Current Opinion in Electrochemistry, 2018, 8, 96-102.

Other publications

Macholdt, D. S., Herrmann, S., Jochum, K. P., Kilcoyne, A. D., Laubscher, T., Pfisterer, J. H. K., Pöhlker, C., Schwager, B., Weber, B., Weigand, M., Domke, K. F., Andreae, M. O., "Black manganese-rich crusts on a Gothic cathedral", Atmospheric Environment, 2017, 171, 205-220.

Natalia Martin-Sabanés, Amala Elizabeth, Jonas H. K. Pfisterer and Katrin F. Domke, "The effect of STM parameters on tip-enhanced Raman spectra", Faraday Discussions, 2017, 205, 233-243.